

Electronic Thesis and Dissertation Repository

12-12-2019 3:00 PM

Design and Analysis of a Compliant 3D Printed Energy Harvester Package for Knee Implants

Geoffrey Yamomo
The University of Western Ontario

Supervisor
Willing, Ryan T.
The University of Western Ontario

Graduate Program in Mechanical and Materials Engineering
A thesis submitted in partial fulfillment of the requirements for the degree in Master of Engineering Science
© Geoffrey Yamomo 2019

Follow this and additional works at: <https://ir.lib.uwo.ca/etd>

Recommended Citation

Yamomo, Geoffrey, "Design and Analysis of a Compliant 3D Printed Energy Harvester Package for Knee Implants" (2019). *Electronic Thesis and Dissertation Repository*. 6728.
<https://ir.lib.uwo.ca/etd/6728>

This Dissertation/Thesis is brought to you for free and open access by Scholarship@Western. It has been accepted for inclusion in Electronic Thesis and Dissertation Repository by an authorized administrator of Scholarship@Western. For more information, please contact wlsadmin@uwo.ca.

Abstract

Instrumented implants provide the potential to measure the *in vivo* tibiofemoral forces that are transmitted through total knee replacements (TKR). The continuous feedback from instrumented implants can be used to objectively justify actions to reduce the risk of implant failure. The main obstacle in developing “smart implants” is reliably powering such devices. Energy harvesting mechanisms, such as the triboelectric effect, can be leveraged to produce usable electricity and measure the transmitted loads in TKRs. A compliant package that interlocks with commercially available TKR components was designed to house triboelectric generators (TEG). Prototypes were more compliant than what was expected from the computational models. During fatigue testing, the prototype failed prematurely due to inherent issues with additive manufacturing. However, these issues can be mitigated with improved post-processing techniques. This package serves as a novel approach to integrating self-powering load sensors in currently available knee implants.

Keywords

energy harvesting, knee implant, additive manufacturing, load sensor, triboelectric

Summary for Lay Audience

Osteoarthritis (OA), or the cartilage degradation in joints, can lead to pain and joint dysfunction. In severe cases of OA, the diseased joint may need to be reconstructed. Knee implants, consisting of metal components resurfacing the shin bone and thigh bone with a plastic insert in-between, replace the diseased bone, relieve pain and restore function. Over time, knee implants can fail for several reasons, such as implant loosening from the surrounding bone and abnormal motion between the thigh bone and the shinbone. Devices that measure forces transmitted through knee implants can improve our understanding of what a knee implant undergoes daily, thus providing information on how to prevent implant failure.

Currently, devices that monitor a patient's knee loads are unavailable. The main reason for this is because of the difficulty of powering these devices. Sensors that can generate power from human motion can be used to measure the loads acting on knee implants. Load sensors have been developed to generate power from static electricity. These sensors require a compliant package to cushion the forces acting on them when placed within a knee implant.

This thesis outlines the design of such a package. The package was designed using computer simulations and then its performance was measured through lab experiments. Prototypes of the package design were made with 3D printed titanium. In one lab experiment where the applied load was intentionally shifted from one side of the package to the other, the prototype predictably deformed more in the location where forces were concentrated. However, the 3D printed package was softer than what was predicted in the computer simulations. During durability testing, the package prototype underwent loading that simulates walking. Implant components should last for millions of cycles, but the current prototype failed prematurely. 3D printed titanium parts may have internal holes and defects that reduce the longevity of the parts. The fatigue strength of the package could be improved with heat treatment and removal of surface defects. The use of this package with embedded load sensors is a novel perspective on measuring the forces that act on knee implants.

Co-Authorship Statement

- Chapter 1: Geoffrey Yamomo – wrote manuscript
Ryan Willing – reviewed manuscript
- Chapter 2: Geoffrey Yamomo – study design, data collection, interpreted results, wrote manuscript
Ryan Willing – study design, interpreted results, reviewed manuscript
- Chapter 3: Geoffrey Yamomo – study design, data collection, interpreted results, wrote manuscript
Ryan Willing – study design, interpreted results, reviewed manuscript
- Chapter 4: Geoffrey Yamomo – study design, data collection, interpreted results, wrote manuscript
Ryan Willing – study design, interpreted results, reviewed manuscript
- Chapter 5: Geoffrey Yamomo – study design, data collection, interpreted results, wrote manuscript
Ryan Willing – study design, interpreted results, reviewed manuscript
- Chapter 6: Geoffrey Yamomo – wrote manuscript
Ryan Willing – reviewed manuscript

Acknowledgments

First and foremost, I would like to thank Dr. Ryan Willing for his guidance and support. Thank you for providing me the opportunity to grow as a budding engineer. I have learned a tremendous amount under your mentorship. Dr. Willing was always available when I had questions or when I needed assistance. I am sincerely grateful for your kind encouragement especially when I lost my way.

I had the opportunity to collaborate with great individuals in New York State. I would like to thank my colleagues in Binghamton University and Stony Brook University. It was an honour being part of this international, interdisciplinary research team.

It was a pleasure working with the folks in the Biomechanical Engineering Research Lab. Working with the surgeons made learning aspects of orthopaedics more engaging than in the classroom or reading textbooks. To my lab mates, Alireza, Sami and Emma, I enjoyed working alongside you and getting the job done.

To my fellow office mates during my graduate studies, thank you for providing an open and supportive environment. Whenever I needed assistance with something, I knew I always had someone to turn to. Also, thank you for tolerating the squalid state my work station always happened to be in. Your patience, kindness and understanding will surely be missed.

Lastly, I would like to thank my family. Mum and Dad, your love and support have not waned since I can first remember. To my sister and brother, Rose and Chris, despite being separated geographically for most of the year... you still manage to annoy me on occasion. However, you have always been there to talk to and thank you for always egging me on.

Funding Support:

This research has been supported by the National Institute of Arthritis and Musculoskeletal and Skin Diseases of the National Institute of Health (United States) under award number R21AR068572. The content is solely the responsibility of the authors and does not necessarily represent the official views of the National Institute of Health.

Table of Contents

Abstract.....	i
Summary for Lay Audience.....	ii
Co-Authorship Statement.....	iii
Acknowledgments.....	iv
Table of Contents.....	v
List of Tables.....	x
List of Figures.....	xi
List of Appendices.....	xvi
List of Abbreviations, Symbols and Nomenclature.....	xvii
Chapter 1.....	1
1 Introduction.....	1
1.1 Anatomical Movement Descriptors.....	1
1.1.1 Anatomical Terms Used to Describe Relative Position or Direction.....	1
1.1.2 Basic Movements.....	2
1.1.3 Cardinal Planes of the Body.....	3
1.2 Knee Anatomy.....	3
1.2.1 Osseous Anatomy of the Knee.....	4
1.2.2 Soft Tissue Anatomy of the Knee.....	5
1.2.2.1 Knee Ligaments.....	5
1.2.2.2 Muscles.....	7
1.3 Knee Osteoarthritis.....	8
1.3.1 Prevalence of Knee Osteoarthritis.....	9
1.4 Total Knee Replacements.....	10
1.4.1 Prevalence of Total Knee Replacements.....	11

1.4.2	Complications in Total Knee Arthroplasty	12
1.4.2.1	Instability	13
1.4.2.2	Aseptic Loosening	14
1.4.3	Revision Total Knee Arthroplasty.....	15
1.5	Instrumented Implants	17
1.5.1	Intraoperative Load Sensors	17
1.5.2	Postoperative Load Sensors	19
1.5.3	Triboelectric Effect	23
1.6	Thesis Rationale.....	26
1.7	Research Objectives.....	26
1.8	References.....	28
Chapter 2	38
2	Tuning of a 3D Printed Energy Harvester Package Design.....	38
2.1	Introduction.....	38
2.2	Materials and Methods.....	40
2.2.1	Dimensions of Elastic Bodies	40
2.2.2	Analytical Model Design	41
2.2.3	Computational Model Design.....	43
2.2.4	Placement of Elastic Bodies in Package Prototype.....	46
2.2.5	Spring Thickness Adjustment.....	47
2.2.6	Reverse Engineering Interlocking Mechanism of TKR Components	49
2.3	Results.....	50
2.3.1	Analytical Model Design	50
2.3.2	Computational Model Design.....	52
2.3.2.1	Simplified Design Simulations.....	52
2.3.2.2	Tuning of Midsection Thickness	55

2.3.3	Simulation Results of Prototype Design	56
2.3.4	Dimensions of Elastic Bodies	58
2.4	Discussion	60
2.5	Conclusion	64
2.6	References.....	65
Chapter 3	69
3	Experimental Validation and Load Imbalance Measurements of a Compliant Package Design	69
3.1	Introduction.....	69
3.2	Materials and Methods.....	70
3.2.1	Manufactured Prototype.....	70
3.2.2	Axial Loading of Package Prototype	72
3.2.3	Imbalance Testing.....	73
3.2.3.1	Flexiforce Sensor Calibration.....	76
3.2.3.2	Experimental Set-Up	77
3.3	Results.....	79
3.3.1	11Axial Loading of Package Prototype	79
3.3.2	Imbalance Testing.....	80
3.4	Discussion.....	81
3.4.1	Stiffness of Additively Manufactured Parts.....	81
3.4.2	Intercompartmental Load Measurements	82
3.5	Conclusion	83
3.6	References.....	85
Chapter 4	87
4	Durability Testing of Energy Harvester Package.....	87
4.1	Introduction.....	87

4.2	Materials and Methods.....	88
4.2.1	Experimental Set-Up.....	88
4.2.2	Loading Scenario at Maximum Vertical Load.....	90
4.2.3	Reduced Vertical Load	91
4.3	Results.....	92
4.3.1	Maximum Vertical Load.....	92
4.3.2	Reduced Vertical Load	94
4.4	Discussion.....	95
4.5	Conclusion	100
4.6	References.....	102
	Chapter 5.....	105
5	Sensitivity Analysis of Polyethylene Thickness and the Effect of Physiological Loading Assumptions	105
5.1	Introduction.....	105
5.2	Materials and Methods.....	106
5.3	Results.....	107
5.3.1	Axial Force Only versus Six Component Loading.....	107
5.3.2	Effect of Polyethylene Insert Thickness	110
5.4	Discussion.....	111
5.5	Conclusion	113
5.6	References.....	114
	Chapter 6.....	115
6	General Discussion and Conclusion	115
6.1	Summary.....	115
6.2	Strengths and Limitations	116
6.3	Future Directions	117

6.4 Significance.....	118
Appendices.....	119
Curriculum Vitae	153

List of Tables

Table 2-1-Stress and deflection comparison between computational and analytical model. The computational models presented in this table had dimensions similar to what was used in the analytical model.	53
Table 2-2- Stress and deflections resulting from dimensions altered using the One-Factor-at- a-Time method.	55
Table 2-3- Summary of stresses and resultant vertical force after altering beam midsection thickness using Bezier curves.	56
Table 2-4- Maximum Stress and Displacements from Maximum Loads in ISO 14243	58
Table 3-1- Selective Laser Melting Parameters	71

List of Figures

Figure 1-1- Primary movements of the knee (tibia with respect to the femur).....	2
Figure 1-2-Cardinal Planes of the Human Body.....	3
Figure 1-3- Osseous Anatomy of the Knee.....	5
Figure 1-4- Cruciate and Collateral Ligaments	7
Figure 1-5- (a) Quadriceps: vastus lateralis, rectus femoris, vastus medialis and vastus intermedius (<i>under rectus femoris</i>) (Anterior View of the Knee), and (b) Hamstrings: biceps femoris, semimembranosus and semitendinosus (Posterior View of the Knee).....	8
Figure 1-6- (A) The joint space narrowing and osteophyte formation in the anterior-posterior radiograph are indicative of bilateral medial osteoarthritis where joint space narrowing is greater in the right knee. (B) A magnified view of the right knee. (Braun and Gold, 2012) (Image use permitted by Elsevier)	9
Figure 1-7- Total Knee Replacement Components	11
Figure 1-8-Radiolucent Lines Surrounding the Tibial Stem (Kutzner et al., 2018) (Image use permitted by Taylor and Francis).....	15
Figure 1-9- Verasense Display (Manning et al., 2018) (Image use permitted by Creative Commons (https://creativecommons.org/licenses/by/4.0/))	18
Figure 1-10- Instrumented implant developed by D’Lima et al. with four transducers located at the four corners of the tibial tray (D’lima et al., 2005b) (Image use permitted by Elsevier)	20
Figure 1-11- (a) Tibial tray with telemetry system, (b) magnified view of the microprocessor and the internal power induction coil, (c) patient with external coil for powering the onboard electronics and telemetry system. (Kirking et al., 2006) (Image use permitted by Elsevier). 21	
Figure 1-12- Triboelectric Working Mechanism (Ibrahim et al., 2019a) (Image use permitted by IOP Publishing).....	24

Figure 1-13- Saw-tooth ridges of metal and dielectric layers (Ibrahim et al., 2019a) (Image use permitted by IOP Publishing) 25

Figure 2-1-Design Process Flowchart..... 40

Figure 2-2- CAD model of the preliminary prototype concept design that feature elastic bodies along the periphery: (a) superior view, (b) isometric view, (c) posterior view, (d) section view that shows the internal void for TEG..... 41

Figure 2-3- A magnified view of the beam structures located on the posterior of the package design. Length, height and fillet radius of the beams are denoted by L , h and r , respectively. *Note: The base (b) is orthogonal to h and L .* 42

Figure 2-4- Simplified, rectangular model used for further computational model iterations on the beam design. (a) isometric view, (b) front view 44

Figure 2-5- Boundary and Loading Conditions: (a) Fixed restraint on corner on bottom surface, (b) Roller/slider on bottom surface, (c) Force applied on top surface 45

Figure 2-6- Bezier Curve Dimensions 46

Figure 2-7- CAD Progression of Package Prototype: (a) STL file of tibial tray, (b) base of prototype, (c) extrusion of elastic bodies along periphery, (d) prototype with top plate..... 47

Figure 2-8-A posterior view of the package-PE bearing assembly. Reference point, RP-1, was placed inferior to the assembly. Reference point, RP-2, was placed superior to the assembly and offset medially to replicate a 60:40 (medial:lateral) load bias. 48

Figure 2-9- Effects of length and base parameters on the bending stress..... 51

Figure 2-10- Effect of length and base on the height..... 52

Figure 2-11- An isometric view of the FE model for Test Run 2 (Table 2-1). Peak stress locations were located at the base of the beams (denoted by red arrow)..... 53

Figure 2-12- Stress Plot from Maximum Axial Load..... 57

Figure 2-13- Vertical Displacement Plot from Maximum Axial Load.....	57
Figure 2-14- Shear displacements due to maximum posteriorly directed force (F_y) and internal moment (M_z) in ISO 14243	58
Figure 2-15- Dimensions of stacked beam structure	59
Figure 2-16- Cross-sectional view of the elastic bodies. The prototype was symmetrical along the sagittal plane, therefore dimensions were denoted only on one side.....	59
Figure 3-1- Package Prototype: (a) top view, (b) isometric view, (c) front view, (d) bottom view, (e) back view and (f) disassembled prototype.....	72
Figure 3-2- The VIVO joint simulator operates in six degrees of freedom. There are three translational (medial/lateral, anterior/posterior, superior/inferior) and three rotational degrees of freedom (internal/external, abduction/adduction, flexion/extension).....	74
Figure 3-3- Experimental set-up (the implant flexed about 60° for clarity)	75
Figure 3-4- Package Prototype with Embedded Flexiforce Sensors in the Medial and Lateral Compartments	77
Figure 3-5- Experimental set-up configurations: a) TKR mounted on VIVO joint simulator and b) TKR mounted on VIVO joint simulator with package prototype embedded with Flexiforce sensors.	78
Figure 3-6- Force vs. displacement plot of package prototype subjected to uniaxial vertical loading.....	80
Figure 3-7- Flexiforce measurements during cyclic abduction/adduction.	81
Figure 4-1- Experimental Set-up for Fatigue Testing on AMTI Boston: (a) Medial View, (b) Anteromedial View	89
Figure 4-2- von Mises Stress Plots of Maximum Load in Gait Cycle: a) Vertical Load of 2600 N, and b) Vertical Load of 2600 N Superimposed with Corresponding Shear Forces in Percent Gait Cycle (Anteriorly Directed Load of 109 N and Internal Torque of 0.9 Nm).....	91

Figure 4-3- Stress plot of the package at a reduced compressive load of 1400 N. The peak stress was below 550 MPa. The red arrow denotes the location of the peak stress..... 92

Figure 4-4- Locations of cracks on the lateral side of the prototype after fatigue testing was terminated. Cracks were located in the same locations on the medial side. 93

Figure 4-5- Vertical position of lower actuator at the maximum applied load of 2600 N in 10 000 cycle intervals. 94

Figure 4-6- Vertical position of lower actuator at the maximum applied load of 1400 N in 2000 cycle intervals. A decrease in the actuator position becomes consistent after 70 000 cycles..... 95

Figure 4-7- Comparison between the Results from Fatigue Testing and the FE Model 96

Figure 4-8- Posterior view of the computational model and a prototype that illustrate the distortion that was present in some of the elastic bodies: a) the area of interest is highlighted in the red circle, b) magnified view of computational model, and c) magnified view of prototype. 99

Figure 4-9- Example of a shift in the printing layers: a) posteromedial view of computational model, b) magnified view of computational model, and c) magnified view of prototype. .. 100

Figure 5-1- Comparison between uniaxial compressive loading and six component loading. Peak stresses occurred at 48% gait cycle for both loading scenarios. There was a 15% difference between load scenarios where the six component loading scenario was greatest. 107

Figure 5-2-Stress Plot of Maximum Six Component Loading: a) anterior, b) isometric, c) medial, d) lateral 108

Figure 5-3- Vertical Displacement Plot of Maximum Six Component Loading: a) superior, b) isometric, c) anterior, d) medial, e) lateral..... 108

Figure 5-4- Stress Plot of Maximum Vertical Load: a) anterior, b) lateral, c) posterior, d) isometric..... 109

Figure 5-5- Vertical Displacement Plot of Maximum Vertical Fz: a) superior, b) isometric, c) anterior, d) lateral..... 109

Figure 5-6- Comparison of the maximum von Mises stresses calculated in six component loading between a 9 mm and 11 mm PE bearing..... 111

List of Appendices

Appendix A- Analytical Model Calculations	119
Appendix B- Simplified Design Iterations using OFAT	123
Appendix C: Axial Loading of Rectangular Models	127
Appendix D: Stiffness Calculation of Single Silicone Spacer	132
Appendix E: AP Translation and IE Rotation Testing.....	132
Appendix F: Copyright Approval	135
Appendix G- Mechanical Testing Machine Technical Data Sheets	141

List of Abbreviations, Symbols and Nomenclature

A	area
AA	abduction/adduction
ACL	anterior cruciate ligament
ADL	activities of daily living
AM	additive manufacturing
AP	anterior/posterior
b	base
BMI	body mass index
CAD	computer aided design
COP	centre of pressure
CP-Ti	commercially pure titanium
CR	cruciate retaining
CS	condylar stabilized
d	displacement
DAQ	data acquisition
DOE	design of experiments
DOF	degree of freedom(s)
E	Young's modulus
FEA	finite element analysis
h	height
HIP	hot isostatic pressing
I	moment of inertia
IE	internal/external
JSN	joint space narrowing
k	stiffness
KSS	American Knee Society Scoring System
L	length
LCL	lateral collateral ligament
M	bending moment
MCL	medial collateral ligament
MEMS	micro-electromechanical system

ML	medial/lateral
NEMS	nano-electromechanical system
OA	osteoarthritis
OFAT	one-factor-at-a-time
PCL	posterior cruciate ligament
PDMS	polydimethylsiloxane
PE	polyethylene
PMMA	polymethylmethacrylate
PROMs	patient reported outcome measures
PS	posterior stabilized
PZT	piezoelectric transducer
SLM	selective laser melting
STL	standard tessellation language
Ta	tantalum
Ti6Al4V	titanium aluminum vanadium
TiTa	titanium tantalum
TEG	triboelectric generator
TJA	total joint arthroplasty
TKR	total knee replacement
UHMWPE	ultra high molecular weight polyethylene
V	shear force
WOMAC	Western Ontario and McMaster Universities Arthritis Index
Δ	deflection
ν	Poisson's ratio
σ_{vm}	von Mises stress
σ_y	yield strength

Chapter 1

1 Introduction

In this chapter, aspects of how the bones and soft tissue of the human knee joint achieve motion will be described. Diseases such as osteoarthritis (OA) can hinder joint function by affecting the structure and stability of the joint. Severe cases of OA can necessitate surgical treatments such as total knee replacements (TKR). Despite the restoration of joint function and reduction in joint pain due to TKR, complications can arise thus rendering the implant dysfunctional. Instrumented implants can provide quantitative feedback that can be used to direct actions towards the improvement of implant longevity and patient outcomes. The thesis rationale and research objectives will be outlined after an overview of the anatomy of the knee, TKR failure modes, current smart implant technologies, and how energy harvesting mechanisms, particularly the triboelectric effect, can be leveraged in measuring the loads transmitted in a total knee replacement.

1.1 Anatomical Movement Descriptors

1.1.1 Anatomical Terms Used to Describe Relative Position or Direction

The terms that are used to describe relative anatomical positions or directions are reviewed here. The term medial refers to a position relatively close to the midline of the body or a movement that moves toward the midline. Conversely, the term lateral refers to a position relatively far from the midline or a movement away from the midline. The term proximal refers to a position that is closer relative to a reference point, whereas the term distal refers to a position that is farther from a reference point. A segment or anatomical landmark is termed superior if it is above a reference point. If a segment or anatomical landmark is below a reference point, the segment or anatomical landmark is inferior. The position of an object or a movement that is relative to the front or back is anterior or posterior, respectively (Hamill and Knutzen, 2014).

1.1.2 Basic Movements

Flexion occurs when the relative angle of a joint between two adjacent segments decreases. Extension is the increase of the relative angle of a joint between two adjacent segments. Abduction is when a segment's movement is away from the midline. Adduction is the movement of a segment towards the midline. Internal and external rotations rotate about a vertical axis running through the segment. Internal rotation is the rotation directed toward the midline. External rotation is the rotation directed away from the midline (Hamill and Knutzen, 2014). Flexion/extension and internal/external rotation of the knee are illustrated in Figure 1-1.

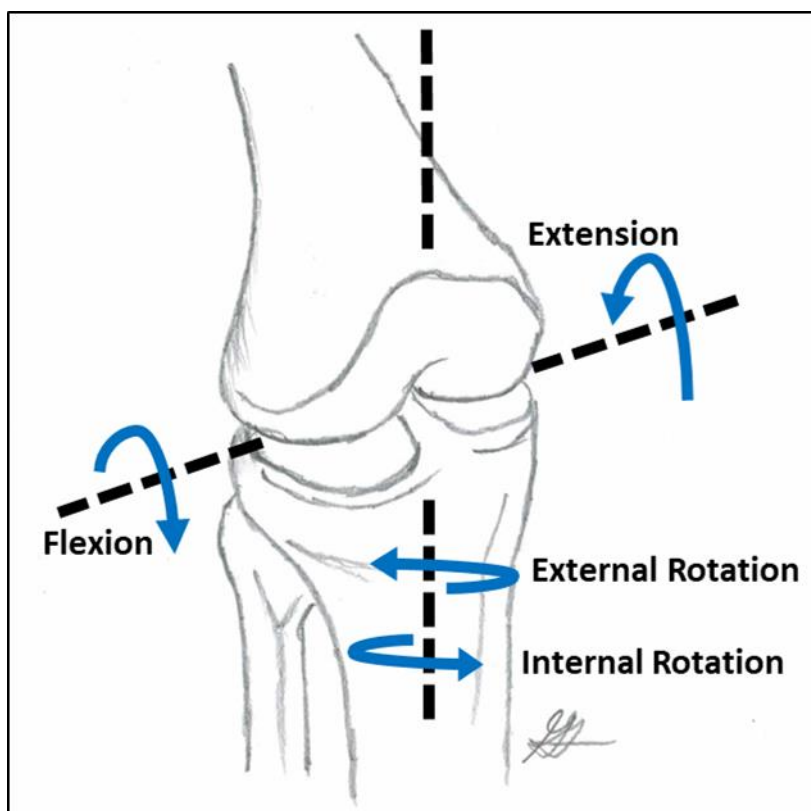


Figure 1-1- Primary movements of the knee (tibia with respect to the femur).

1.1.3 Cardinal Planes of the Body

Three cardinal planes intersect at the centre of mass of the body (Figure 1-2). The sagittal plane bisects the left and right sides of the body. The coronal or frontal plane bisects the body to create front and back halves. The transverse plane bisects the body to create top and bottom halves (Hamill and Knutzen, 2014).

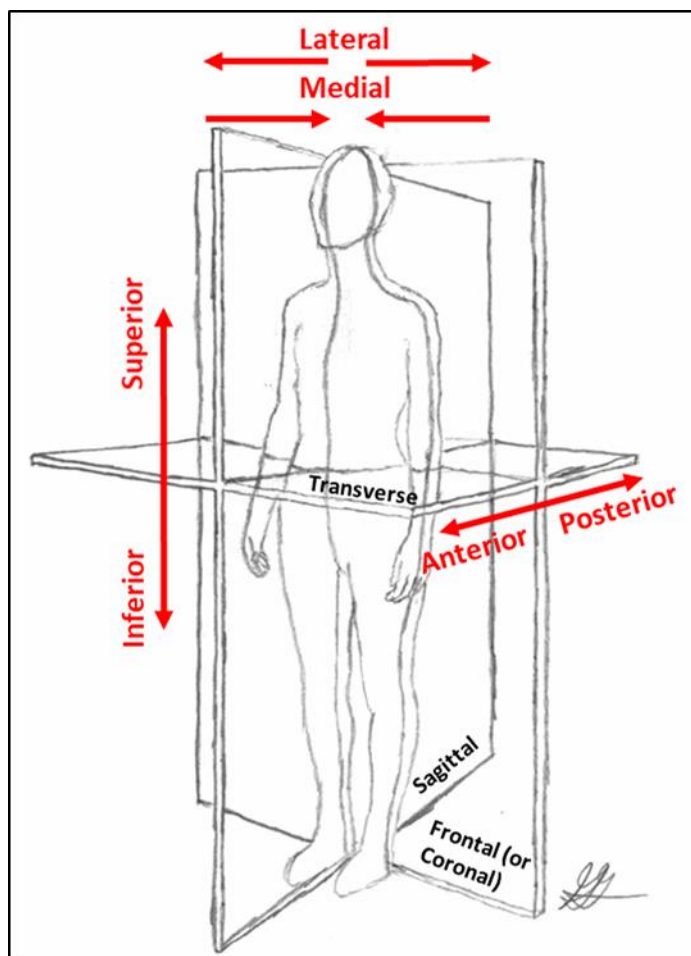


Figure 1-2-Cardinal Planes of the Human Body

1.2 Knee Anatomy

The knee primarily flexes and extends. Flexion is accompanied with a small, but significant amount of rotation. The knee is a mobile joint that is stabilized passively by

the ligaments, joint geometry, the active muscles, and the compressive forces pushing the bones together (Hamill and Knutzen, 2014). Joint function and stability are directly affected by the degeneration of the articulating surfaces of the joint, bones, ligaments, and the muscles. An overview of the aforementioned components of the knee will be discussed further in this chapter.

1.2.1 Osseous Anatomy of the Knee

The human knee joint is comprised of three articulating surfaces. They include the tibiofemoral joint, the patellofemoral joint, and the tibiofibular joint. Although all three of these articulations play a role in the kinematics and kinetics of the human knee joint, the tibiofemoral articulation will be emphasized. It is the largest articulation that transmits the largest loads. Therefore, the effects of musculoskeletal diseases in this articulation can be the most detrimental.

Tibiofemoral Joint

The tibiofemoral joint, as the name suggests, is where the tibia and the femur meet. On the distal femur, there are two large convex surfaces, the medial and lateral condyles. The medial and lateral condyles are separated by the intercondylar notch in the posterior region of the distal femur, whereas the patellar or trochlear groove is the anterior separation between the condyles (Hamill and Knutzen, 2014).

The features that differentiate the lateral condyle from its medial counterpart are the larger surface area, the flatter surface and the more prominent anterior extension (Hamill and Knutzen, 2014). The epicondyles, located above the condyles, serve as attachment points for ligaments, muscles and capsule. The condyles on the distal femur rest on the tibial plateau of the proximal tibia. The tibial plateau is separated into two regions: the medial and lateral tibial plateau. The oval-shaped, concave shape of the medial plateau articulates with the convex shape of the medial condyle. The shape of the lateral condyle can be described as circular and slightly convex. The surfaces of the medial compartment have a convex-concave relationship, whereas both articulating surfaces in the lateral

compartment are convex (Hamill and Knutzen, 2014). The osseous structure of the knee is shown in Figure 1-3. The geometric differences between the compartments allow the lateral condyle to translate along the anteroposterior direction during flexion and extension; this accommodates femoral roll-back during flexion and the screw-home mechanism during extension.

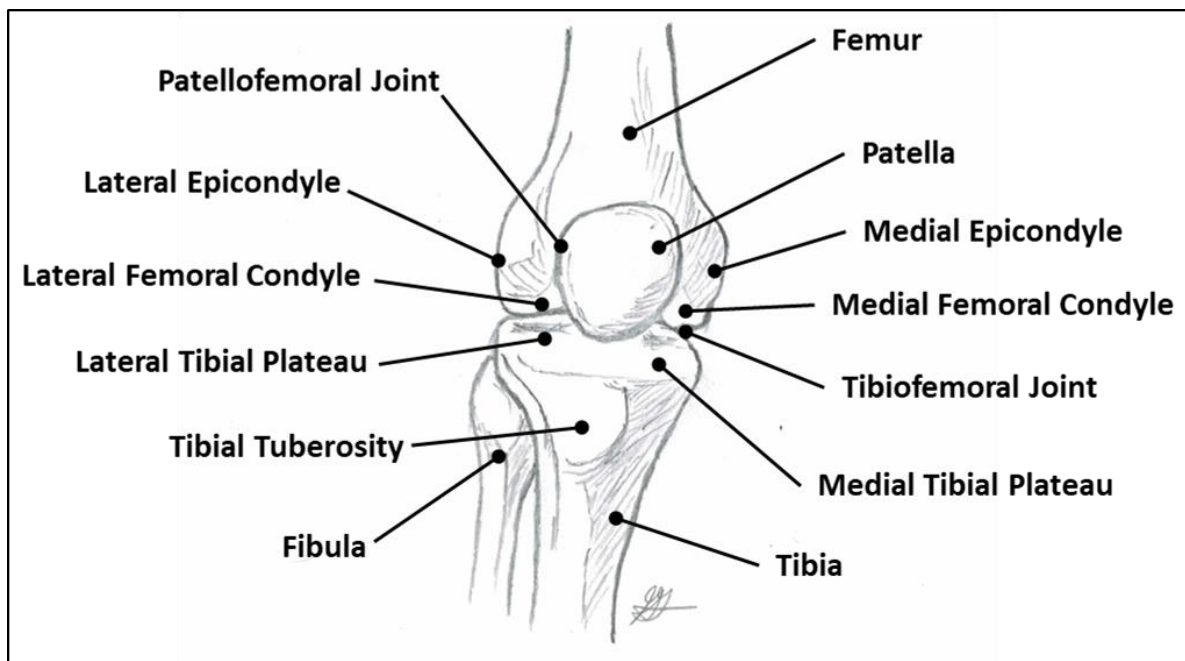


Figure 1-3- Osseous Anatomy of the Knee

1.2.2 Soft Tissue Anatomy of the Knee

The soft tissues, such as capsules, muscles and ligaments, are responsible for maintaining mechanical stability in the joint.

1.2.2.1 Knee Ligaments

The cruciate and collateral ligaments of the knee serve as passive restraints along the transverse and coronal planes (Figure 1-4). The patellar ligament connects the patella and

the tibia at the tibial tuberosity. This ligament is essential for the extensor mechanism to function properly (Hamill and Knutzen, 2014).

Cruciate Ligaments

There are two cruciate ligaments that are in the intercondylar space. The anterior cruciate ligament (ACL) restrains anterior translation of the femur relative to the tibia and internal-external rotation. The posterior cruciate ligament (PCL) restrains posterior translation of the femur relative to the tibia and internal rotation. The length of the PCL remains constant in external rotation (Hamill and Knutzen, 2014).

Collateral Ligaments

The collateral ligaments, located on the sides of the knee joint, restrain varus-valgus torques and provide some restraint to internal-external rotation. The medial collateral ligament (MCL) resists against valgus moments, or forces that act in the medial direction on the lateral side of the knee. The lateral collateral ligament (LCL) supports the knee against varus moments, or forces that are directed laterally on the medial side of the joint (Hamill and Knutzen, 2014).

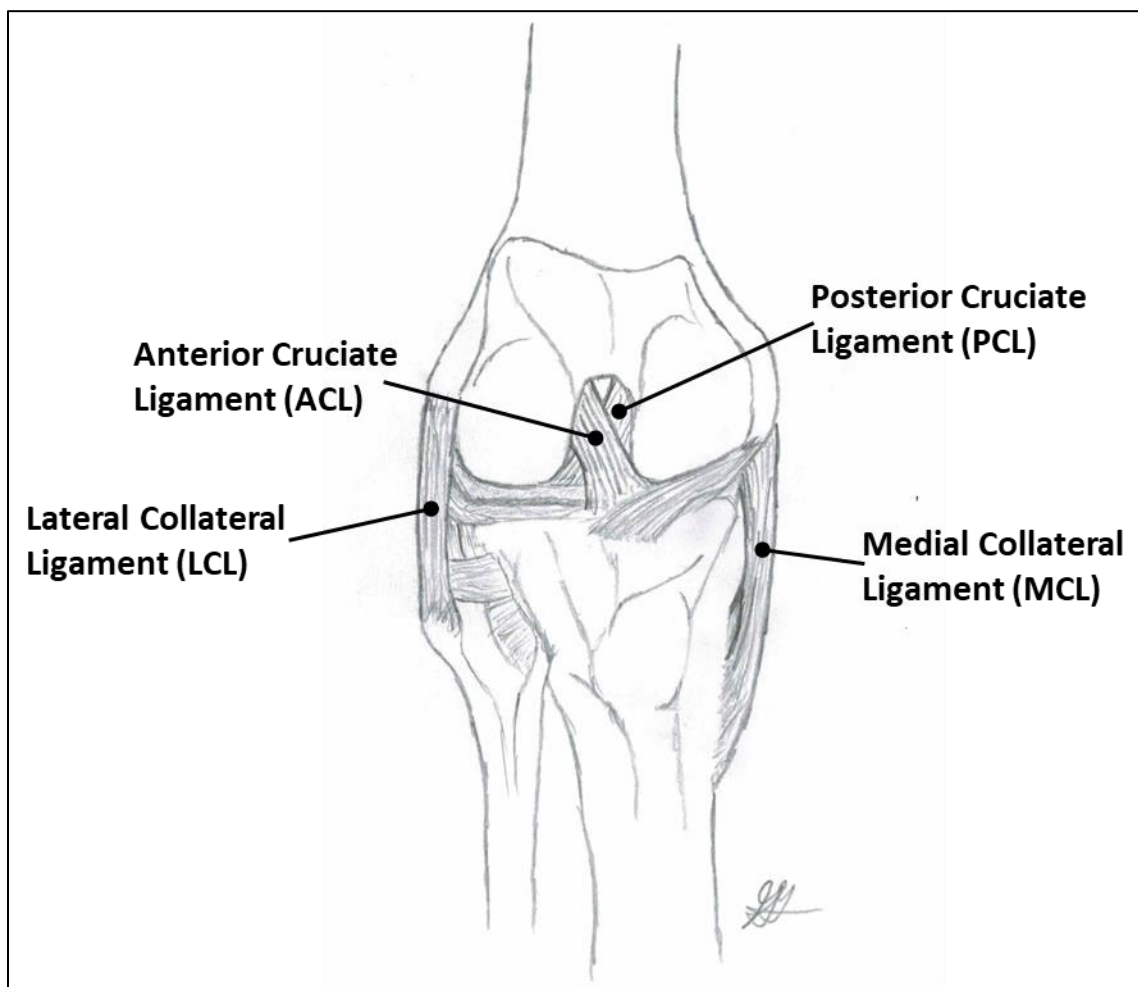


Figure 1-4- Cruciate and Collateral Ligaments

1.2.2.2 Muscles

The muscles surrounding the knee joint act as secondary stabilizers and produce motion (Figure 1-5). The quadriceps femoris, composed of the vastus lateralis, rectus femoris, vastus medialis and vastus intermedius, is connected to the patellar tendon. Extension is achieved from the contraction of these muscles. The biceps femoris, semimembranosus and semitendinosus make up the hamstrings. The hamstrings are responsible for knee flexion (Hamill and Knutzen, 2014).

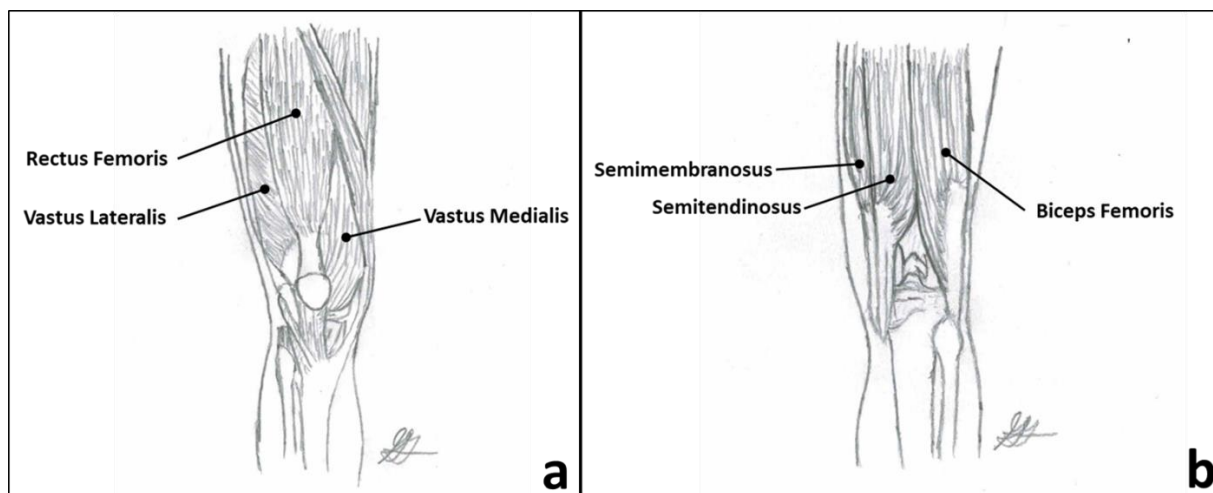


Figure 1-5- (a) Quadriceps: vastus lateralis, rectus femoris, vastus medialis and vastus intermedius (*under rectus femoris*) (Anterior View of the Knee), and (b) Hamstrings: biceps femoris, semimembranosus and semitendinosus (Posterior View of the Knee)

1.3 Knee Osteoarthritis

Osteoarthritis (OA) is a joint disease characterized by the degeneration of the articular cartilage covering the bones. Cartilage loss leads to pain and reduced joint function. This joint disease is usually understood to result from aging and wear-and-tear. However, the onset of arthritis is multifactorial. Although mechanical loading is one of the main factors, joint integrity, genetic predisposition, local inflammation, and cellular and biochemical processes contribute to the severity of OA (Lespasio et al., 2017).

There are signs and symptoms that are indicative of OA. Pain in the affected joint can vary from being dull, sharp, constant, and intermittent. In addition to this pain, the range of motion of the joint can be limited, and movement may not be smooth as a result of an absence of articular cartilage and the presence of osteophytes, or bone spurs. This, in turn, affects joint function. Radiographic images may be used to classify the severity of a patient's OA based on the identification of osteophytes, and joint space narrowing (JSN) (Figure 1-6). The presence of JSN is a prime indicator of an absence of articular cartilage.

The severity of OA can be graded using the Kellgren-Lawrence scale (KELLGREN and LAWRENCE, 1957). The grading scale ranges from 1 to 4. Kellgren and Lawrence grades from 1 to 3 can be treated with non-operative treatments such as weight loss, assistive devices, medications, and intra-articular knee injections. For Grade 4 OA, surgical options need to be considered. OA at this state has large osteophytes, marked JSN, severe sclerosis, and definite bone deformity (Lespasio et al., 2017). Joint reconstruction can restore joint function, alleviate pain, and improve quality of life.

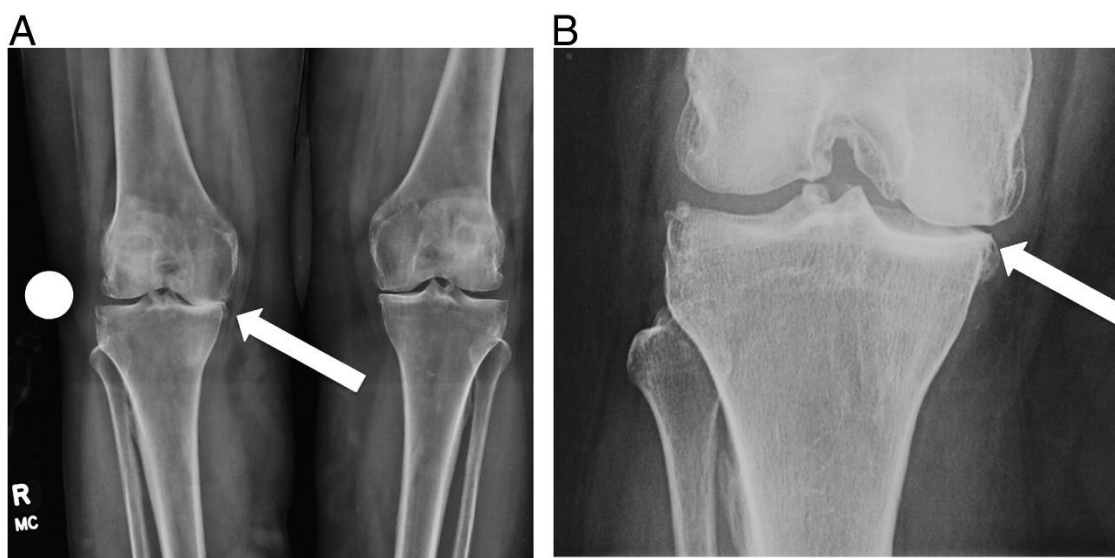


Figure 1-6- (A) The joint space narrowing and osteophyte formation in the anterior-posterior radiograph are indicative of bilateral medial osteoarthritis where joint space narrowing is greater in the right knee. (B) A magnified view of the right knee.

(Braun and Gold, 2012) (Image use permitted by Elsevier)

1.3.1 Prevalence of Knee Osteoarthritis

The knee is the most susceptible joint to OA (Bliddal and Christensen, 2009). Knee OA is more prevalent in the older population and in individuals with a higher body mass index (BMI). Increased joint loading due to obesity is not the only factor that contributes to the onset of OA in weight-bearing joints. Changes in body composition, negative

effects related to inflammation, the decrease of physical activity, and resulting loss of muscle strength from a sedentary lifestyle increase the risk of OA (Wluka et al., 2013). Obesity rates are expected to increase thereby increasing the incidence of knee OA and the need for knee arthroplasty (Bryan et al., 2013).

1.4 Total Knee Replacements

For Grade 4 OA, based on the Kellgren-Lawrence scale, total knee replacements (TKR) remains the most viable option for restoring joint function and pain relief. Implant designs can vary based on the required constraint. However, a TKR generally consists of a cobalt-chromium femoral component, a titanium tibial tray, and an ultra-high molecular weight polyethylene (UHMWPE) bearing (Figure 1-7). Most TKRs function with the removal of the ACL, but on rare occasions, it is not removed when a bi-cruciate retaining implant is used. The PCL is removed about half of the time. Therefore, there are different implant designs that compensate for the contributions of the removed ligaments. TKR does not solely remove the diseased tissue, but it also realigns the mechanical axes of the femur and the tibia in a way that replicates the load distribution in a healthy joint. The alignment and fixation of the TKR is imperative for implant longevity and ensuring patient satisfaction (Sikorski, 2008).

Material strength and durability of implants should be high enough to prevent yielding and fatigue failure from the stresses transmitted through the knee during activities of daily living (ADL). Knee implants, generally, should be durable enough to last about 15-20 years (Rönn et al., 2011).

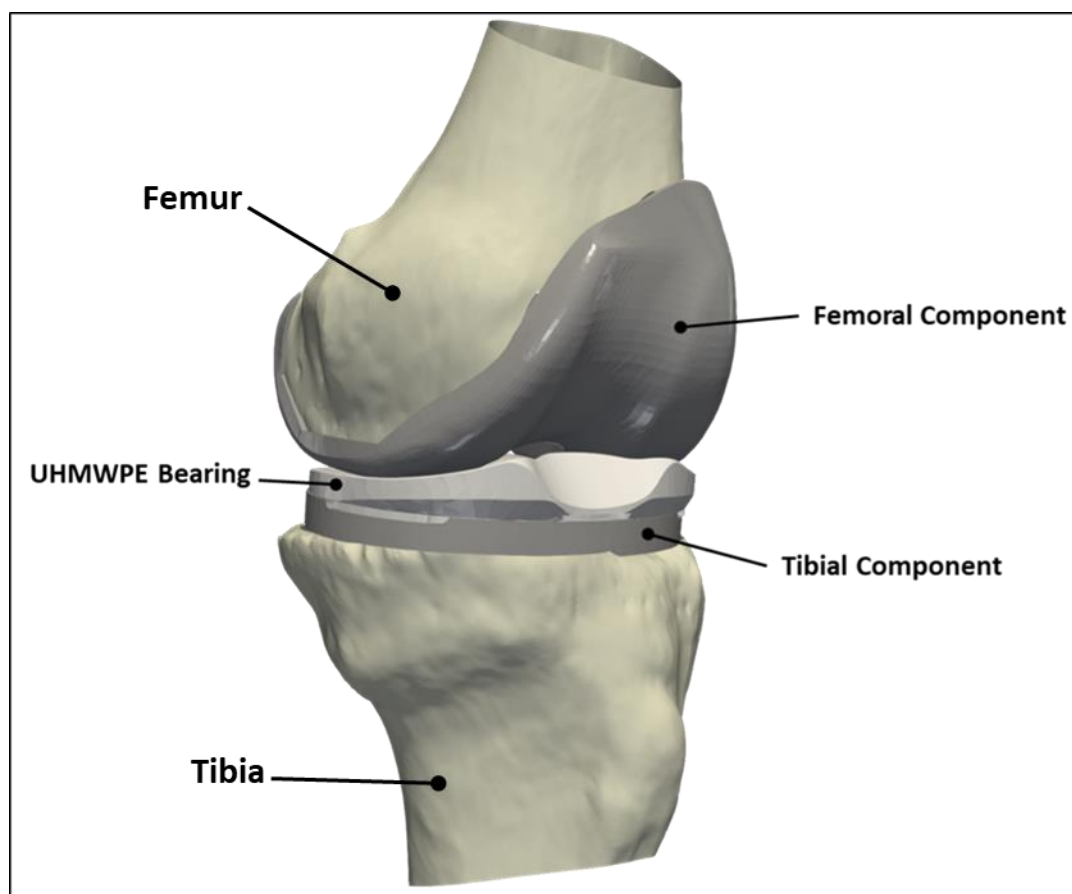


Figure 1-7- Total Knee Replacement Components

1.4.1 Prevalence of Total Knee Replacements

TKR cases are expected to increase in the next decade. In Canada, based on the Canadian Joint Registry, there has been a 17.0% increase in the TKR procedure volume from 2012 to 2017 (Canadian Institute for Health Information, 2018). In the United States, procedural volume for all total joint arthroplasties (TJA) rose by 38% between 2016 and 2017 (American Joint Replacement Registry, 2018). In both the United States and Canada, TKRs represents about 60% of all TJA procedures. Kurtz et al. projected a 673% increase in TKRs by 2030 when compared to the annual number of procedures in 2005. Based on their projection methodology, in 2030, 3.48 million procedures can be expected in the United States (Kurtz et al., 2007). In more recent studies, the projected increase in the number of TKRs is not as high. Sloan et al. projected that TKR procedures

in 2030 will be about half of what was envisioned by Kurtz et al.; 1.26 million procedures are expected based on a linear estimate (Sloan et al., 2018). Nevertheless, TKR procedures are expected to be in high demand in the future.

There are several factors that are contributing to the increase of TKR procedures. With medical and technological improvements, life expectancies have increased in developed countries. In countries such as the UK, Japan, Canada, and Australia, life expectancies are 80 and 83 years for men and women, respectively (Hamilton et al., 2015). Another trend that may be connected to the increase in TKR procedures is the increasing incidence in active, younger adults (Weinstein et al., 2013). Another risk factor that is contributing to the projected increase in TKR is the higher prevalence of obesity. Obesity has been associated with earlier cases of moderate to severe OA (Coggon et al., 2001; Doherty, 2001; Gillespie and Porteous, 2007; Harms et al., 2007; Vasarhelyi and MacDonald, 2012). In Canada and the United States, from the late 1980s to 2009, there was approximately a 10% increase in the prevalence of obesity (Shields et al., 2011; Vasarhelyi and MacDonald, 2012). Factors such as longer life expectancies, obesity and TKR performed earlier in life can result in not only in an increase in primary TKR procedures, but can warrant the need for a revision, and possibly a re-revision surgery, as patients outlive their knee prostheses.

1.4.2 Complications in Total Knee Arthroplasty

Despite the success of the majority of primary TKRs, some patients may experience pain, stiffness, and instability. In some cases, based on clinical diagnoses, revision surgery may be considered. Infection, instability, and loosening have been the most common reasons for revision surgery (Gaizo et al., 2011; Vince et al., 2006; Wilson et al., 2017). Joint instability and aseptic loosening are both mechanical in nature and are both sensitive to implant design and surgical technique.

Instability can result from muscle weakness, improper implant sizing, and ligament imbalance which can alter the loading of components (Abdel and Haas, 2014; Petrie and

Haidukewych, 2016; Vince et al., 2006). Changes to the loading pattern of implant components can lead to excessive stress and motion which can lead to component damage. Osteolysis can affect the integrity of the surrounding bone structures which can lead to implant loosening. Misalignment of TKR components resulting from surgical error can contribute to physiologically incorrect loading thus introducing high stresses that can lead to the mechanical failure of implant components. Abnormal loading patterns and biological changes can affect a TKR's articulation which may result in premature prosthesis failure (Gaizo et al., 2011; Vince et al., 2006; Wilson et al., 2017).

1.4.2.1 Instability

Instability consistently remains one of the most common modes of implant failure (Dalury et al., 2013; Sharkey et al., 2014; Vince et al., 2006; Wilson et al., 2017).

Instability accounts for 10 to 22% of revisions (Abdel and Haas, 2014; Callaghan et al., 2004; Parratte and Pagnano, 2008; Vince, 2003; Yercan et al., 2005a, 2005b). A reconstructed knee is unstable when the implant and surrounding tissue do not provide sufficient restraint against the secondary joint motion when compared to a healthy, intact joint. The lack of restraint can lead to excessive relative motion between the articulating surfaces of the knee. Obvious visual signs of dislocation are indicative of instability.

Dislocations can take the form of varus, valgus, or recurvatum deformities. Symptoms of instability include pain, recurrent knee effusion, restricted motion, giving-way, a sense of rubbing between the components, or "locking" of the knee (Yercan et al., 2005b).

Component loosening, prosthetic breakage, component size or position, fracture, polyethylene bearing wear, and collateral ligament failure can lead to instability (Vince et al., 2006). There are three types of instability proposed by Parratte and Pagnano: extension instability, flexion instability, and genu recurvatum (Chang et al., 2014; Parratte and Pagnano, 2008). When soft tissue balancing is performed, the objective is to balance the tibial forces along the mediolateral and anteroposterior axes while not over constraining the joint.

1.4.2.2 Aseptic Loosening

Successful prostheses have a solid fixation, and thus no relative motion between the implant and bone they are implanted in. The infection of surrounding tissues in a TKR can cause components to loosen by weakening the periprosthetic bond at the implant-bone interface. However, aseptic loosening can arise when the implant-bone fixation is weakened, not from necrotic tissue, but what is commonly believed to result from wear-induced osteolysis. In TKRs, particulate debris usually originates from the UHMWPE bearing. The presence of wear debris elicits a foreign-body reaction. Wear debris triggers the creation of cytokines. The higher concentration of cytokines promotes osteoclast differentiation and activity thus perpetuating bone resorption. Additionally, wear debris inhibits bone formation by affecting osteoblast progenitor cells (Jiang et al., 2013; Saleh et al., 2004). This leads to periprosthetic bone loss or osteolysis. However, in recent years, the technological advancements in the design and manufacturing of highly crosslinked UHMWPE have reduced the degradation and wear of UHMWPE bearings, but fatigue remains a concern (Collier et al., 2005; Medel et al., 2009). Signs, or the presence, of aseptic loosening, can be identified as radiolucent zones at the implant-bone interface (Rosenthal, 1997) (Figure 1-8).

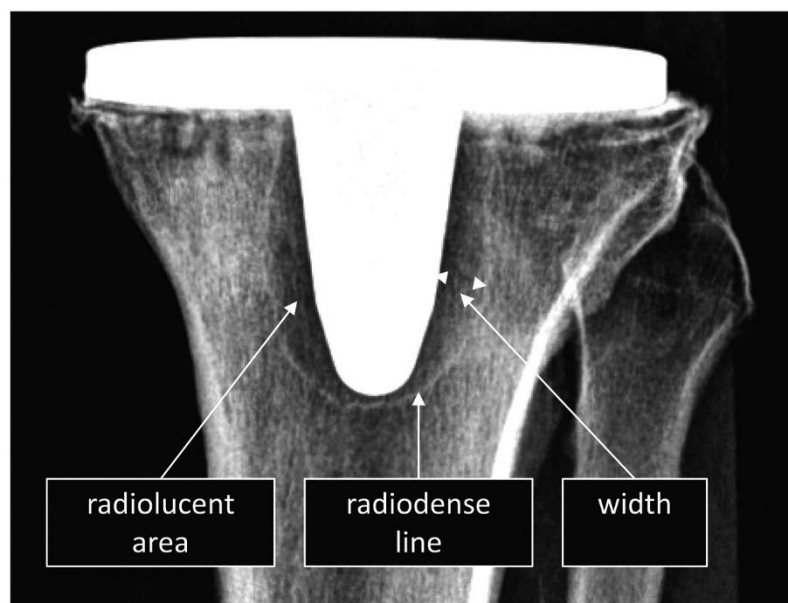


Figure 1-8-Radiolucent Lines Surrounding the Tibial Stem (Kutzner et al., 2018)

(Image use permitted by Taylor and Francis)

Aseptic loosening is not always associated with osteolysis. Micromotion can lead to insufficient primary fixation or impede osseointegration. Large micromotion can lead to fibrous tissue formation in the implant-bone interface. Increased relative motion between the implant and bone can enlarge the effective joint space and increase the amount of cement and metal wear particles. Stress shielding, high fluid pressure due to the inflammatory response, materials of articulating surfaces, and individual variations can also contribute to aseptic loosening (Sundfeldt et al., 2006). Continuous measurement of the tibial forces can detect the effect of load imbalances have on bone remodeling and the progression of failure modes such as instability and aseptic loosening.

1.4.3 Revision Total Knee Arthroplasty

The revision burden for TKR, in 2017, was 6.9% and 5% in Canada and the United States, respectively (American Joint Replacement Registry, 2018; Canadian Institute for Health Information, 2018). Revision burden is the proportion of revision surgeries performed out of all TKR. The revision burden in both countries has remained constant

from 2012 to 2017. With the increasing prevalence of TKR, an increase in the procedure volume of revision TKR will be expected despite the consistent revision burden in recent years.

Reiterating the impact associated with obesity on OA, obesity can lead to complications that can affect the outcome of a primary TKR procedure. Obese patients, younger than 60 years of age, are more likely to undergo a revision TKR procedure. Heavier, active patients tend to have decreased implant survivorship (Foran et al., 2004; Vazquez-Vela Johnson et al., 2003). Overall, the increased joint loading in obese patients can decrease the success of a TKR procedure thus warranting revision TKRs.

Based on the prevalence of obesity, the projected increase in TKR procedures, an aging population, and younger individuals requiring a TKR, revision TKR will become more prevalent. Revision TKR is more complex than a primary TKR. It is a more costly and complex procedure (Kurtz et al., 2005). Revision TKR presents challenges that can adversely affect the outcome of the surgery. Detailed planning based on the implant failure mode determined from clinical history, examination, analysis of radiographs and laboratory tests must be undertaken (Hamilton et al., 2015). Removal of the primary TKR components can be challenging if there isn't adequate exposure. Long stems, augments, and osseous-integrative materials are commonly used to compensate for tissue loss when the primary TKR is removed (Dennis et al., 2018; Mason and Fehring, 2006). Due to the challenges associated with revision TKR, revision TKR do not replicate the same implant survival rates and patient outcomes as the primary TKR.

Based on the undesirable aspects of revision surgeries, the ability to acquire quantitative feedback of the forces transmitted through a load-sensing implant can possibly mitigate implant failures that are mechanical in nature such as instability and aseptic loosening. By understanding the *in vivo* tibial forces, suitable interventions that restore the load distribution within the knee to an established, objective target, can be implemented to improve implant survivorship, thus reducing the procedure volume of revision surgeries.

1.5 Instrumented Implants

In order to address the complications that occur with TKR, instrumented implants can be utilized to better understand the etiology of implant failure. Implants equipped with load sensors can provide quantitative data that can be used to corroborate a patient's history when issues arise, or more importantly, predict precursors of implant failure.

Instrumented implants have a potential of supplementing current diagnostic tools such as radiographic images and laboratory tests.

1.5.1 Intraoperative Load Sensors

Soft tissue imbalances in TKR can be detrimental to implant survivorship and patient outcomes (Babazadeh et al., 2009; Parratte and Pagnano, 2008; Sharkey et al., 2014; Unitt et al., 2008; Whiteside, 2002). Inadequate soft tissue balance can be the precursor to instability, premature implant wear, and aseptic loosening. Required bone resections, ligament releases, and rotations are judged based on the subjective tactile assessment of the surgeon (Gustke et al., 2014a). Despite the importance of a correctly aligned and well-balanced TKR, a quantitative standard that defines a well-balanced knee has not been established (Gustke et al., 2014b).

The Verasense Knee System (Orthosensor, Dania FL) was developed for the purpose of measuring the forces transmitted in the medial and lateral compartments of the joint during the preliminary sizing and positioning of components during TKR surgery. This instrumented tibial tray insert trial provides real-time force feedback and the locations of peak tibiofemoral forces throughout the knee's full range of motion. With the quantitative feedback of the mediolateral force distribution, soft tissue balancing can be evaluated and corrected accordingly based on an objective basis.

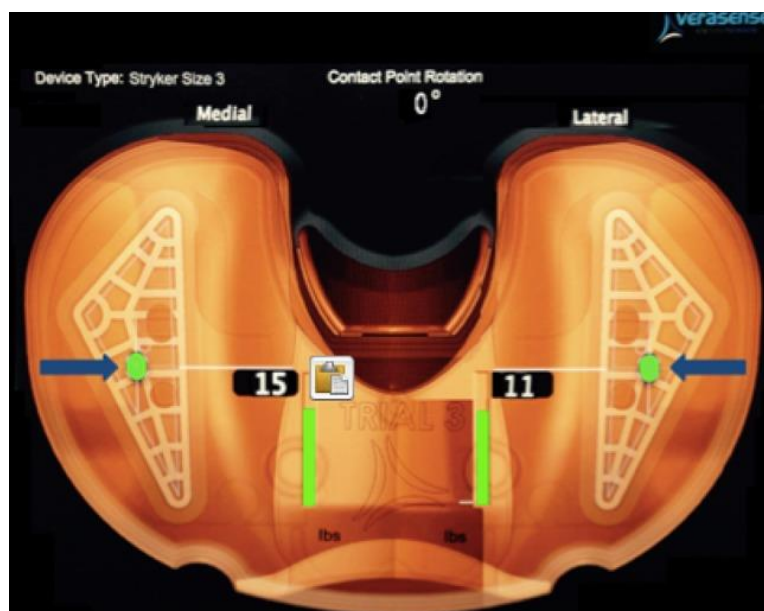


Figure 1-9- Verasense Display (Manning et al., 2018) (Image use permitted by Creative Commons (<https://creativecommons.org/licenses/by/4.0/>))

Measuring the intercompartmental loads using the Verasense Knee System, for acquiring a desired mediolateral load distribution, has shown favourable short-term outcomes (Cho et al., 2018; Elmallah et al., 2016; Gustke et al., 2014b; Gustke et al., 2014; Meneghini et al., 2016a; Risitano et al., 2017a). The Western Ontario and McMaster Universities Arthritis Index (WOMAC) (Bellamy et al., 1988) and the American Knee Society Scoring System (KSS) (Noble et al., 2012; Scuderi et al., 2012) have been commonly used to measure patient reported outcome measures (PROMs) before and after TKR. Both scoring systems evaluate pain, stiffness, and physical function. A higher WOMAC score indicates worse pain, stiffness, and functional limitations, whereas a higher KSS score reflects improvement. Gustke et al. observed that KSS and WOMAC scores indicated better improvement in the quantifiably balanced (intercompartmental load difference of < 15 lbs) group versus the quantifiably unbalanced group six months post-operatively. The improvements in the PROMs of the balanced group are reflected by the increased activity levels. This may be the result of better performance in post-operative physiotherapy from the more favourable biomechanics stemming from the intraoperative

compartmental measurements (Gustke et al., 2014b). However, the course of healing can change over time, and because of the lack of *in vivo* load measurements, the objective targets used in soft tissue balancing with the aid of an intraoperative sensor like the Verasense cannot be validated.

Intraoperative sensors, in conjunction with an established objective load target, may be beneficial in preventing instability, loosening, and implant wear in the short term. However, the load balance, even when determined objectively with an intraoperative sensor, may change over the course of healing. Successfully achieving the optimal intercompartmental load distribution intraoperatively does not guarantee immunity from complications. Embedded sensors in TKR components can monitor patients' activity levels and improve our understanding of *in vivo* knee mechanics. With instrumented implants, quantitative evidence of patient outcomes can possibly support how intraoperative sensors are used for TKR.

1.5.2 Postoperative Load Sensors

Load sensors have been used to measure forces and moments in the shoulder, hip, knee, and spine. Due to the scope of this project, relevant work related to the instrumentation of knee implants measuring tibial forces will be outlined.

The first instrumented knee implant that was used to measure forces *in vivo* was developed by D'Lima et al (Figure 1-10). Four transducers were placed at the four corners of the tibial tray in order to measure the total axial force and determining the center of pressure. The microtransmitter, power induction coil, and antenna were housed within the stem of the tibial component. During use, inductive coupling was used to power the transducers and telemetry system wirelessly. The participant was instructed to perform a set of activities of daily living including gait, stair ascent, stair descent, sit-stand, stand-sit, and cycling, during which knee loads were recorded (D'lima et al., 2005a).

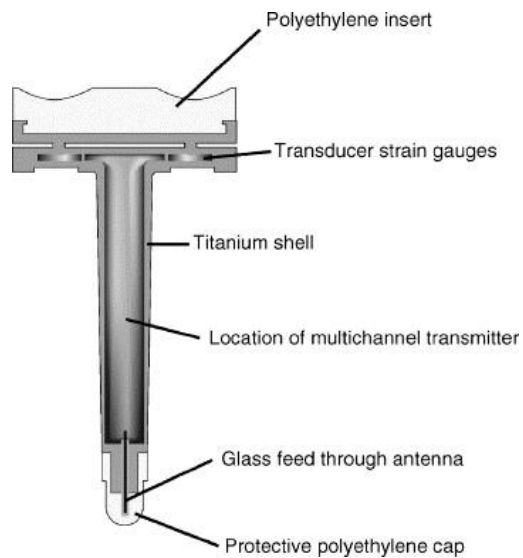


Figure 1-10- Instrumented implant developed by D’Lima et al. with four transducers located at the four corners of the tibial tray (D’lima et al., 2005b) (Image use permitted by Elsevier)

Kirking et al. developed an instrumented implant capable of measuring all six load components (Kirking et al., 2006). The telemetry system, and mechanism for powering the microtransmitter and load cells used an identical set-up as D’Lima et al (D’lima et al., 2005a). The instrumented design was accurate with a highly linear response ($R^2 > 0.997$) when comparing the measured loads of the instrumented implant and the applied external loads. Power was consistently supplied at approximately 40 mW via induction coupling. The net signal integrity, of the wireless transmission of all components of loading, was greater than 98%. Overall, this instrumented implant design was able to wirelessly transmit accurate load data based on the applied uniaxial loading along each axis, and during a sinusoidal dynamic loading scenario.

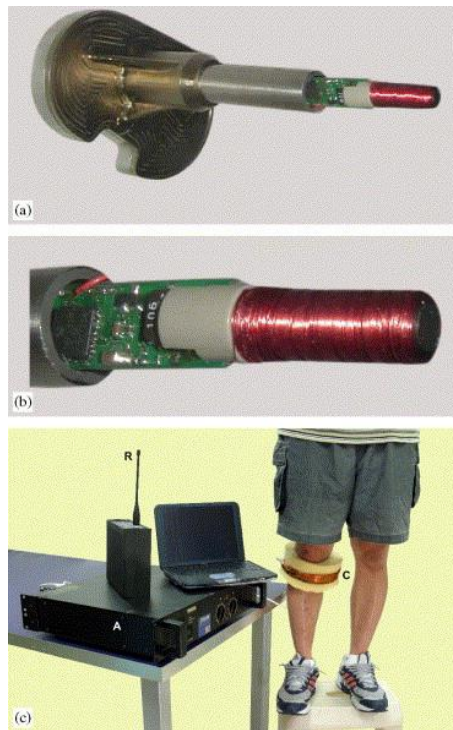


Figure 1-11- (a) Tibial tray with telemetry system, (b) magnified view of the microprocessor and the internal power induction coil, (c) patient with external coil for powering the onboard electronics and telemetry system. (Kirking et al., 2006)

(Image use permitted by Elsevier)

Another design by Bergmann et al., similar to what was developed by Kirking et al., was tested *in vivo*. Strain gauges were embedded in a tibial component that transmitted load data using an inductively powered telemetry system. The design of their instrumented tibial component was able to measure the six load components.

Although powering strain gauges and telemetry systems using induction coupling has proved to be an effective means of measuring and transmitting tibiofemoral contact forces accurately and reliably, this method of power transmission is inherently cumbersome. An external coil must be donned by the individual. Therefore, powering the electronics for smart implants remains a limiting factor. With the advancements in micro-electromechanical and nano-electromechanical systems (MEMS and NEMS,

respectively), more compact methods of measurement, and power generation can be developed. Energy harvesting mechanisms can be used for load acquisition and power generation.

In recent years, piezoelectric transduction has been a mechanism that has been explored. Safaei et al. conceptualized the idea of embedding piezoelectric transducers (PZT) in the polyethylene insert. By locating transducers in the anteromedial, anterolateral, posteromedial, and posterolateral regions of the polyethylene bearing, the center of pressure can be determined on the tibiofemoral joint. Safaei et al. performed preliminary testing with a simplified model of this concept by embedding a single PZT in a polyethylene disk (Safaei et al., 2017). The vertical component of the gait cycle was applied to this simplified prototype. Biomechanical modeling, finite element analysis and electromechanical modeling were conducted in the design phase preceding the experiments (Safaei et al., 2018).

Platt et al. were the first to place piezoelectric ceramics in an altered tibial tray. PZTs were placed in the anterior, posteromedial, and posterolateral locations of the tibial plateau. The prototype was able to generate 850 μW of continuous regulated power. The PZT elements were deemed to have the longevity required in TKR applications. A single PZT element was axially compressed with an ISO knee load profile for up to 20 million cycles. A 17% decrease in power output was measured when compared to the initial power output. Therefore, the use of PZT elements integrated into TKR components in the hopes of powering low power microprocessors and sensors has shown some promise (Platt et al., 2005).

Almouahed et al. developed a concept that echoes aspects of Safaei et al. and Platt et al.'s work. The prototype had four PZT placed in the four corners of a custom-made tibial component, instead of the PE bearing. This design also measured the COP of the applied axial load. In previous iterations of this prototype, there were some drawbacks present. The top layer of the PZTs was torn off due to shear forces. Power generation was not optimized due to the geometry of the PZTs. The power generated was proportional to the

height, and inversely proportional to the surface area (Almouahed et al., 2017). One limitation in Platt et al.'s design was the overall thickness of the tibial baseplate that measured at least 22 mm in height. Almouahed et al reduced the thickness of the baseplate with the PZTs to 6.65 mm in their design. Removing a large amount of bone during TKR would jeopardize the success of possible revision TKRs (Almouahed et al., 2011).

Electromagnetic induction was another method used for energy harvesting purposes. Luciano et al.'s design consisted of an altered rotating hinge TKR. A coil of wire was spooled around the hinge of the TKR. In order to leverage Faraday's law of induction, magnets were embedded in a femoral component. During the swing phase, the femoral component would translate along a curvilinear path during flexion and extension. This design could generate 1.7 mW of power every 7.6 s (Luciano et al., 2014). The main limitations are the feasibility of making the necessary changes to the TKR components to recreate this design and the use of an overly constrained TKR system that is generally used for revision surgeries.

1.5.3 Triboelectric Effect

Another mechanism that can be utilized in energy harvesting is the triboelectric effect. The triboelectric effect is electrification induced by contact and friction between two interfacing materials (Wang, 2013). This phenomenon can be used for energy harvesting and load sensing applications (F.-R. R. Fan et al., 2012; Lin et al., 2013; Zhang et al., 2014). For the purposes of measuring loads in a TKR, a design that utilizes the contact-separation between a metal and a dielectric is the most suitable for harvesting energy while measuring *in vivo* loads during activities of daily living.

The contact-separation mode operates based on the cyclic compression applied to the triboelectric generator (TEG). Stacked structures are generally used for this triboelectrification modality. Materials selected for the stacked structure is an important consideration. A larger disparity in the polarities between the contacting materials

increases the charge transferred in the TEG (Wang, 2013). In other words, contacting materials with opposite polarities on the triboelectric series will generate more power. The top and bottom layers of the stacked structure act as electrodes. The material of choice for the electrodes tends towards a positive polarity like aluminum, for instance. A material with a negative polarity, like polydimethylsiloxane (PDMS), is secured to the top surface of the bottom electrode (F.-R. R. Fan et al., 2012; Wang, 2013, 2014). Therefore, the top layer comes into contact with the dielectric when the TEG is loaded, and separation between the layers occurs when the TEG is unloaded.

The contact and separation of the metal and dielectric layers allow the electron transfer between the electrodes. As the metal layer comes into contact with the dielectric, electrons from the metal layer are transferred to the dielectric layer. At full compression of the layers, the metal layer is positively charged whereas the bottom layer becomes negatively charged. As the metal layer separates from the dielectric, electrons transfer back to the positively charged metal layer. At full separation, the TEG is restored to a neutral state as the triboelectric and electrostatic charges equalize. The cyclic change of electron flow direction creates an alternating current (Figure 1-12) (Ibrahim et al., 2019a; Wang, 2013).

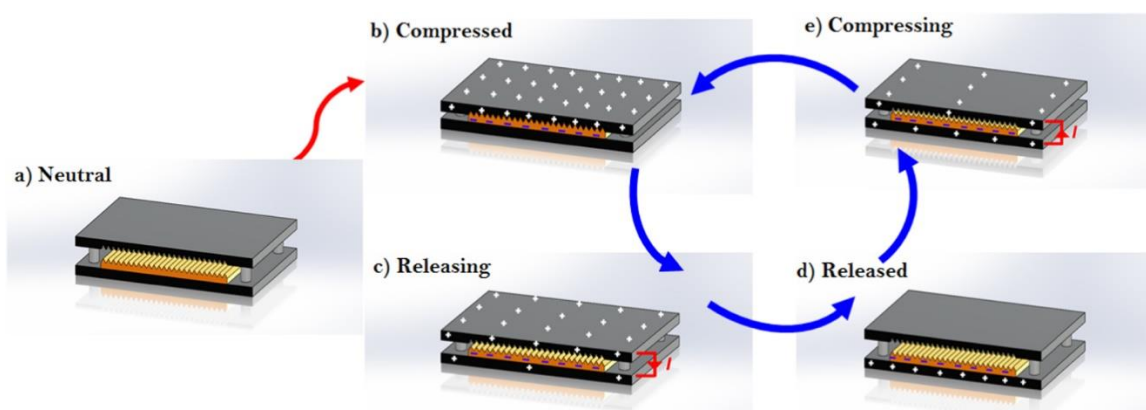


Figure 1-12- Triboelectric Working Mechanism (Ibrahim et al., 2019a) (Image use permitted by IOP Publishing)

In addition to using a metal-to-dielectric surface interface with materials on the opposite end of the triboelectric scale, the volumetric charge density can also be enhanced by changing the geometry of the contacting surfaces. Micro- and nano-patterns on the contacting surfaces can increase the surface area thus improving triboelectrification (F.-R. Fan et al., 2012; Wang, 2013).

Ibrahim et al. developed a TEG with the intention of instrumenting a TKR (Ibrahim et al., 2019a, 2019b, 2018). Material selection and patterns of the contacting surfaces were considered to maximize the electric charge between a metal-to-dielectric interface in a vertical contact-separation mode-based TEG. Titanium and PDMS were used in the TEG due to the opposite polarities of the said materials on the triboelectric series. As a means of increasing the contact surface area, matching saw-tooth ridges were fabricated on the contacting surfaces of the titanium and PDMS layers (Figure 1-13) (Ibrahim et al., 2019a). However, these TEGs require a relatively large compression distance (0.2 mm) to be able to operate, therefore a compliant package is needed to integrate the TEGs with a TKR.

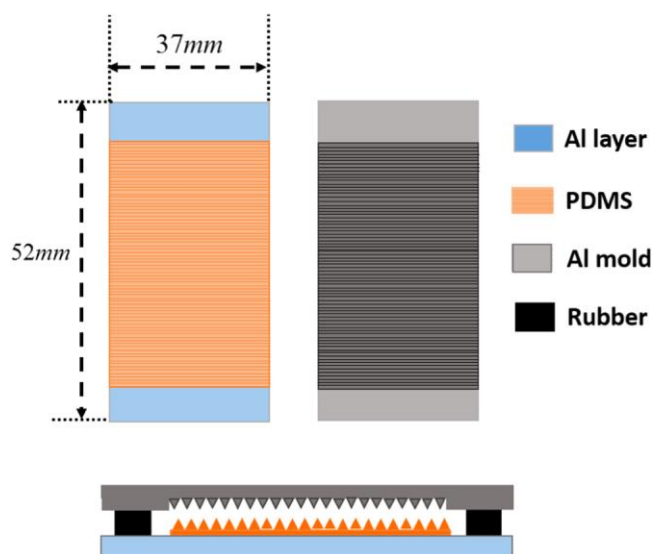


Figure 1-13- Saw-tooth ridges of metal and dielectric layers (Ibrahim et al., 2019a)

(Image use permitted by IOP Publishing)

1.6 Thesis Rationale

Currently, there are no commercially available means of continuously monitoring load transfer through TKR knees. Energy harvesting mechanisms can be of utility in powering instrumented knee implants. The triboelectric effect is the energy harvesting mechanism investigated by our group for the purpose of measuring tibiofemoral contact forces. Measuring these forces in uninhibited ADL can provide valuable quantitative feedback on the condition of a patient's knee years after a TKR procedure. There are several benefits of acquiring the *in vivo* loads postoperatively. The load data can be used to refine surgical techniques, such as soft-tissue balancing and implant alignment, which is critical to a well-functioning TKR. By monitoring patient activity levels, patients, therapists, and surgeons can be alerted of problems that can possibly be addressed early to avoid a revision surgery. With a better understanding of the loads and demands placed on implants, future implant designs can be improved. Therefore, there is a need for self-powering systems capable of quantifying tibiofemoral forces after TKR procedures.

Theoretically, TEGs in an instrumented knee implant has shown promise. However, there is still a need for further development before these devices can be integrated into commercially available TKR systems. The shear forces in ADL can damage the contacting surfaces of the TEGs. The TEGs are capable of generating electricity only when cyclic contact and full separation between the contacting layers occurs. A compliant durable package, designed to interlock between the UHMWPE bearing and tibial tray, can ensure the contact and separation of the TEG layers during the cyclic loading in ADL. In this thesis, the design and the analysis of the mechanical behaviour of a 3D printed titanium package prototype is outlined.

1.7 Research Objectives

The objectives of this study were:

1. Design a compliant package that houses the TEGs, and interlocks with a commercially available polyethylene insert and tibial tray.

2. Characterize and validate the stiffness of the compliant package when subjected to gait loading. The package's resistance to shear forces was measured.
3. Assess possible damage in the energy harvester package resulting from durability testing under simulated gait.
4. Develop computational models of the package that quantify its sensitivity to different size PE bearing thicknesses. Differences in the deflection and peak stresses were also measured between loading scenarios that account for all six components of loading and uniaxial loading.

1.8 References

- Abdel, M.P., Haas, S.B., 2014. The unstable knee: Wobble and Buckle. *Bone Jt. J.* 96B, 112–114. <https://doi.org/10.1302/0301-620X.96B11.34325>
- Almouahed, S., Gouriou, M., Hamitouche, C., Stindel, E., Roux, C., 2011. The use of piezoceramics as electrical energy harvesters within instrumented knee implant during walking. *IEEE/ASME Trans. Mechatronics* 16, 799–807. <https://doi.org/10.1109/TMECH.2011.2159512>
- Almouahed, S., Hamitouche, C., Stindel, E., 2017. Optimized Prototype of Instrumented Knee Implant: Experimental Validation. *IRBM* 38, 250–255. <https://doi.org/10.1016/J.IRBM.2017.06.005>
- American Joint Replacement Registry, 2018. Fifth AJRR Annual Report on Hip and Knee Arthroplasty Data 2018, American Joint Replacement Registry. <https://doi.org/1.1>
- Babazadeh, S., Stoney, J.D., Lim, K., Choong, P.F.M., 2009. The relevance of ligament balancing in total knee arthroplasty: how important is it? A systematic review of the literature. *Orthop. Rev. (Pavia)*. 1, e26. <https://doi.org/10.4081/or.2009.e26>
- Bellamy, N., Buchanan, W.W., Goldsmith, C.H., Campbell, J., Stitt, L.W., 1988. Validation study of WOMAC: a health status instrument for measuring clinically important patient relevant outcomes to antirheumatic drug therapy in patients with osteoarthritis of the hip or knee. *J. Rheumatol.* 15, 1833–40.
- Bliddal, H., Christensen, R., 2009. The treatment and prevention of knee osteoarthritis: a tool for clinical decision-making. *Expert Opin. Pharmacother.* 10, 1793–1804. <https://doi.org/10.1517/14656560903018911>
- Braun, H.J., Gold, G.E., 2012. Diagnosis of osteoarthritis: Imaging. *Bone* 51, 278–288. <https://doi.org/10.1016/j.bone.2011.11.019>

- Bryan, D., Parvizi, J., Austin, M., Backe, H., Valle, C. Della, Kolessar, D.J., Kreuzer, S., Malinzak, R., Masri, B., McGrory, B.J., Mochel, D., Yates, A., 2013. Obesity and total joint arthroplasty. A literature based review. *J. Arthroplasty*.
<https://doi.org/10.1016/j.arth.2013.02.011>
- Callaghan, J.J., O'Rourke, M.R., Saleh, K.J., 2004. Why knees fail. *J. Arthroplasty* 19, 31–34. <https://doi.org/10.1016/j.arth.2004.02.015>
- Canadian Institute for Health Information, 2018. Hip and Knee Replacements in Canada , 2017 – 2018: Canadian Joint Replacement Registry Annual Report. Ottawa, ON.
- Chang, M.J., Lim, H., Lee, N.R., Moon, Y.-W., 2014. Diagnosis, Causes and Treatments of Instability Following Total Knee Arthroplasty. *Knee Surg. Relat. Res.* 26, 61–67. <https://doi.org/10.5792/ksrr.2014.26.2.61>
- Cho, K.-J., Seon, J.-K., Jang, W.-Y., Park, C.-G., Song, E.-K., 2018. Objective quantification of ligament balancing using VERASENSE in measured resection and modified gap balance total knee arthroplasty. *BMC Musculoskelet. Disord.* 19, 266. <https://doi.org/10.1186/S12891-018-2190-8>
- Coggon, D., Reading, I., Croft, P., McLaren, M., Barrett, D., Cooper, C., 2001. Knee osteoarthritis and obesity. *Int. J. Obes.* 25, 622–627. <https://doi.org/10.1038/sj.ijo.0801585>
- Collier, M., EnghJr, C., Mcauley, J., 2005. Osteolysis After Total Knee Arthroplasty: Influence of Tibial Baseplate Surface Finish and Sterilization of Polyethylene Insert Findings at Five to Ten Years. *J. Bone ...* 2702–2708.
- D'lima, D.D., Patil, S., Steklov, N., Slamin, J.E., Colwell, C.W., 2005a. THE CHITRANJAN RANAWAT AWARD In Vivo Knee Forces after Total Knee Arthroplasty. <https://doi.org/10.1097/01.blo.0000186559.62942.8c>
- D'lima, D.D., Townsend, C.P., Arms, S.W., Morris, B.A., Colwell, C.W., 2005b. An

- implantable telemetry device to measure intra-articular tibial forces. *J. Biomech.* 38, 299–304. <https://doi.org/10.1016/j.jbiomech.2004.02.011>
- Dalury, D.F., Pomeroy, D.L., Gorab, R.S., Adams, M.J., 2013. Why are Total Knee Arthroplasties Being Revised? *J. Arthroplasty* 28, 120–121. <https://doi.org/10.1016/J.ARTH.2013.04.051>
- Dennis, D.A., Berry, D.J., Engh, G., Fehring, T., MacDonald, S.J., Rosenberg, A.G., Scuderi, G., 2018. Revision total knee arthroplasty. *Orthop. Knowl. Updat. Hip Knee Reconstr.* 5 267–278.
- Doherty, M., 2001. Risk factors for progression of knee osteoarthritis. *Lancet* 358, 775–776. [https://doi.org/10.1016/S0140-6736\(01\)06006-8](https://doi.org/10.1016/S0140-6736(01)06006-8)
- Elmallah, R.K., Mistry, J.B., Cherian, J.J., Chughtai, M., Bhave, A., Roche, M.W., Mont, M.A., 2016. Can We Really “Feel” a Balanced Total Knee Arthroplasty? *J. Arthroplasty* 31, 102–105. <https://doi.org/10.1016/J.ARTH.2016.03.054>
- Fan, F.-R., Lin, L., Zhu, G., Wu, W., Zhang, R., Wang, Z.L., 2012. Transparent Triboelectric Nanogenerators and Self-Powered Pressure Sensors Based on Micropatterned Plastic Films. *Nano Lett* 12, 3114. <https://doi.org/10.1021/nl300988z>
- Fan, F.-R.R., Lin, L., Zhu, G., Wu, W., Zhang, R., Wang, Z.L., 2012. Transparent triboelectric nanogenerators and self-powered pressure sensors based on micropatterned plastic films. *Nano Lett.* 12, 3109–3114. <https://doi.org/10.1021/nl300988z>
- Foran, J.R.H., Mont, M.A., Etienne, G., Jones, L.C., Hungerford, D.S., 2004. The outcome of total knee arthroplasty in obese patients. *J. Bone Joint Surg. Am.* 86, 1609–15. <https://doi.org/10.2106/00004623-200408000-00002>
- Gaizo, D.J. Del, Craig, ;, Della Valle, J., Della Valle, C.J., 2011. Instability in Primary

- Total Knee Arthroplasty 34. <https://doi.org/10.3928/01477447-20110714-46>
- Gillespie, G.N., Porteous, A.J., 2007. Obesity and knee arthroplasty. *Knee* 14, 81–86. <https://doi.org/10.1016/J.KNEE.2006.11.004>
- Gustke, Kenneth A, Golladay, G.J., Roche, M.W., Elson, L.C., Anderson, C.R., 2014. Primary TKA patients with quantifiably balanced soft-tissue achieve significant clinical gains sooner than unbalanced patients. *Adv. Orthop.* 2014, 628695. <https://doi.org/10.1155/2014/628695>
- Gustke, Kenneth A., Golladay, G.J., Roche, M.W., Elson, L.C., Anderson, C.R., 2014. A new method for defining balance: Promising Short-Term Clinical Outcomes of Sensor-Guided TKA. *J. Arthroplasty* 29, 955–960. <https://doi.org/10.1016/j.arth.2013.10.020>
- Hamill, J., Knutzen, K.M., 2014. *Biomechanical Basis of Human Movement*, Fourth. ed. Lippincott Williams & Wilkins, Baltimore, MD, USA.
- Hamilton, D.F., Howie, C.R., Burnett, R., Simpson, A.H.R.W., Patton, J.T., Hamilton, □ D F, 2015. Dealing with the predicted increase in demand for revision total knee arthroplasty CHALLENGES, RISKS AND OPPORTUNITIES. <https://doi.org/10.1302/0301-620X.97B6>
- Harms, S., Larson, R., Sahmoun, A.E., Beal, J.R., 2007. Obesity increases the likelihood of total joint replacement surgery among younger adults. *Int. Orthop.* 31, 23–26. <https://doi.org/10.1007/s00264-006-0130-y>
- Ibrahim, A., Jain, M., Salman, E., Willing, R., Towfighian, S., 2019a. A smart knee implant using triboelectric energy harvesters. *Smart Mater. Struct.* 28, 025040. <https://doi.org/10.1088/1361-665X/aaf3f1>
- Ibrahim, A., Ramini, A., Towfighian, S., 2018. Experimental and theoretical investigation of an impact vibration harvester with triboelectric transduction. *J. Sound Vib.* 416,

111–124. <https://doi.org/10.1016/J.JSV.2017.11.036>

Ibrahim, A., Yamomo, G., Willing, R., Towfighian, S., 2019b. Analysis of a triboelectric energy harvester for total knee replacements under gait loading 47.

<https://doi.org/10.1117/12.2515351>

Jiang, Y., Jia, T., Wooley, P.H., Yang, S.Y., 2013. Current research in the pathogenesis of aseptic implant loosening associated with particulate wear debris. *Acta Orthop. Belg.* 79, 1–9.

KELLGREN, J.H., LAWRENCE, J.S., 1957. RADIOLOGICAL ASSESSMENT OF OSTEO-ARTHRISIS, *Ann. rheum. Dis.* BMJ Publishing Group.

<https://doi.org/10.1136/ard.16.4.494>

Kirking, B., Krevolin, J., Townsend, C., Colwell, C.W., D'Lima, D.D., 2006. A multiaxial force-sensing implantable tibial prosthesis. *J. Biomech.* 39, 1744–1751.

<https://doi.org/10.1016/J.JBIOMECH.2005.05.023>

Kurtz, S., Mowat, F., Ong, K., Chan, N., Lau, E., Halpern, M., 2005. Prevalence of primary and revision total hip and knee arthroplasty in the United States from 1990 through 2002. *J. Bone Joint Surg. Am.* 87, 1487–97.

<https://doi.org/10.2106/JBJS.D.02441>

Kurtz, S., Ong, K., Lau, E., Mowat, F., Halpern, M., 2007. Projections of primary and revision hip and knee arthroplasty in the United States from 2005 to 2030. *J. Bone Joint Surg. Am.* 89, 780–5. <https://doi.org/10.2106/JBJS.F.00222>

Kutzner, I., Hallan, G., Høl, P.J., Furnes, O., Gøthesen, Ø., Figved, W., Ellison, P., 2018. Early aseptic loosening of a mobile-bearing total knee replacement. *Acta Orthop.* 89, 77–83. <https://doi.org/10.1080/17453674.2017.1398012>

Lespasio, M.J., PiuZZi, N.S., Husni, M.E., Muschler, G.F., Guarino, A., Mont, M.A., 2017. Knee Osteoarthritis: A Primer. *Perm. J.* 21, 16–183.

<https://doi.org/10.7812/TPP/16-183>

- Lin, L., Xie, Y., Wang, S., Wu, W., Niu, S., Wen, X., Wang, Z.L., 2013. Triboelectric active sensor array for self-powered static and dynamic pressure detection and tactile imaging. *ACS Nano* 7, 8266–8274. <https://doi.org/10.1021/nn4037514>
- Luciano, V., Sardini, E., Serpelloni, M., Baronio, G., 2014. An energy harvesting converter to power sensorized total human knee prosthesis. *Meas. Sci. Technol.* 25, 025702. <https://doi.org/10.1088/0957-0233/25/2/025702>
- Manning, W.A., Ghosh, K.M., Blain, A., Longstaff, L., Rushton, S.P., Deehan, D.J., 2018. Internal femoral component rotation adversely influences load transfer in total knee arthroplasty: a cadaveric navigated study using the Verasense device. *Knee Surg. Sports Traumatol. Arthrosc.* 26, 1577–1585. <https://doi.org/10.1007/s00167-017-4640-5>
- Mason, J.B., Fehring, T.K., 2006. Removing well-fixed total knee arthroplasty implants, in: *Clinical Orthopaedics and Related Research*. pp. 76–82. <https://doi.org/10.1097/01.blo.0000214413.06464.ce>
- Medel, F.J., Kurtz, S.M., Hozack, W.J., Parvizi, J., Purtill, J.J., Sharkey, P.F., MacDonald, D., Kraay, M.J., Goldberg, V., Rimnac, C.M., 2009. Gamma inert sterilization: a solution to polyethylene oxidation? *J. Bone Joint Surg. Am.* 91, 839–49. <https://doi.org/10.2106/JBJS.H.00538>
- Meneghini, R.M., Ziemba-Davis, M.M., Lovro, L.R., Ireland, P.H., Damer, B.M., 2016. Can Intraoperative Sensors Determine the “Target” Ligament Balance? Early Outcomes in Total Knee Arthroplasty. *J. Arthroplasty* 31, 2181–2187. <https://doi.org/10.1016/J.ARTH.2016.03.046>
- Noble, P.C., Scuderi, G.R., Brekke, A.C., Sikorskii, A., Benjamin, J.B., Lonner, J.H., Chadha, P., Daylamani, D.A., Scott, W.N., Bourne, R.B., 2012. Development of a new Knee Society scoring system. *Clin. Orthop. Relat. Res.* 470, 20–32.

<https://doi.org/10.1007/s11999-011-2152-z>

- Parratte, B.S., Pagnano, M.W., 2008. Instability After Total Knee Arthroplasty 184–194.
- Petrie, J.R., Haidukewych, G.J., 2016. Instability in total knee arthroplasty. *Bone Joint J.* 98-B, 116–119. <https://doi.org/10.1302/0301-620X.98B1.36371>
- Platt, S.R., Farritor, S., Garvin, K., Haider, H., 2005. The use of piezoelectric ceramics for electric power generation within orthopedic implants. *IEEE/ASME Trans. Mechatronics* 10, 455–461. <https://doi.org/10.1109/TMECH.2005.852482>
- Risitano, S., Karamian, B., Indelli, P.F., 2017. Intraoperative load-sensing drives the level of constraint in primary total knee arthroplasty: Surgical technique and review of the literature. *J. Clin. Orthop. trauma* 8, 265–269. <https://doi.org/10.1016/j.jcot.2017.06.004>
- Rönn, K., Reischl, N., Gautier, E., Jacobi, M., 2011. Current surgical treatment of knee osteoarthritis. *Arthritis* 2011, 454873. <https://doi.org/10.1155/2011/454873>
- Rosenthal, L., 1997. Hip and knee prostheses: Evaluation of the natural history of periprosthetic bone changes. *Semin. Nucl. Med.* 27, 346–354. [https://doi.org/10.1016/S0001-2998\(97\)80007-4](https://doi.org/10.1016/S0001-2998(97)80007-4)
- Safaei, M., Meneghini, R.M., Anton, S.R., 2018. Energy Harvesting and Sensing with Embedded Piezoelectric Ceramics in Knee Implants. *IEEE/ASME Trans. Mechatronics* 23, 864–874. <https://doi.org/10.1109/TMECH.2018.2794182>
- Safaei, M., Meneghini, R.M., Anton, S.R., 2017. Parametric analysis of electromechanical and fatigue performance of total knee replacement bearing with embedded piezoelectric transducers. *Smart Mater. Struct.* 26. <https://doi.org/10.1088/1361-665X/aa814e>
- Saleh, K.J., Thongtrangan, I., Schwarz, E.M., 2004. Osteolysis: Medical and surgical

approaches. *Clin. Orthop. Relat. Res.* 138–147.
<https://doi.org/10.1097/01.blo.0000142288.66246.4d>

- Scuderi, G.R., Bourne, R.B., Noble, P.C., Benjamin, J.B., Lonner, J.H., Scott, W.N., 2012. The New Knee Society Knee Scoring System. *Clin. Orthop. Relat. Res.* 470, 3. <https://doi.org/10.1007/S11999-011-2135-0>
- Sharkey, P.F., Lichstein, P.M., Shen, C., Tokarski, A.T., Parvizi, J., 2014. Why Are Total Knee Arthroplasties Failing Today—Has Anything Changed After 10 Years? *J. Arthroplasty* 29, 1774–1778. <https://doi.org/10.1016/J.ARTH.2013.07.024>
- Shields, M., Carroll, M.D., Ogden, C.L., 2011. Adult obesity prevalence in Canada and the United States. *NCHS Data Brief* 1–8.
- Sikorski, J.M., 2008. Alignment in total knee replacement. *J. Bone Joint Surg. Br.* 90-B, 1121–1127. <https://doi.org/10.1302/0301-620X.90B9.20793>
- Sloan, M., Premkumar, A., Sheth, N.P., 2018. Projected volume of primary total joint arthroplasty in the u.s., 2014 to 2030. *J. Bone Jt. Surg. - Am. Vol.* 100, 1455–1460. <https://doi.org/10.2106/JBJS.17.01617>
- Sundfeldt, M., Carlsson, L. V., Johansson, C.B., Thomsen, P., Gretzer, C., 2006. Aseptic loosening, not only a question of wear: A review of different theories. *Acta Orthop.* 77, 177–197. <https://doi.org/10.1080/17453670610045902>
- Unitt, L., Sambatakakis, A., Johnstone, D., Briggs, T.W.R., 2008. Short-term outcome in total knee replacement after soft-tissue release and balancing. *J. Bone Joint Surg. Br.* 90-B, 159–165. <https://doi.org/10.1302/0301-620X.90B2.19327>
- Vasarhelyi, E.M., MacDonald, S.J., 2012. The influence of obesity on total joint arthroplasty. *J. Bone Jt. Surg. - Ser. B* 94 B, 100–102. <https://doi.org/10.1302/0301-620X.94B11.30619>

- Vazquez-Vela Johnson, G., Worland, R.L., Keenan, J., Norambuena, N., 2003. Patient demographics as a predictor of the ten-year survival rate in primary total knee replacement. *J. Bone Joint Surg. Br.* 85, 52–6. <https://doi.org/10.1302/0301-620x.85b1.12992>
- Vince, K.G., 2003. Why knees fail. *J. Arthroplasty* 18, 39–44. <https://doi.org/10.1054/ARTH.2003.50102>
- Vince, K.G., Abdeen, A., Sugimori, T., 2006. The Unstable Total Knee Arthroplasty: Causes and Cures. *J. Arthroplasty* 21, 44–49. <https://doi.org/10.1016/J.ARTH.2006.02.101>
- Wang, Z.L., 2014. Triboelectric nanogenerators as new energy technology and self-powered sensors – Principles, problems and perspectives. *Faraday Discuss.* 176, 447–458. <https://doi.org/10.1039/C4FD00159A>
- Wang, Z.L., 2013. Triboelectric nanogenerators as new energy technology for self-powered systems and as active mechanical and chemical sensors. *ACS Nano* 7, 9533–9557. <https://doi.org/10.1021/nn404614z>
- Weinstein, A.M., Rome, B.N., Reichmann, W.M., Collins, J.E., Burbine, S.A., Thornhill, T.S., Wright, J., Katz, J.N., Losina, E., 2013. Estimating the burden of total knee replacement in the United States. *J. Bone Jt. Surg. - Ser. A* 95, 385–392. <https://doi.org/10.2106/JBJS.L.00206>
- Whiteside, L.A., 2002. Soft tissue balancing: The knee. *J. Arthroplasty* 17, 23–27. <https://doi.org/10.1054/ARTH.2002.33264>
- Wilson, C.J., Theodoulou, A., Damarell, R.A., Krishnan, J., 2017. Knee instability as the primary cause of failure following Total Knee Arthroplasty (TKA): A systematic review on the patient, surgical and implant characteristics of revised TKA patients. *Knee* 24, 1271–1281. <https://doi.org/10.1016/j.knee.2017.08.060>

- Wluka, A.E., Lombard, C.B., Cicuttini, F.M., 2013. Tackling obesity in knee osteoarthritis. *Nat. Rev. Rheumatol.* 9, 225–235.
<https://doi.org/10.1038/nrrheum.2012.224>
- Yercan, H.S., Ait Si Selmi, T., Sugun, T.S., Neyret, P., 2005a. Tibiofemoral instability in primary total knee replacement: A review, Part 1: Basic principles and classification. *Knee* 12, 257–266. <https://doi.org/10.1016/J.KNEE.2005.01.004>
- Yercan, H.S., Ait Si Selmi, T., Sugun, T.S., Neyret, P., 2005b. Tibiofemoral instability in primary total knee replacement: A review: Part 2: Diagnosis, patient evaluation, and treatment. *Knee* 12, 336–340. <https://doi.org/10.1016/J.KNEE.2005.01.005>
- Zhang, H., Yang, Y., Su, Y., Chen, J., Adams, K., Lee, S., Hu, C., Wang, Z.L., 2014. Triboelectric nanogenerator for harvesting vibration energy in full space and as self-powered acceleration sensor. *Adv. Funct. Mater.* 24, 1401–1407.
<https://doi.org/10.1002/adfm.201302453>

Chapter 2

2 Tuning of a 3D Printed Energy Harvester Package Design

Overview: *In this chapter, the design of a compliant package prototype will be discussed. The triboelectric generators were designed to generate electricity based on the cyclic contact and separation of two components. These generators harness the electron exchange resulting from the triboelectric effect. The TEGs, in their role of measuring loads in TKRs, require a package that ensures gap closure which is proportional to the amount of load transferred. The package was designed to achieve an axial force-displacement relationship that is compatible with the maximum allowable compression of the triboelectric generators while minimizing shear displacements resulting from shear forces during gait, which can otherwise cause TEG damage.*

2.1 Introduction

Despite the satisfactory success rate of modern TKR systems, implant failure still poses a problem (Baker et al., 2013; Mannion et al., 2009; Scott et al., 2010; Toms et al., 2009). Complications can be mitigated intraoperatively by ensuring optimal implant alignment and soft tissue balancing. Intraoperative tools such as the Verasense (Orthosensor, Inc., Dania Beach, FL) have proved to be an effective tool in soft tissue balancing during surgery. Some instrumented implants have been used in small cohorts of patients for research, however, clinically available instrumented implants are non-existent. Instrumented implants have the potential for providing important feedback in determining causes of implant failure which is unique to individual TKR recipients (Almouahed et al., 2017).

D’Lima et al. were the first to report the *in vivo* loads in a knee implant. In their first design iteration, a modified tibial tray with load cells located at the four corners of the tibial plateau, a power coil, a microtransmitter with an antenna were used to measure and relay the total force, anteroposterior and mediolateral load distribution, and the center of

pressure in the joint (D'lima et al., 2005a). The next iteration was capable of accurately measuring all six force components (Kirking et al., 2006). Bergmann et al. used a similar modified tibial tray as Kirking et al. to measure *in vivo* loads that may serve as a more accurate alternative to previously established standardized loads for pre-clinical testing of TKR such as ISO 14243 (Bergmann et al., 2014).

The main challenge of developing an instrumented implant is reliably powering these devices for their entire lifetime. The limitation of inductive coupling is the use of an external coil that is wrapped around the patient's knee. The presence of an external coil can impede mobility and thus alter patient biomechanics. In response to the need for a reliable, compact method of powering instrumented implants, the application of energy harvesting mechanisms has been investigated. Piezoelectric transducers have been embedded in UHMWPE bearings and tibial trays (Almouahed et al., 2017; Platt et al., 2005; Safaei et al., 2017). Luciano et al. presented work that uses an electromagnetic generator (Luciano et al., 2014). The alternative energy harvesting mechanisms, for load sensing applications in orthopaedic implants, have not been investigated thoroughly yet.

The triboelectric generator (TEG) developed by Ibrahim et al. is a novel approach in measuring tibial forces and harvesting energy from activities of daily living (Ibrahim et al., 2019a). Ibrahim et al. developed an energy harvesting system that uses the phenomenon known as the triboelectric effect. The TEGs are composed of specially designed contact interfaces that slide with respect to one another. The contact and separation between these interfacing surfaces create an electric charge that can be turned into usable electricity.

The objective of this study is to design a compliant interpositional device that interlocks between the UHMWPE bearing and the tibial tray, which can house the TEG components and elastically deform under physiological loading to provide an ideal amount of TEG contact and separation. Furthermore, the package must resist shear forces that can lead to permanent damage of the TEGs.

2.2 Materials and Methods

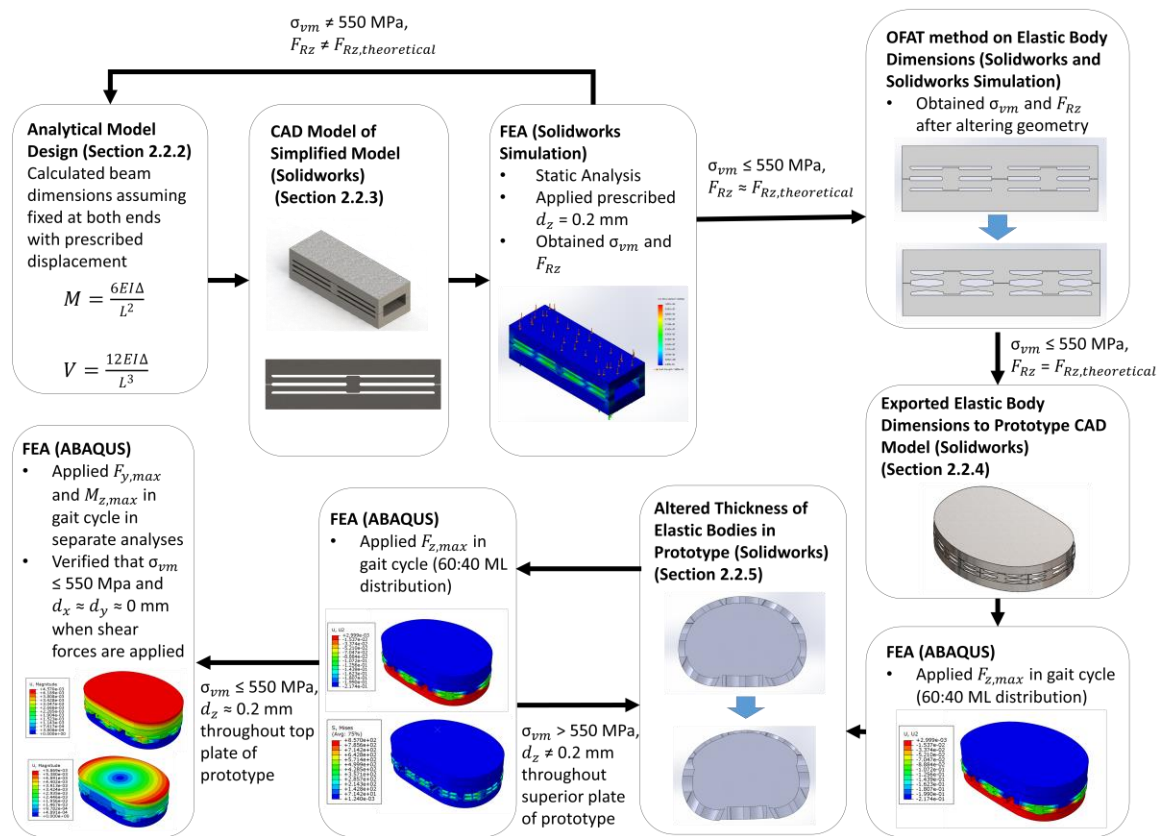


Figure 2-1-Design Process Flowchart

The overall design process is outlined in Figure 2-1. An analytical model was initially used to determine spring dimensions for the package design. Design iterations of the spring structures were performed with computer aided design (CAD) modelling and finite element analysis (FEA) on simplified models. The spring design that had the deflection and stress response was exported to a tibial tray shaped part. This part underwent subsequent design iterations to adjust the stiffness in different locations of the package design by altering the spring thickness.

2.2.1 Dimensions of Elastic Bodies

The geometry of a size 7 Triathlon tibial tray (Stryker, Kalamazoo, MI) was used for the prototype design. The geometries of the implant components were provided in the form

of polygonal surface models in the standard tessellation language (STL) file format. The inferior and superior geometry of the package was designed to interface with the existing locking mechanism between the PE bearing and tibial tray. The perimeter shape of the package was recreated based on that of the tibial tray and the PE insert. Based on the operating conditions of the TEGs, the package was designed to achieve a vertical displacement of 0.2 mm at the maximum vertical load of 2600 N as defined in ISO 14243 (ISO, 2009) while having a linear-elastic behavior across the entire force range. Elastic bodies were located along the periphery of the package to ensure an internal void to accommodate the 3 mm thick TEGs and the accompanying electronics.

2.2.2 Analytical Model Design

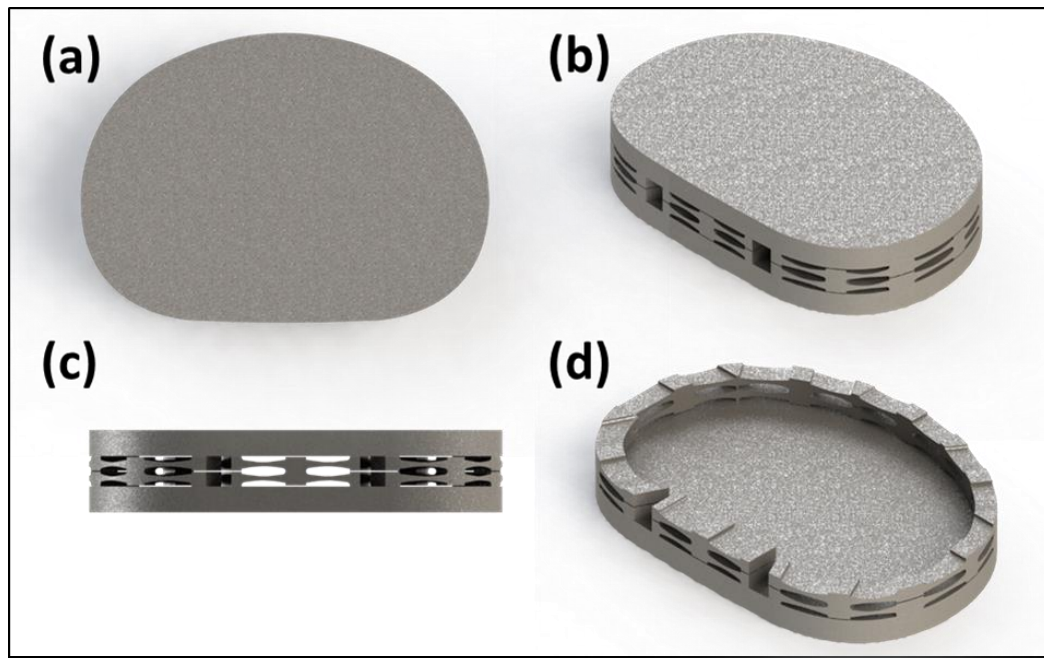


Figure 2-2- CAD model of the preliminary prototype concept design that feature elastic bodies along the periphery: (a) superior view, (b) isometric view, (c) posterior view, (d) section view that shows the internal void for TEG

For this prototype, a series of stacked beam structures were placed along the periphery. The design of the beam structures in the prototype can be calculated using the known

perimeter of the tibial tray and the length of the beams (Figure 2-2). The force per beam structure can be calculated based on the number of beams that can fit within the finite perimeter of the package. If the theoretical amount of load transmitted in each beam structure is known, the moment of inertia can be altered to yield a desired deflection within the elastic region.

A net deflection of 0.2 mm was desired at a force of 2600 N, approximately equaling the maximum vertical contact force during gait. Ti6Al4V was the material used for the design due to its biocompatibility and the availability of selective laser melting for future manufacturing.

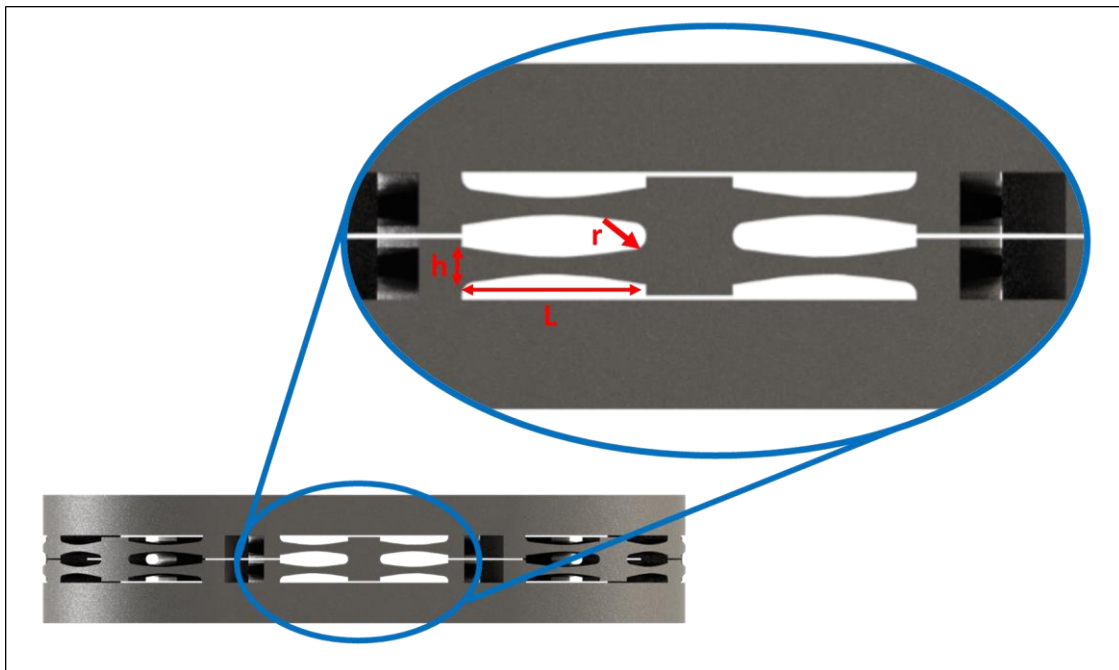


Figure 2-3- A magnified view of the beam structures located on the posterior of the package design. Length, height and fillet radius of the beams are denoted by L , h and r , respectively. *Note: The base (b) is orthogonal to h and L .*

A preliminary analytical solution was used to determine appropriate beam dimensions for the length (L), base (b), height (h), and fillet radii (r) (Figure 2-3). Equations 1 served as a starting point for calculating the moment of inertia (I) of a rectangular cross-sectional

area. Equations 1 calculate the height (h) in a beam fixed at both ends with a prescribed transverse displacement, Δ . Since two beams were stacked to decrease the strain of individual beams in the elastic bodies, a prescribed displacement of 0.1 mm was used in the calculations. Combinations of b , h , and L that resulted in calculated bending stresses and shear stresses less than the fatigue strength of Ti6Al4V (550 MPa) were considered in the design. Raw data and calculations of h are available in the Appendix.

$$h = \sqrt[3]{\left(\frac{2FL^3}{Eb\Delta}\right)} \quad \text{Equation 1}$$

2.2.3 Computational Model Design

Simplified models were constructed using CAD software (Solidworks, Dassault Systemes, Vélizy-Villacoublay, France). The simplified models consisted of two parallel, rectangular plates with elastic beam structures along two opposing sides (Figure 2-4). The stacked beam structures were modelled with the b , h , and L dimensions from the analytical solution.

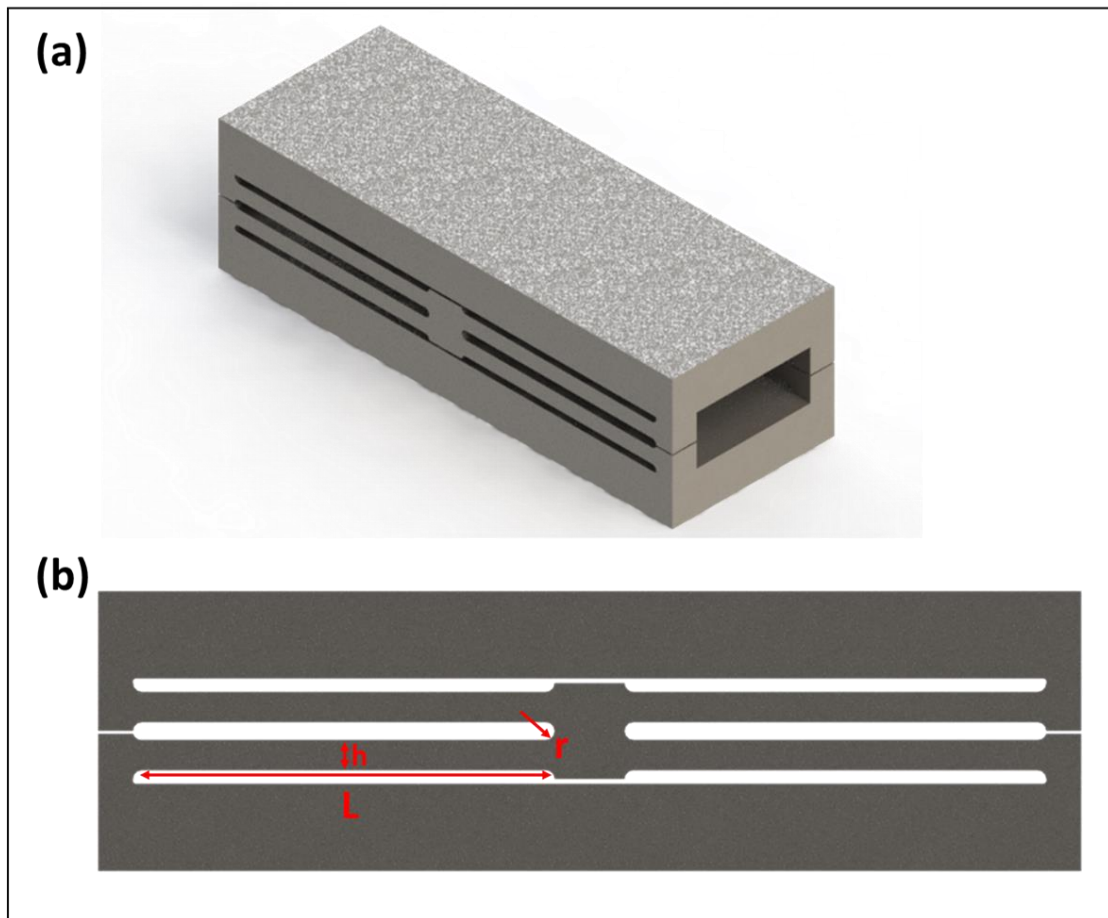


Figure 2-4- Simplified, rectangular model used for further computational model iterations on the beam design. (a) isometric view, (b) front view

FEA was conducted on the simplified models using Solidworks Simulation. A static study where one of the corners on the bottom plate was fully restrained, and the bottom surface had a roller/slider constraint was performed. A compressive force equal to the theoretical magnitude which, based on the analytical model, would lead to the model deflecting 0.2 mm was applied to the top surface of the model (Figure 2-5).

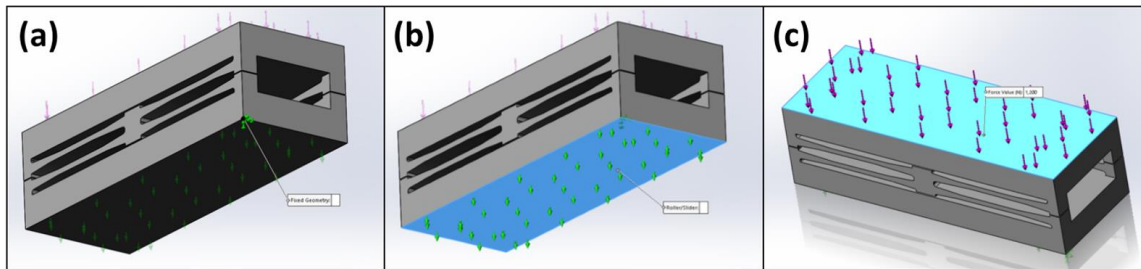


Figure 2-5- Boundary and Loading Conditions: (a) Fixed restraint on corner on bottom surface, (b) Roller/slider on bottom surface, (c) Force applied on top surface

Tetrahedral elements with a global mesh size of 1 mm were used for the analyses. An h-adaptive solution method was used for local mesh refinement in high stress regions in the model. H-adaptive meshing iteratively alters the mesh density in consecutive loops. In this study, the maximum number of 5 loops was used in the analysis. Convergence was achieved when the strain energy between subsequent loops yielded a 1% difference. The elastic modulus (E) was set to 128 GPa, yield strength (σ_y) equal to 1000 MPa (Renishaw plc, 2017) and the Poisson's ratio (ν) was defined as 0.31 (AZoMaterials, n.d.). Stacked beam structure dimensions (base (b), length (L), height (h), and fillet radii (r)) from the analytical model that yielded the target response values closest to the desired values ($\sigma_{vm} = 550 \pm 100$ MPa, $d = 0.2 \pm 0.05$ mm) were considered for further iterations.

The One-Factor-at-a-Time (OFAT) method was used to determine suitable dimensions for decreasing the midsection thickness of the beam using Bezier curves. The dimensions that were altered were a and h_{middle} (Figure 2-6). Reducing the thickness of the beam's midsection increased the compliance of the model. The dimensions that provided the desired deflection of 0.2 mm at the maximum load determined from the analytical model while having peak stresses below the fatigue strength of Ti6Al4V (550 MPa) were used in the final prototype design.

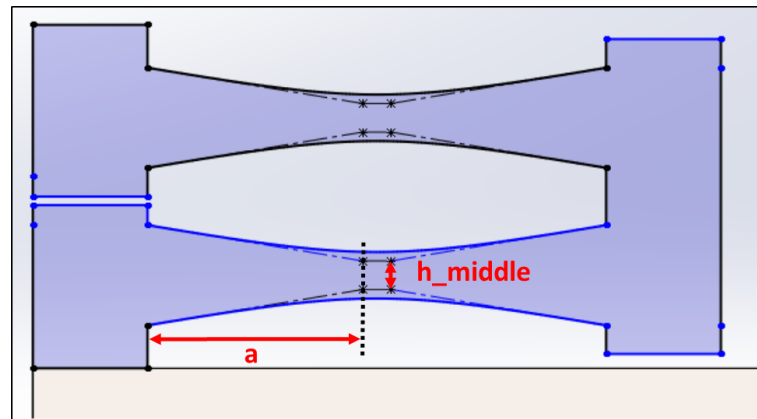


Figure 2-6- Bezier Curve Dimensions

2.2.4 Placement of Elastic Bodies in Package Prototype

Using the acquired STL file of a size 7 Triathlon tibial tray and the *Scanto3D* add-in in Solidworks, the surface mesh of the tibial tray's perimeter shape was used to create a 5 mm thick solid geometry of the prototype base. For this prototype, there would be anticipated prohibitively high stresses in the elastic bodies if they contoured the posterior notch of the tibial tray. Therefore, this prototype disregards the posterior notch and as a result, the prototype is limited to the use for TKRs that resect the cruciate ligaments (cruciate sacrificing designs). The geometry of the elastic bodies, determined by the OFAT method in the simplified models, were sketched along the periphery of the base and were extruded to an initial thickness of 3 mm. The base of the package was reproduced on the top of the elastic bodies to create a top plate (Figure 2-7).

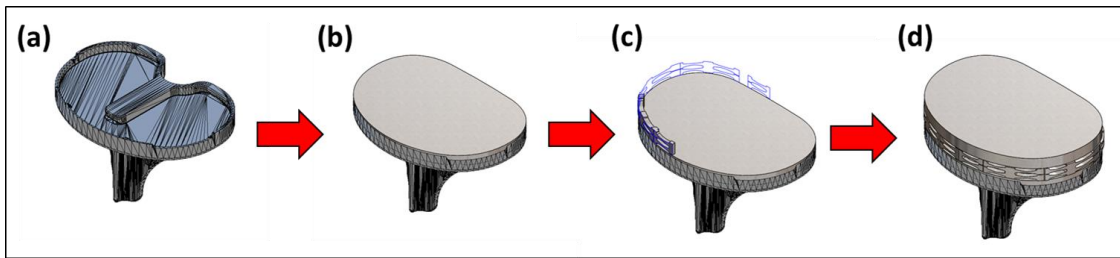


Figure 2-7- CAD Progression of Package Prototype: (a) STL file of tibial tray, (b) base of prototype, (c) extrusion of elastic bodies along periphery, (d) prototype with top plate

2.2.5 Spring Thickness Adjustment

In the following computational models used for the spring thickness adjustment, the model consisted of the package design from the previous section and a defeatured UHMWPE bearing. The UHMWPE bearing was modeled by sketching the perimeter shape of the tibial tray and extruding the resulting sketch by 6.25 mm—the thickness of a 9 mm thick UHMWPE bearing at its lowest point. The UHMWPE bearing model was mated to the superior surface of the top plate to create an assembly. This assembly was used in subsequent FEA. The CAD model of the package and UHMWPE bearing assembly was exported, as a .STEP file, to FEA software (Abaqus, Simulia, Johnston, RI) for further elastic body design iterations. A tie constraint was defined to connect the package prototype and the UHMWPE bearing instances. Two reference points were created: one was placed inferior of the assembly, and the other one was placed superior to the package offset from the sagittal plane in order to simulate a 60:40 medial load bias, and above the lowest points of the UHMWPE bearing (Figure 2-8). The inferior reference point was rigidly connected to the inferior surface of the package and fully restrained using an Encastre boundary condition. The superior reference point was rigidly connected to the superior surface of the UHMWPE bearing. Loads were applied to the superior reference point. The global mesh size for the package prototype was 0.7 mm, whereas the UHMWPE bearing had a global mesh size of 6.3 mm. Tetrahedral elements were used for

both components. The Ti6Al4V package had the following material properties: $E = 130\,000\text{ MPa}$, and $\nu = 0.31$. The UHMWPE bearing component was assigned $E = 830\text{ MPa}$, and $\nu = 0.42$.

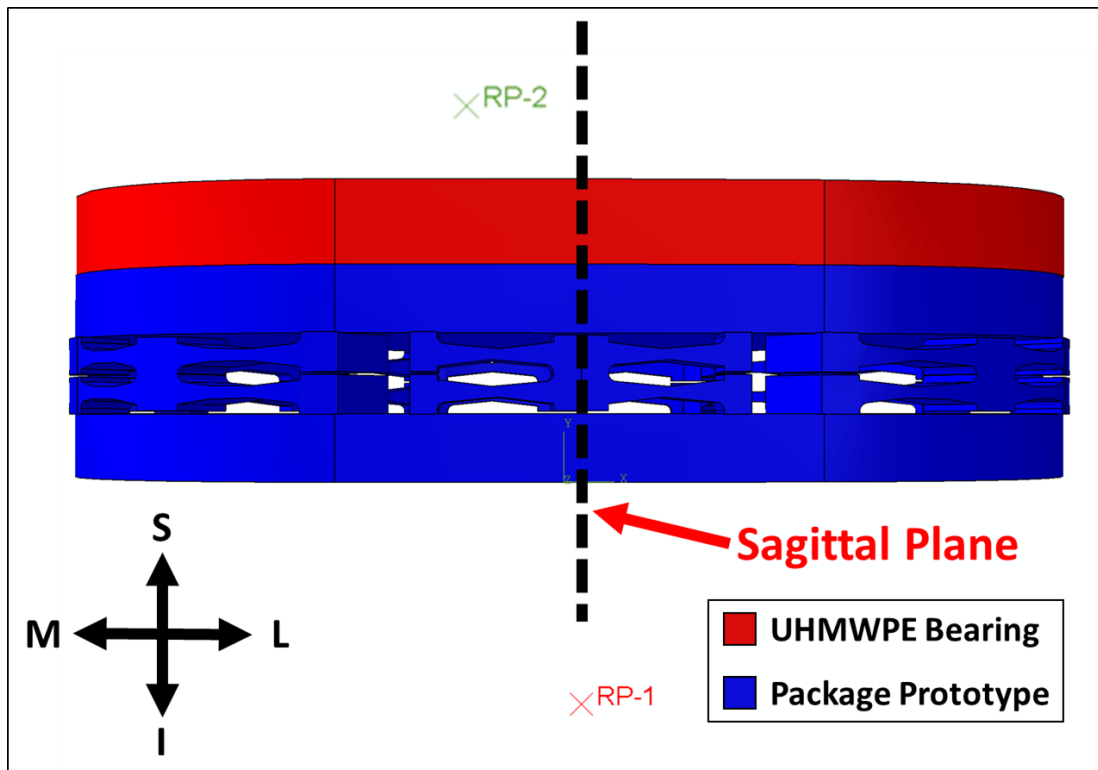


Figure 2-8-A posterior view of the package-PE bearing assembly. Reference point, RP-1, was placed inferior to the assembly. Reference point, RP-2, was placed superior to the assembly and offset medially to replicate a 60:40 (medial:lateral) load bias.

A vertical compressive load of 2600 N, the maximum load in gait based on ISO 14243, was applied to the superior reference point. At this point, the thickness of the elastic bodies had a thickness of 3 mm along the entire periphery of the package. Due to the asymmetric geometry along the anteroposterior axis and the load being applied in the posterior part of the package, the thicknesses of the elastic bodies were altered in regions along the package to ensure a uniform deflection of 0.2 mm was achieved. Deflections that exceed 0.2 mm could exceed the gap distance of the TEGs thus possibly resulting in

damage to the TEGs' contacting surfaces. To compound the effect of an uneven deflection behaviour, the improper vertical alignment of the sawtooth ridges of the TEG interfacing surfaces can also contribute to TEG damage. Another reason for having the package deflect uniformly along the anteroposterior axis is to maximize the contact between the TEG surfaces which in turn maximizes the energy harvested.

If the target deflection behaviour was not achieved, the thickness of the package was altered to adjust the localized stiffness in different regions in the package. After elastic body adjustments were performed in Solidworks, FEA was conducted using the same parameters in the compression simulation. The elastic body thickness underwent further iterations until a uniform deflection of 0.2 mm was achieved.

As eluded previously, the TEG contacting surfaces are susceptible to damage from shear displacements and operate solely from contact and separation in the vertical direction. Therefore, the package must be able to eliminate shear displacements. The package's resistance to shear forces in gait was analyzed by applying a posteriorly-directed load of 265 N and an internal torque of 6 Nm from ISO 14243 to the superior rigid point to calculate the shear displacements in separate simulations. Compression was not superimposed on the shear forces.

2.2.6 Reverse Engineering Interlocking Mechanism of TKR Components

In order to install the TEGs inside the package, the package was separated into a bottom and top part with an interlocking geometry to resist relative transverse motion. To secure the two parts together, three M3 x 0.5mm, 6 mm flat head screws were located in threads created in the medial, lateral, and posterior regions of the prototype.

On the superior surface of the top plate, the interlocking geometry of the tibial tray was created using manufactured-provided surface mesh data. On the inferior surface of the bottom plate, the interlocking geometry of a UHMWPE bearing was replicated using the

mesh data. Therefore, the package prototype was designed to fit in-between the tibial tray and UHMWPE bearing of a size 7 Stryker Triathlon system.

2.3 Results

2.3.1 Analytical Model Design

Based on the analytical model of a single beam, the σ_b (bending stress) decreased as the length and base of the beams increased. Contrarily, the calculated height, which would result in the desired deflection of 0.1 mm, exhibited a proportional relationship with σ_b (Figure 2-9 and Figure 2-10).

Due to the volumetric constraints of the package where the overall thickness should be minimized and the internal volume should be maximized, some dimensions for L , b and h were not considered. The gap distance between the top and bottom plates of the package was limited to a maximum of 6 mm. Enough vertical space should be reserved for the deflection of the beams. Also, having a small gap between beams would lead to sharp reentrant edges that can serve as stress concentrations. In this design, enough space was desired to relieve stress concentrations with fillets at the corners. In regards to the internal volume, encroachment of the elastic bodies towards the interior of the package was minimized by minimizing b of the beams.

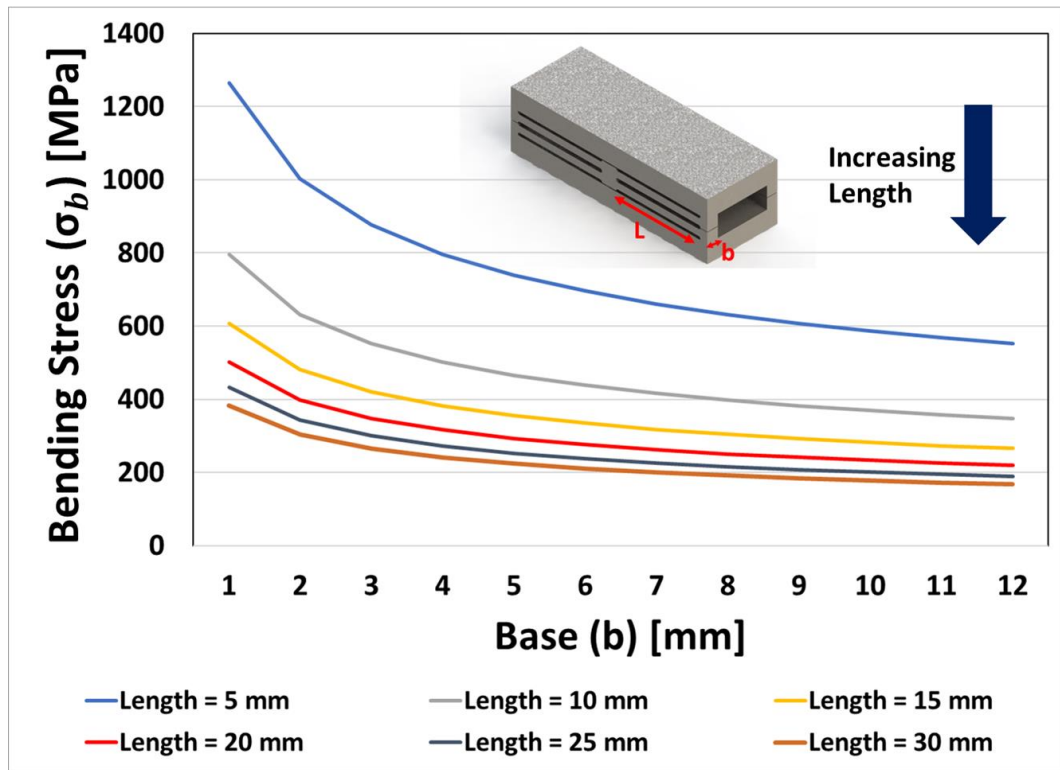


Figure 2-9- Effects of length and base parameters on the bending stress.

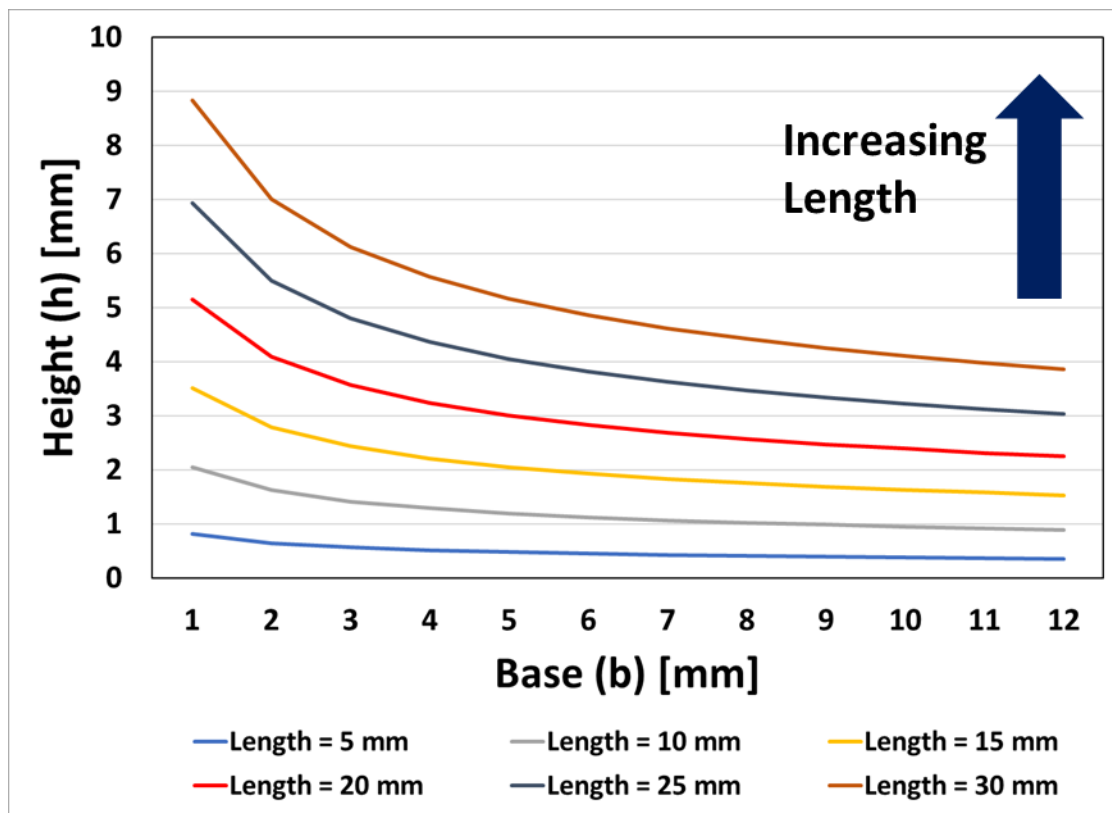


Figure 2-10- Effect of length and base on the height

2.3.2 Computational Model Design

2.3.2.1 Simplified Design Simulations

The computational models that simulate compression of the simplified designs did not demonstrate a close agreement with the analytical model. The computational models had larger stresses and deflections that were calculated in the analytical model, as summarized in Table 2-1. A variable that was overlooked in the analytical model was the influence the fillet radii had on the stresses and deflections. When comparing test runs 3 and 4 in Table 2-1, there was approximately a 600 MPa decrease in $\sigma_{vm,max}$ and a 0.04 mm decrease in the vertical displacement when the fillet radius was increased by 0.25 mm. The peak stresses were located at the base of the beams in the computational

model (Figure 2-11). The exclusion of considering the effects of including the fillets in the analytical led to an underestimation of the expected stresses and deflections.

Table 2-1-Stress and deflection comparison between computational and analytical model. The computational models presented in this table had dimensions similar to what was used in the analytical model.

Test Run	<i>Beam Dimensions</i>			<i>Computational Responses</i>		<i>Analytical</i>
	h [mm]	L [mm]	r [mm]	σ_{vm} [MPa]	d_v [mm]	σ_b [MPa]
1	1	8	0.25	1774	0.49	640
2	1.5	10	0.25	1330	0.39	552
3	1.5	12	0.25	1896	0.69	489
4	1.5	12	0.5	1300	0.65	489

Note: $b = 3$ mm, $d_{y,analytical} = 0.2$ mm

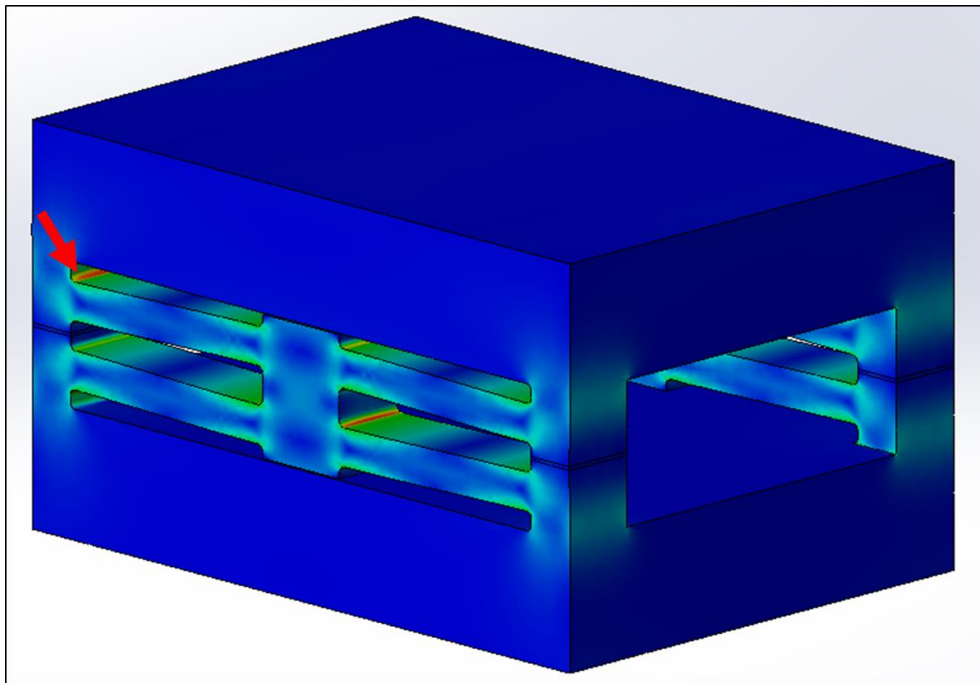


Figure 2-11- An isometric view of the FE model for Test Run 2 (Table 2-1). Peak stress locations were located at the base of the beams (denoted by red arrow).

Combinations of dimensions were not limited to what was determined from the analytical model especially in light of the discrepancies that it had with the aforementioned computational models presented in Table 2-2. The shorter length beams, despite having lower stresses, were too stiff. The opposite was observed for longer beams. The stiffness was proportional to the height. The peak stresses and deflections occurred with the longer slender beams (i.e. Test Run 3 in Table 2-2). For the prototype design, Test 16 was used for further iterations in acquiring the desired mechanical response. These dimensions had

response values close to the target values; the stiffness and the stress could be reduced by reducing the thickness of the beam's midsection.

Table 2-2- Stress and deflections resulting from dimensions altered using the One-Factor-at-a-Time method.

Test Run	Beam Dimensions			Responses	
	h [mm]	L [mm]	r [mm]	σ_{vm} [MPa]	d_y [mm]
1	1	6	0.25	1113	0.19
2	1	8	0.25	1774	0.49
3	1	10	0.25	2200	1.00
4	1.5	6	0.25	632	0.08
5	1.5	8	0.25	984	0.19
6	1.5	10	0.25	1330	0.39
7	1.5	12	0.25	1896	0.69
8	2	6	0.25	400	0.04
9	2	8	0.25	608	0.10
10	2	10	0.25	815	0.20
11	2	12	0.25	594	0.17
12	1	6	0.5	839	0.17
13	1	8	0.5	1358	0.45
14	1	10	0.5	1999	0.97
15	1.5	6	0.5	389	0.07
16	1.5	8	0.5	632	0.17
17	1.5	10	0.5	1919	0.35
18	1.5	12	0.5	1300	0.65

Note: b = 3 mm

2.3.2.2 Tuning of Midsection Thickness

After selecting the dimensions from Test Run 16 in Table 2-2, Bezier curves were used to create a tapered midsection in the beams. Thinning the midsection increased the compliance and reduced the stresses when compared to a beam with a uniform cross-section. After several changes to the altered parameters, the dimensions from Test Run 8, in Table 2-3, were exported to the tibial tray shaped prototype since it had a peak von Mises stress less than 550 MPa and the resultant force from a prescribed vertical

displacement of 0.2 mm that was close to the theoretical target compressive load. The progressive beam dimension changes are outlined below in Table 2-3.

Table 2-3- Summary of stresses and resultant vertical force after altering beam midsection thickness using Bezier curves.

Test Run	Beam Dimensions					Responses	
	h [mm]	L [mm]	r [mm]	a [mm]	$h_{midsection}$ [mm]	σ_{vm} [MPa]	F_{Rz} [N]
1	1.5	8.5	0.5	2	1	560	816
2	1.5	8.5	0.5	3	1	598	854
3	1.5	8.5	0.5	3.5	1	611.3	872
3	1.75	8.5	0.5	3.5	1	719.2	1129
4	1.75	8.5	0.5	3	1	702.8	1100
5	1.75	8.5	0.5	3.5	1	712.8	1129
6	1.75	8.5	0.5	3.5	0.75	637	983
7	1.75	8.5	0.6	3.5	0.5	513	830
8	1.75	8.5	0.6	3.75	0.5	527.5	855

Note: b = 3 mm; Prescribed displacement was applied instead of compressive force

2.3.3 Simulation Results of Prototype Design

From the vertical load simulation, stresses were generally below the 550 MPa threshold. The highest stresses were located at the base of the beams, where bending moments would dominate, in the medial and lateral regions of the package. The high stresses exceeded the fatigue strength of Ti6Al4V in a small region (about 5.7% of the beam's volume) (Figure 2-12). The peak stress was 857 MPa located in the anteromedial portion of the package. The deflection of the top plate with respect to the bottom plate was 0.22 mm, slightly greater than the target of 0.2 mm (Figure 2-13).

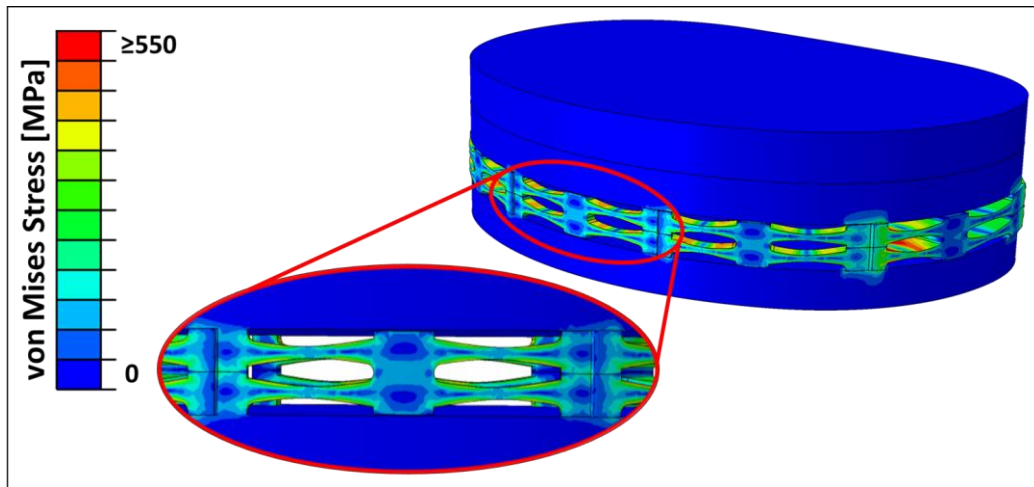


Figure 2-12- Stress Plot from Maximum Axial Load

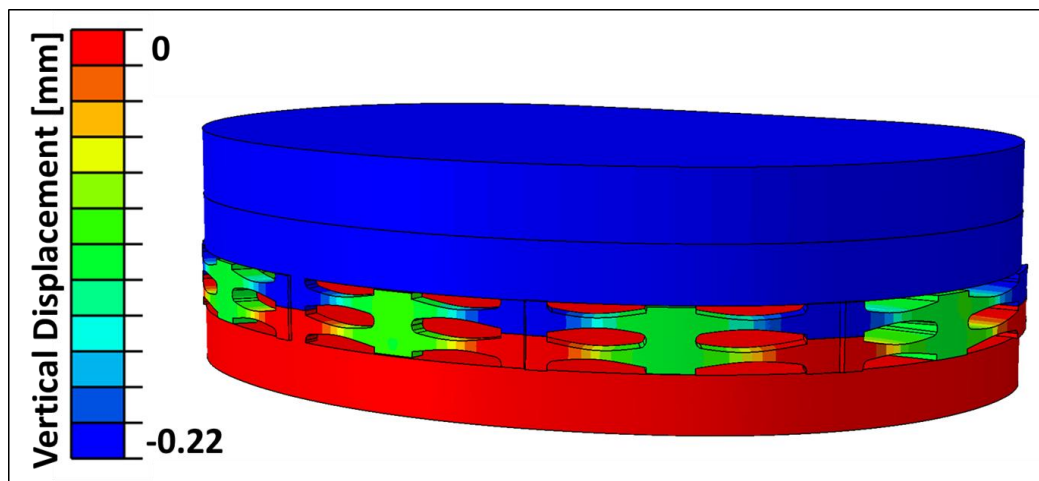


Figure 2-13- Vertical Displacement Plot from Maximum Axial Load

From the posteriorly directed load of 265 N, the shear displacements of the top plate with respect to the bottom plate and the stresses were negligible. Similar stresses and displacements were calculated when an internal torque of 6 Nm was applied to the computational model. The maximum stresses and displacements from the ISO 14243 loads are outlined in Table 2-4. In Figure 2-14, the maximum shear displacements from the shear loads are shown.

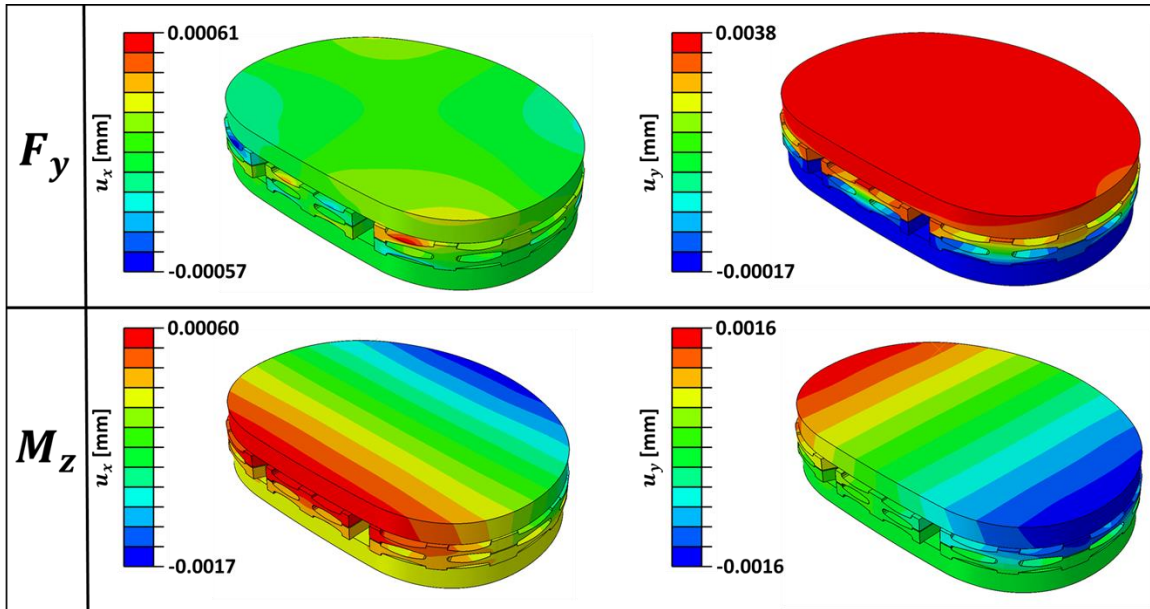


Figure 2-14- Shear displacements due to maximum posteriorly directed force (F_y) and internal moment (M_z) in ISO 14243

Table 2-4- Maximum Stress and Displacements from Maximum Loads in ISO 14243

Applied Load	σ_{vm} [MPa]	u_x [mm]	u_y [mm]	u_z [mm]
$F_z = 2600$ N	550	0.01	0.013	0.22
$F_y = -265$ N	52.6	0.00061	0.0038	0.0039
$M_z = 6$ Nm	46.4	0.0017	0.0016	0.0017

2.3.4 Dimensions of Elastic Bodies

The dimensions of the stacked beam structures for the compliant package are outlined in (Figure 2-15). The thickness of the elastic bodies was altered because of the larger load distribution in the posterior of the package. Therefore, beam thickness gradually increased from the anterior to the posterior. This gradual change in the thickness is illustrated in Figure 2-16.

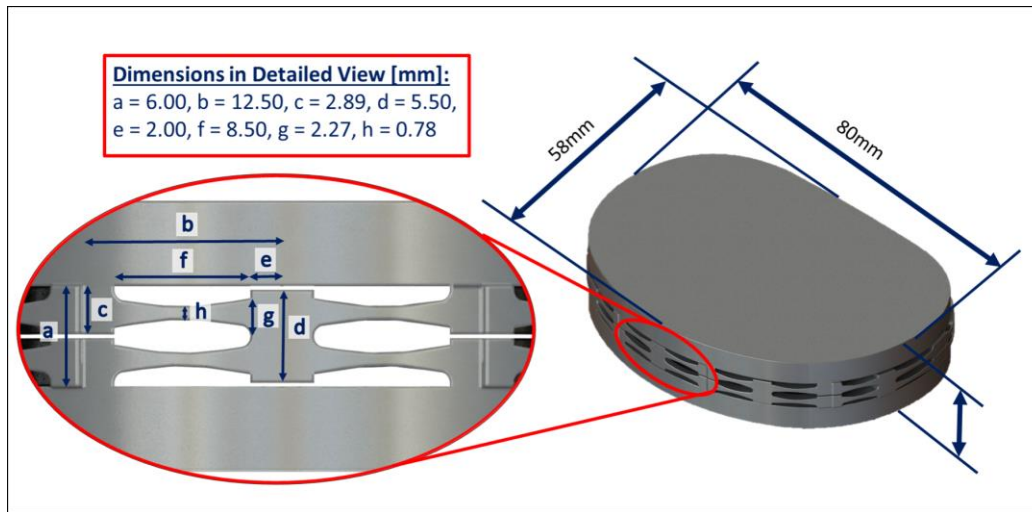


Figure 2-15-Dimensions of stacked beam structure

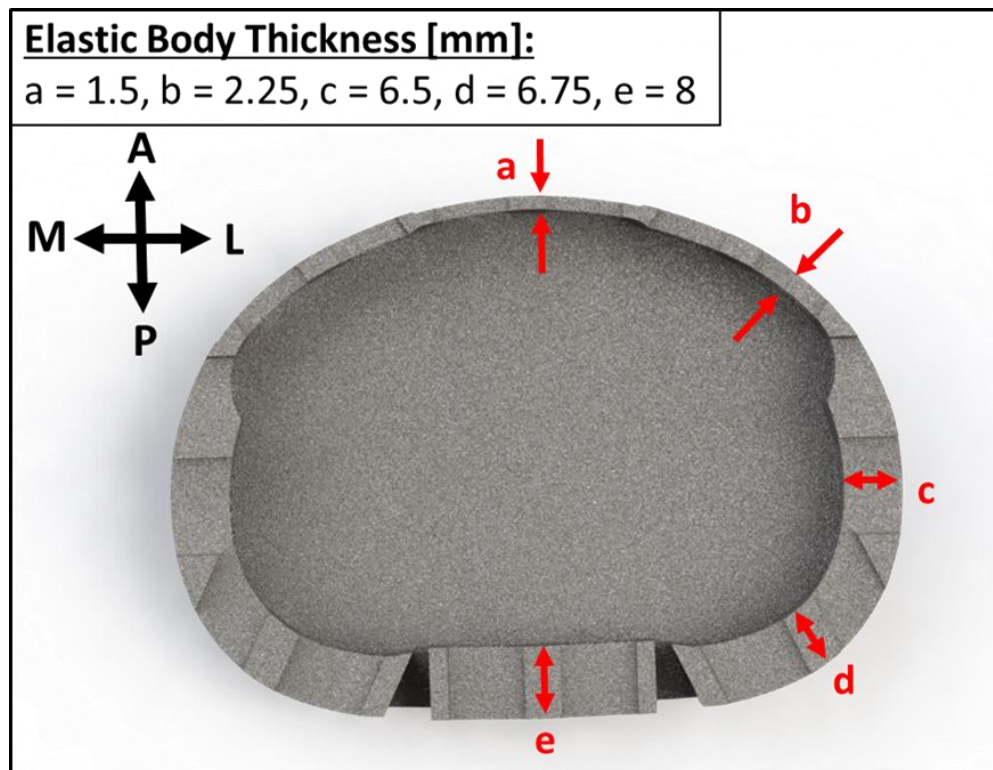


Figure 2-16- Cross-sectional view of the elastic bodies. The prototype was symmetrical along the sagittal plane, therefore dimensions were denoted only on one side.

2.4 Discussion

In this current study, a compliant, linearly elastic package was designed for housing the TEGs developed by Ibrahim et al (Ibrahim et al., 2019a). Springs were positioned along the periphery of a tibial tray shaped package to achieve a maximum deflection of 0.2 mm (gap distance between the TEG layers) under the maximum vertical load according to ISO 14243. The package had peak stresses that surpassed the fatigue strength of Ti6Al4V but were lower than the yield strength.

The beam dimensions, initially determined using an analytical model, were used for creating rectangular, simplified designs that underwent simulated compression. The computational models calculated the peak stress and stiffness of the elastic body design iterations. Modifications were made to the dimensions of the springs until the target stress and deflection were achieved. The springs that had the desired mechanical response from the computational models of the simplified designs were exported along the periphery of a tibial tray shaped package. Further tuning was done to this model by varying the thickness of the beams until a uniform vertical displacement was calculated. After applying the shear forces occurring during gait, the package was verified to have a negligible amount of shear displacement.

The reason behind using a large TKR was to maximize the surface area of the TEGs. The TEG's energy harvesting capability is partly limited to the surface area. An increase of the surface area would increase the area for contact and separation between the interfacing surfaces thus increasing the power generated. Another benefit to deriving a design from a larger tibial tray is that the volume available for a compliant geometry within the package would be maximized. The technique used in this chapter can be implemented in all other implant sizes and different designs.

The dimensions of the current design may not be the optimal dimensions that would result in the desired stress and deflections. There may be other combinations not considered that may be more suitable. Localized changes to all the dimensions may be

better suited in different areas of the package as opposed to altering the base (b) of the beams where force distributions differ. The rationale behind changing only the base of the beams was the efficiency to update the model and undergo further design iterations.

Higher stresses were calculated in the tibial tray shaped prototype when compared to the simplified model. This is a limitation of projecting an idealized beam structure onto a curved profile. After projecting the sketch and extruding the beams towards the interior of the package, the beams do not maintain the length that was tested in the simplified models. This led to increased stress magnitudes in sections of the beams adjacent to the internal void. The primary objective was to create a prototype with the desired stiffness. By limiting the elastic bodies along the periphery, the beams did not maintain the geometry that was used in the simplified models thus resulting in stresses and stiffness that differ from the simplified models.

High stresses resulting from the projection of the beam structure to the package periphery explains the absence of the posterior notch. The idealized beam structure was not replicated along the posterior notch. The shorter beams of the projected beam structure increased the stresses. With the means of reducing the stress and maximizing the internal surface area for the TEGs, the notch was disregarded in this initial prototype. Although some TKR designs require the resection of the cruciate ligaments, cruciate retaining (CR) designs will require the PCL. Future design iterations will require the need to include the posterior notch while possessing the mechanical properties to allow the TEGs to operate optimally.

The height (h) would have a more profound effect on the stresses in the package because of its cubic relationship with the moment of inertia (I). In addition, b could be reduced as h increases thus further maximizing the internal volume. The localized tuning of h can optimize the stiffness and reduce the stress. However, altering the projected elastic body sketch along the tibial tray shaped periphery proved to be difficult. Varying even just a single beam parameter would require changes to the sketch originating from the simplified design. Performing this for all elastic body units of the package design would

be time consuming and arduous. For future consideration, the use of a tibial tray shaped prototype with elastic bodies with parameters that can be readily changed can facilitate localized tuning.

Longer beams in the analytical model resulted in lower calculated stresses while achieving the desired stiffness. The main limitation behind designing beams that are longer than what was used is that the required beam height h was limited by the height of the internal void. In other words, the longer beams could not be accommodated in a void with a 6 mm vertical height.

There are inherent limitations associated with using OFAT in designing the compliant package. OFAT can be an inefficient method in design optimization. It can require more time, experiments and resources (Telford, 2007). The estimates of each factor that explains the response aren't always precise. The main effects can be determined from OFAT, but the effects of interactions between input variables cannot be quantified. For instance, using OFAT, the effect of simultaneously changing the L and b on the deflection cannot be estimated. Since OFAT consists largely on "trial and error", the entire factor space is not considered thus increasing the possibility of false optimal conditions (Antony et al., 2003). Design of experiments (DOE) is a more efficient method of quantifying the sensitivity of the input variables and it provides a mathematical model that accounts for the estimation of main effects and interactions (Antony et al., 2003; Czitrom, 1999; Telford, 2007; Wahid and Nadir, 2013).

The peak stresses in the package design were below the yield strength of Ti6Al4V, but higher than the fatigue strength. For this prototype, a package with a linearly elastic behaviour was prioritized over the fatigue behaviour. The multi-objective nature of this application can prove to be difficult to satisfy all the desired engineering constraints, but this package had a stiffness that has the potential to work with the TEGs, maximized the space for the TEGs, and the package remained in the elastic region under 2600 N of compression.

Another limitation to this study is that other motions like jogging were not tested. Ideally, the package should be designed to withstand physiological loading with the largest magnitudes. For the case of preliminary evaluation, gait loading from ISO 14243 was assumed to be acceptable.

The modular design of the package provides surgeons intraoperative choices regarding component thickness and implant constraint. Another advantage of using modular components is that a worn PE bearing can be replaced without affecting the bony fixation of the tibial component during a revision procedure (Barrack, 1994). However, the modularity of implant components can be problematic. Wear and tribocorrosion can occur between interfacing surfaces thus resulting in wear induced synovitis, osteolysis or adverse local soft tissue reactions (ALTRs) (Berry et al., 2014; Jacobs et al., 2009). The PE bearing-package and package-tibial tray interfaces can elicit an increase in wear particles.

The micromotion between the underside of the PE bearing and the top plate of the package can lead to larger amounts of polyethylene wear and debris particles (Li et al., 2002; Sisko et al., 2017; Wasielewski et al., 1997). Two factors that greatly affect this PE backside wear are the surface finish of the tibial tray and the interlocking mechanism (Rao et al., 2002; Sisko et al., 2017). The use of TKR systems with highly polished tibial tray surfaces can reduce backside damage and linear wear (Berry et al., 2012; Teeter et al., 2015). A robust interlocking mechanism that restricts tibial tray motion also contributes to PE bearing longevity (Conditt et al., 2004; Jayabalan et al., 2007). The current prototype's design is derived from the Stryker Triathlon TKR system. The Triathlon interlocking mechanism, which features a central anti-rotational island to the peripheral capture, limits PE backside motion (Sisko et al., 2017). Despite the Triathlon interlocking mechanism's effectiveness in reducing PE backside wear, future iterations of this package design can limit PE damage by polishing the package surfaces.

The package-tibial tray interface may be more concerning than the PE bearing-package interface. This metal-on-metal interface can introduce metal ions which can lead to

synovitis and local soft tissue reactions (Berry et al., 2014; Jacobs et al., 2009). The wear and tribocorrosion at this interface can be exacerbated by the rough surfaces of both components. Future designs should ensure minimal relative micromotion between these surfaces. A high tolerance press-fit of the package and the tibial tray may be a viable option in reducing the micromotion. Otherwise, a custom tibial component with the integrated package may be required to eliminate the metal-on-metal surface interaction. Overall, when considering a package design that is compatible with other TKR systems, surface finish and the interlocking mechanism are still of a concern in terms of mitigating implant failure.

Future research can be done to optimize the design of the elastic bodies. DOE and topological optimization may provide other geometric alternatives that will provide the desired stiffness and reduce the peak stresses. This current study only considered the loads in ISO 14243. In future iterations, the stiffness and stresses should be tuned with consideration of other ADL such as jogging, stair ascent and stair descent where higher magnitude loads can be transmitted through the package.

2.5 Conclusion

In this chapter, the process of designing a compliant package intended for the integration of TEGS was outlined. The deflection of the package was slightly larger than the target of 0.2 mm at a compressive load of 2600 N. The package, based on the computational models, was able to resist shear forces that can lead to permanent damage of the TEGs. The calculated peak stresses exceeded the fatigue strength but remained within the elastic region of Ti6Al4V. This suggests that failure is possible due to fatigue. The following chapters will examine a 3D printed prototype where the stiffness of the prototype will be compared with the computational results and the fatigue life of the package will be quantified.

2.6 References

- Almouahed, S., Hamitouche, C., Stindel, E., 2017. Optimized Prototype of Instrumented Knee Implant: Experimental Validation. *IRBM* 38, 250–255.
<https://doi.org/10.1016/J.IRBM.2017.06.005>
- Antony, J., Chou, T., Ghosh, S., 2003. Training for design of experiments. *Work Study* 52, 341–346. <https://doi.org/10.1108/00438020310502642>
- AZoMaterials, n.d. Properties: Titanium Alloys - Ti6Al4V Grade 5 [WWW Document]. URL <https://www.azom.com/properties.aspx?ArticleID=1547> (accessed 11.4.19).
- Baker, P.N., Rushton, S., Jameson, S.S., Reed, M., Gregg, P., Deehan, D.J., 2013. Patient satisfaction with total knee replacement cannot be predicted from pre-operative variables alone: A cohort study from the national joint registry for england and wales. *Bone Jt. J.* 95 B, 1359–1365. <https://doi.org/10.1302/0301-620X.95B10.32281>
- Barrack, R.L., 1994. Modularity of Prosthetic Implants, *Journal of the American Academy of Orthopaedic Surgeons*.
- Bergmann, G., Bender, A., Graichen, F., Dymke, J., Rohlmann, A., Trepczynski, A., Heller, M.O., Kutzner, I., 2014. Standardized Loads Acting in Knee Implants. *PLoS One* 9, 86035. <https://doi.org/10.1371/journal.pone.0086035>
- Berry, D.J., Abdel, M.P., Callaghan, J.J., 2014. What Are the Current Clinical Issues in Wear and Tribocorrosion? *Clin. Orthop. Relat. Res.* 472, 3659–3664.
<https://doi.org/10.1007/s11999-014-3610-1>
- Berry, D.J., Currier, J.H., Mayor, M.B., Collier, J.P., 2012. Knee wear measured in retrievals: A polished tray reduces insert wear, in: *Clinical Orthopaedics and Related Research*. Springer New York LLC, pp. 1860–1868. <https://doi.org/10.1007/s11999-012-2248-0>

- Conditt, M.A., Stein, J.A., Noble, P.C., 2004. Factors affecting the severity of backside wear of modular tibial inserts. *J. Bone Joint Surg. Am.* 86, 305–11.
<https://doi.org/10.2106/00004623-200402000-00013>
- Czitrom, V., 1999. One-factor-at-a-time versus designed experiments. *Am. Stat.* 53, 126–131. <https://doi.org/10.1080/00031305.1999.10474445>
- D’lima, D.D., Patil, S., Steklov, N., Slamin, J.E., Colwell, C.W., 2005. THE CHITRANJAN RANAWAT AWARD In Vivo Knee Forces after Total Knee Arthroplasty. <https://doi.org/10.1097/01.blo.0000186559.62942.8c>
- Ibrahim, A., Jain, M., Salman, E., Willing, R., Towfighian, S., 2019. A smart knee implant using triboelectric energy harvesters. *Smart Mater. Struct.* 28, 025040.
<https://doi.org/10.1088/1361-665X/aaf3f1>
- ISO, 2009. ISO 14243-1, Implants for surgery - Wear of total knee-joint prostheses.
- Jacobs, J.J., Urban, R.M., Hallab, N.J., Skipor, A.K., Fischer, A., Wimmer, M.A., 2009. Metal-on-metal bearing surfaces. *J. Am. Acad. Orthop. Surg.* 17, 69–76.
<https://doi.org/10.5435/00124635-200902000-00003>
- Jayabalan, P., Furman, B.D., Cottrell, J.M., Wright, T.M., 2007. Backside wear in modern total knee designs. *HSS J.* 3, 30–34. <https://doi.org/10.1007/s11420-006-9033-0>
- Kirking, B., Krevolin, J., Townsend, C., Colwell, C.W., D’Lima, D.D., 2006. A multiaxial force-sensing implantable tibial prosthesis. *J. Biomech.* 39, 1744–1751.
<https://doi.org/10.1016/J.JBIOMECH.2005.05.023>
- Li, S., Scuderi, G., Furman, B.D., Bhattacharyya, S., Schmieg, J.J., Insall, J.N., 2002. Assessment of backside wear from the analysis of 55 retrieved tibial inserts, in: *Clinical Orthopaedics and Related Research*. Lippincott Williams and Wilkins, pp. 75–82. <https://doi.org/10.1097/00003086-200211000-00013>

- Luciano, V., Sardini, E., Serpelloni, M., Baronio, G., 2014. An energy harvesting converter to power sensorized total human knee prosthesis. *Meas. Sci. Technol.* 25, 025702. <https://doi.org/10.1088/0957-0233/25/2/025702>
- Mannion, A.F., Kämpfen, S., Munzinger, U., Kramers-de Quervain, I., 2009. The role of patient expectations in predicting outcome after total knee arthroplasty. *Arthritis Res. Ther.* 11. <https://doi.org/10.1186/ar2811>
- Platt, S.R., Farritor, S., Garvin, K., Haider, H., 2005. The use of piezoelectric ceramics for electric power generation within orthopedic implants. *IEEE/ASME Trans. Mechatronics* 10, 455–461. <https://doi.org/10.1109/TMECH.2005.852482>
- Rao, A.R., Engh, G.A., Collier, M.B., Lounici, S., 2002. Tibial interface wear in retrieved total knee components and correlations with modular insert motion. *J. Bone Joint Surg. Am.* 84, 1849–55. <https://doi.org/10.2106/00004623-200210000-00017>
- Renishaw plc, 2017. Ti6Al4V ELI-0406 powder for additive manufacturing [WWW Document]. URL <https://resources.renishaw.com/en/details/data-sheet-ti6al4v-eli-0406-powder-for-additive-manufacturing--94700>
- Safaei, M., Meneghini, R.M., Anton, S.R., 2017. Parametric analysis of electromechanical and fatigue performance of total knee replacement bearing with embedded piezoelectric transducers. *Smart Mater. Struct.* 26. <https://doi.org/10.1088/1361-665X/aa814e>
- Scott, C.E.H., Howie, C.R., MacDonald, D., Biant, L.C., 2010. Predicting dissatisfaction following total knee replacement: A prospective study of 1217 patients. *J. Bone Jt. Surg. - Ser. B* 92, 1253–1258. <https://doi.org/10.1302/0301-620X.92B9.24394>
- Sisko, Z.W., Teeter, M.G., Lanting, B.A., Howard, J.L., McCalden, R.W., Naudie, D.D., MacDonald, S.J., Vasarhelyi, E.M., 2017. Current Total Knee Designs: Does Baseplate Roughness or Locking Mechanism Design Affect Polyethylene Backside Wear? *Clin. Orthop. Relat. Res.* 475, 2970–2980. <https://doi.org/10.1007/s11999->

017-5494-3

- Teeter, M.G., Lanting, B.A., Shrestha, K.R., Howard, J.L., Vasarhelyi, E.M., 2015. Contribution of Surface Polishing and Sterilization Method to Backside Wear in Total Knee Arthroplasty. *J. Arthroplasty* 30, 2320–2322.
<https://doi.org/10.1016/j.arth.2015.06.036>
- Telford, J.K., 2007. A brief introduction to design of experiments. *Johns Hopkins APL Tech. Dig. (Applied Phys. Lab. 27, 224–232.*
- Toms, A.D., Mandalia, V., Haigh, R., Hopwood, B., 2009. The management of patients with painful total knee replacement. *J. Bone Jt. Surg. - Ser. B* 91, 143–150.
<https://doi.org/10.1302/0301-620X.91B2.20995>
- Wahid, Z., Nadir, N., 2013. Improvement of one factor at a time through design of experiments. *World Appl. Sci. J.* 21, 56–61.
<https://doi.org/10.5829/idosi.wasj.2013.21.mae.99919>
- Wasielewski, R.C., Parks, N., Williams, I., Surprenant, H., Collier, J.P., Engh, G., 1997. Tibial insert undersurface as a contributing source of polyethylene wear debris. *Clin. Orthop. Relat. Res.* 53–9.

Chapter 3

3 Experimental Validation and Load Imbalance Measurements of a Compliant Package Design

Overview: *The stiffness of the package was determined from axial compressive loads applied to the package. The package also underwent simulated load imbalances to measure differences between the medial and lateral compartmental forces measured by surrogate sensors.*

3.1 Introduction

Proper implant alignment and soft tissue balancing are imperative for favourable patient outcomes and implant longevity. Intraoperative sensors have been used to objectively ensure that implant components are positioned correctly, and as a useful tool for ligament balancing by providing real-time quantitative feedback (Cho et al., 2018; Elmallah et al., 2016; Kenneth A Gustke et al., 2014; Kenneth A. Gustke et al., 2014). All possible preemptive measures can be taken to minimize future implant failures intraoperatively, but the condition of an implant can change over the course of healing. Currently, there is no quantitative method of monitoring the postoperative loads transmitted in one's prosthetic knee available for routine clinical use.

The benefit of instrumented implants is the ability to better understand the *in vivo* mechanics of a patient's TKR. The ability to measure tibial forces can help identify signs of instability, and aseptic loosening. Measured loads can be used to corroborate patient histories so that the most suitable actions can be made to improve implant longevity.

The triboelectric effect can be used for both load sensing and energy harvesting applications. TEGs developed by Ibrahim et al. are designed to operate between the UHMWPE bearing and tibial tray. The motivation behind the design of the compliant package described in Chapter 2 was to integrate the TEG in a commercially available TKR system.

This objective of this chapter is the experimental validation of the computational model presented in Chapter 2, and to measure the effect of intentional load imbalances on the deflection of a package prototype. A manufactured prototype underwent uniaxial compression testing to determine the stiffness of the prototype and how this value deviates from the stiffness determined from the computational model. In addition, several simplified structures underwent compression testing. The stiffness of the manufactured simplified structures was also compared to their corresponding computational models. Using embedded load sensors, the medial and lateral compartment forces were measured as the mediolateral load distribution oscillated between a medial and a lateral load bias during simulated abduction/adduction.

3.2 Materials and Methods

3.2.1 Manufactured Prototype

Alterations were made to the prototype CAD model in Chapter 2 prior to manufacturing and mechanical testing. Since the package was intended to accommodate the TEGs, access to the interior of the package was achieved by printing the prototype into two interlocking, separate parts. The interlocking geometry between the parts provides resistance to relative transverse displacements. Additionally, using the acquired STL file of a size 7 Triathlon tibial tray and PE bearing, the *Scanto3D* add-in in Solidworks was used to recreate the interlocking geometry of the TKR components on the top and bottom surfaces of the package. The parts were fastened together using three M3 x 0.05 6mm long flat head screws to prevent removal of the top plate. Threaded holes were located at the medial, lateral and posterior locations of the prototype. Once these alterations were completed, the prototype was manufactured using selective laser melting (Figure 3-1). The printing parameters are outlined in Table 3-1. The resulting prototype assembly was used in the subsequent experiments.

Table 3-1- Selective Laser Melting Parameters

Laser Power [W]	400
Laser Diameter [μm]	70
Layer Thickness [μm]	40
Powder Size Diameter [μm]	15-45
Heat Treatment Process	With argon supply on, 60 minutes to 350°C, hold at 350°C for 30 minutes. 60 minutes to 850°C, hold at 850°C for 60 minutes. Cool the furnace down slowly.
Surface Finish	Grit Blast ($\sim 5\text{-}10\mu\text{m } R_a$)

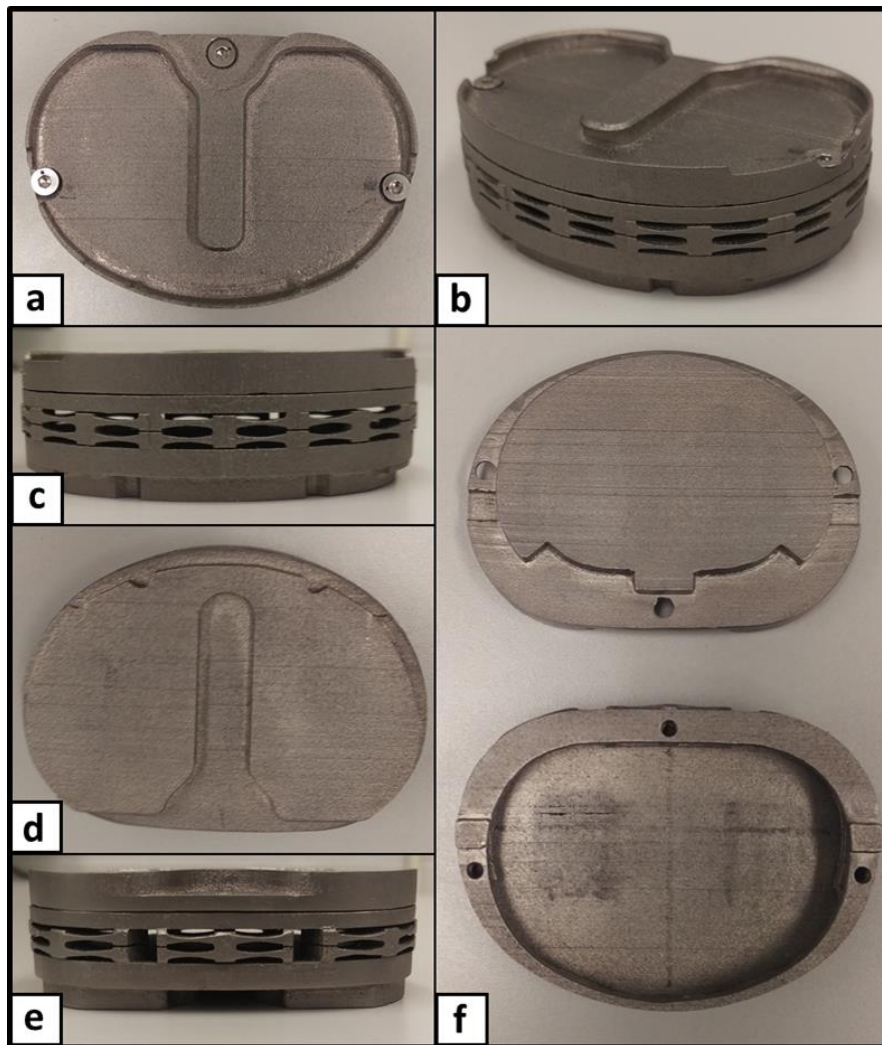


Figure 3-1- Package Prototype: (a) top view, (b) isometric view, (c) front view, (d) bottom view, (e) back view and (f) disassembled prototype.

3.2.2 Axial Loading of Package Prototype

In order to compare the stiffness of the computational model and the manufactured prototype, an Instron 8874 mechanical testing machine (Instron, Norwood, MA) equipped with a 5 kN load cell was used to measure the stiffness of the prototype. The prototype was placed along the vertical axis of the actuator on a metal stand used to raise the specimen within the actuator's line of travel. The actuator was translated downwards in displacement until in contact with the prototype, as indicated by changes in force

measured by the load cell in series with the prototype. In force control, contact between the load cell and the prototype was initially set by applying 500 N of compression. The further axial compressive load was then applied at a rate of 26 N/s up to a maximum of 1800 N. The displacement of the crosshead was acquired at a sampling rate of 1000 samples/s. Afterwards, the stiffness of the stand and load frame was acquired by performing the same loading protocol that was applied to the prototype with the only exception of swapping the prototype with a rigid, metal block. In order to correct for the compliance of the experimental set-up, the compliance of the prototype was isolated by subtracting the compliance determined from compressing the rigid block from the system that contained the prototype. The stiffness of the prototype was compared to the stiffness of the computational model presented in the previous chapter to quantify if there is agreement between the experimental and computational models.

3.2.3 Imbalance Testing

Compression and simulated load imbalances were applied using a VIVO joint motion simulator (Advanced Mechanical Technology, Inc, Watertown, MA) capable of applying loads and displacements in all 6 degrees-of-freedom (DOF). A Triathlon Knee System (Stryker, Kalamazoo, MI) was used for the design and testing of the package. The femoral component was cemented on a femoral component holder secured to the abduction arm of the VIVO using polymethylmethacrylate (PMMA) bone cement (Bosworth Fastray, Keystone Industries, Myerstown, PA). While the abduction arm of the VIVO was positioned at 0° of abduction/adduction and with the femoral component holder attached to the abduction arm, a sagittal plane defined midway between the femoral component's condyles was positioned to intersect the origin of the flexion and abduction arm along the mediolateral axis (Figure 3-2). On the lower actuator of the VIVO, the tibial tray was cemented on a custom fixture using dental cement (Dentstone, Kulzer, LLC, South Bend, IN).

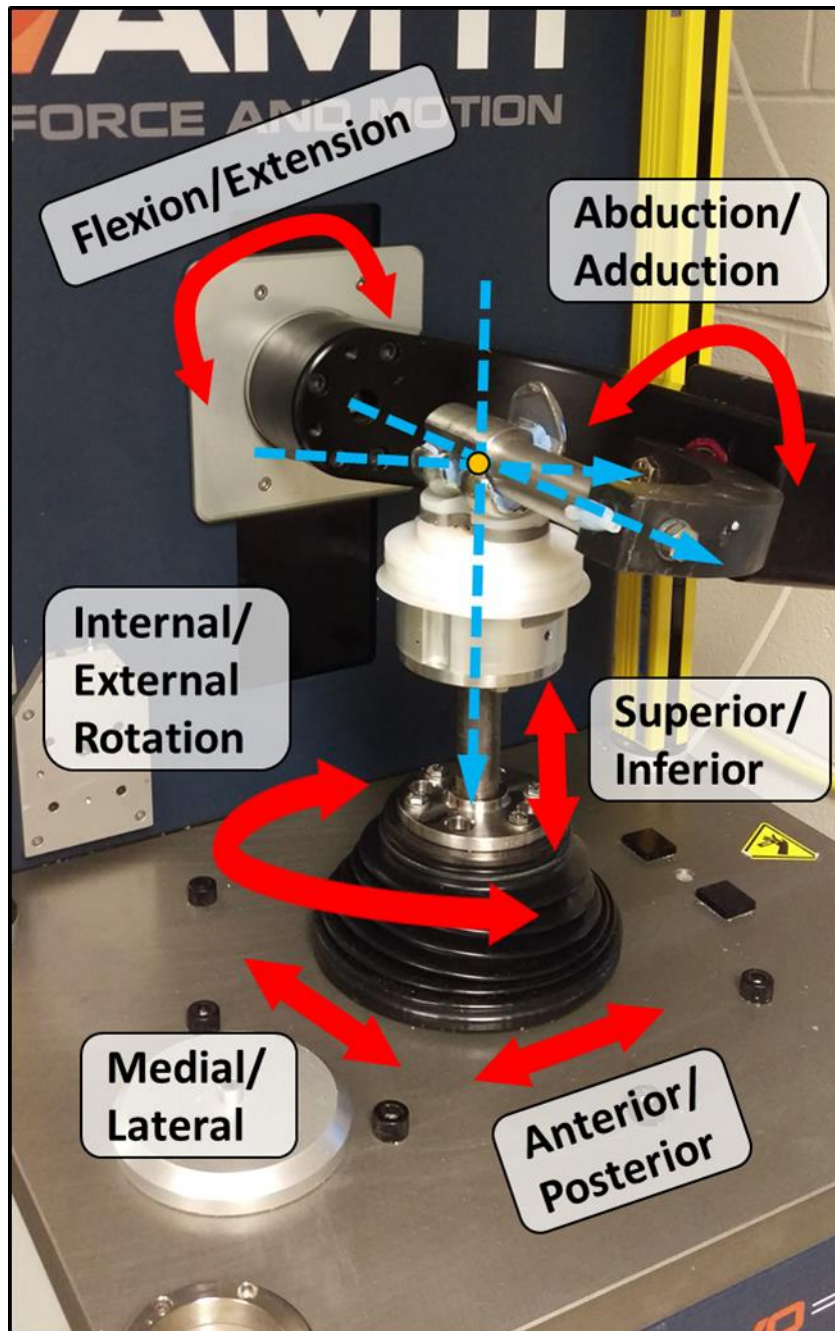


Figure 3-2- The VIVO joint simulator operates in six degrees of freedom. There are three translational (medial/lateral, anterior/posterior, superior/inferior) and three rotational degrees of freedom (internal/external, abduction/adduction, flexion/extension).

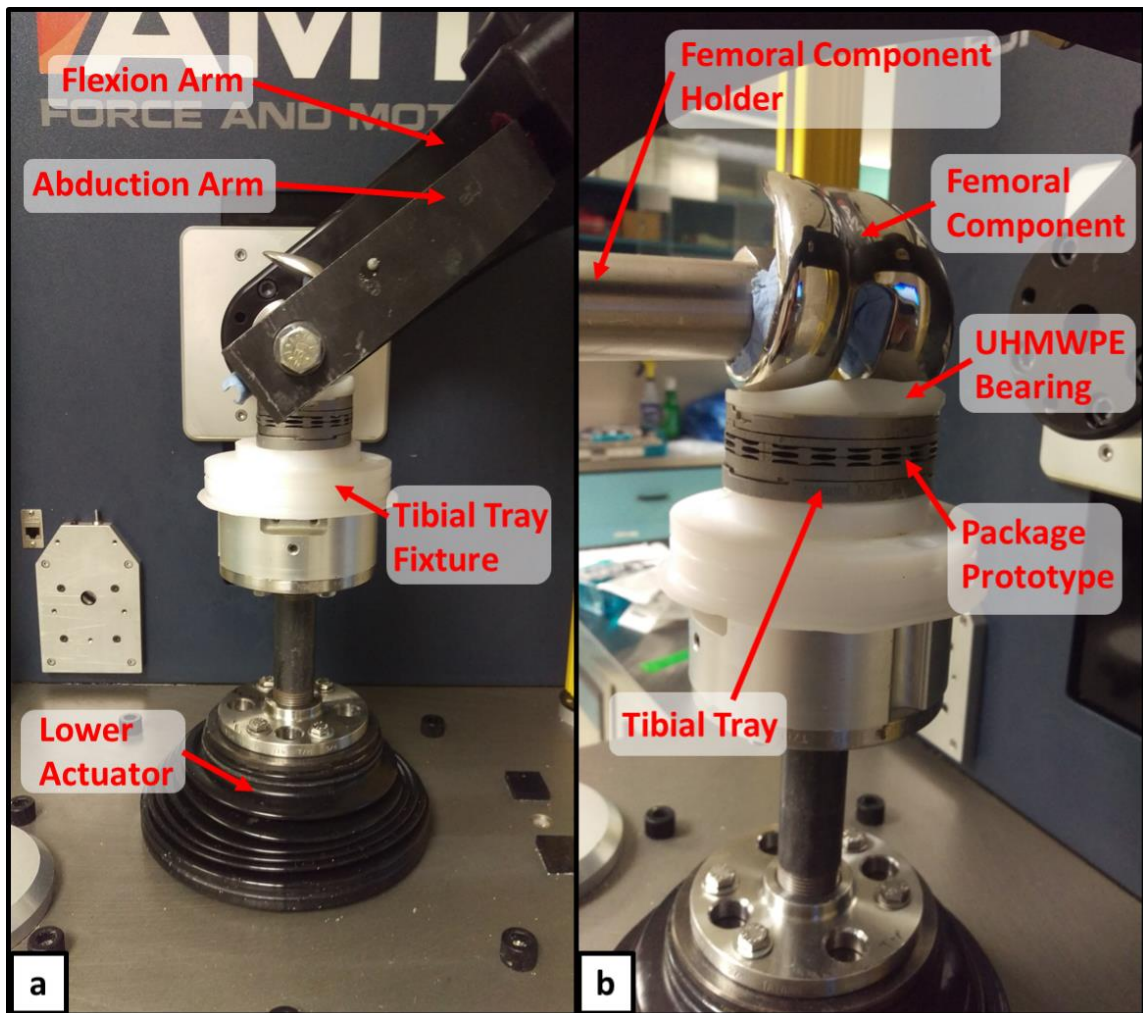


Figure 3-3- Experimental set-up (the implant flexed about 60° for clarity)

At the time of the experiment, suitably capable TEG components were not available for experimental testing. Thus, ultra-thin Flexiforce sensors (Tekscan, Boston, MA), rated for up to 111 N (25 lbs.), were employed. Castable silicone (Amazing Remelt, Alumilite Corporation, Kalamazoo, MI) with the shape of the sensing element of the Flexiforce sensors was used to occupy the excess vertical space within the package and transmit loads through the Flexiforce sensors. The height of the silicone spacers was made to have a height slightly greater than the height of the internal void. This was done to ensure

contact between the Flexiforce sensors and the top plate. Based on the Shore A hardness of the silicone, provided by the manufacturer's specifications, the stiffness of a silicone spacer was calculated to be 43 N/mm. With the stiffness of the package determined from the computational model in Chapter 2 (11 818 N/mm) and the calculated silicone stiffness, the approximate amount of load that would be transmitted through the Flexiforce sensors at the maximum load of 2600 N was determined. Assuming equal loading is applied between the compartments, approximately 10 N would be transmitted through one of the Flexiforce sensors. The package transmits the majority of the load since it is stiffer than the silicone. The 111 N (25 lbs.) sensors were chosen because the low-load (4.4 N) rated sensors would most likely be saturated whereas the resolution may be too large with the high-load (445 N) rated sensors at the expected load of 10 N.

3.2.3.1 Flexiforce Sensor Calibration

Calibration of the Flexiforce sensors was performed using weights ranging from 0.45 kg (1 lbs.) to 5 kg (11 lbs.). The maximum test weight of 5 kg, which would exceed the expected Flexiforce load of 10 N, was selected to avoid possible output voltage saturation. A data acquisition (DAQ) card (National Instruments Corporation, Austin, TX) that was connected to the output voltage terminal of a Flexiforce Quickstart Board (Tekscan, Boston, MA) and a custom Labview (National Instruments Corporation, Austin, TX) program were used to acquire the output voltage from the Quickstart Board. Power to the Flexiforce Quickstart Board was supplied by a 9 V battery connected to the positive and negative input terminals. With a 111 N (25 lbs.) rated Flexiforce sensor connected to the Flexiforce Quickstart Board, the largest weight of 5 kg was placed on the Flexiforce's sensing element. The feedback resistance was adjusted with the potentiometer located on the Flexiforce Quickstart Board until the output voltage was 80% to 90% of the 5 V maximum output voltage. Afterwards, the full test weight was removed. The corresponding output voltages for 0.45, 0.9, 1.36 and 2.26 kg weights were acquired. A linear plot of the voltage-force relationship and the resulting line of best fit was acquired for subsequent experiments. The same calibration procedure was conducted with another 111 N (25 lbs.) rated Flexiforce sensor.

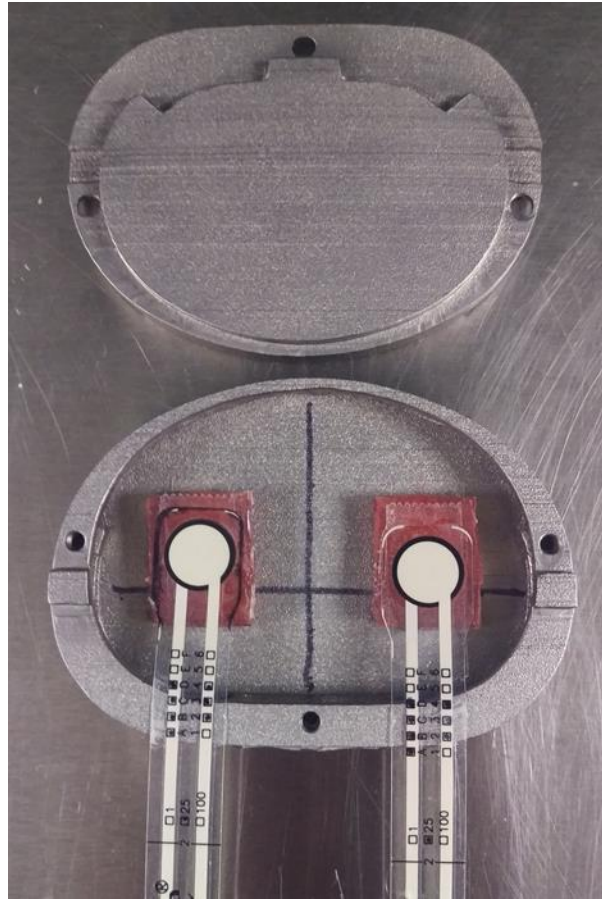


Figure 3-4- Package Prototype with Embedded Flexiforce Sensors in the Medial and Lateral Compartments

3.2.3.2 Experimental Set-Up

The vertical displacement from the VIVO joint simulator during axial loading was used to measure the deflection of the prototype. However, machine and fixture compliance are expected during testing. In order to eliminate the effects of the machine and fixture compliance, the TKR was tested with and without the prototype. By knowing the stiffness of both test configurations, the stiffness of the prototype could be isolated. The force and kinematic data from the VIVO were acquired at a rate of 100 Hz. The actuator position resolution is ± 0.1 mm.

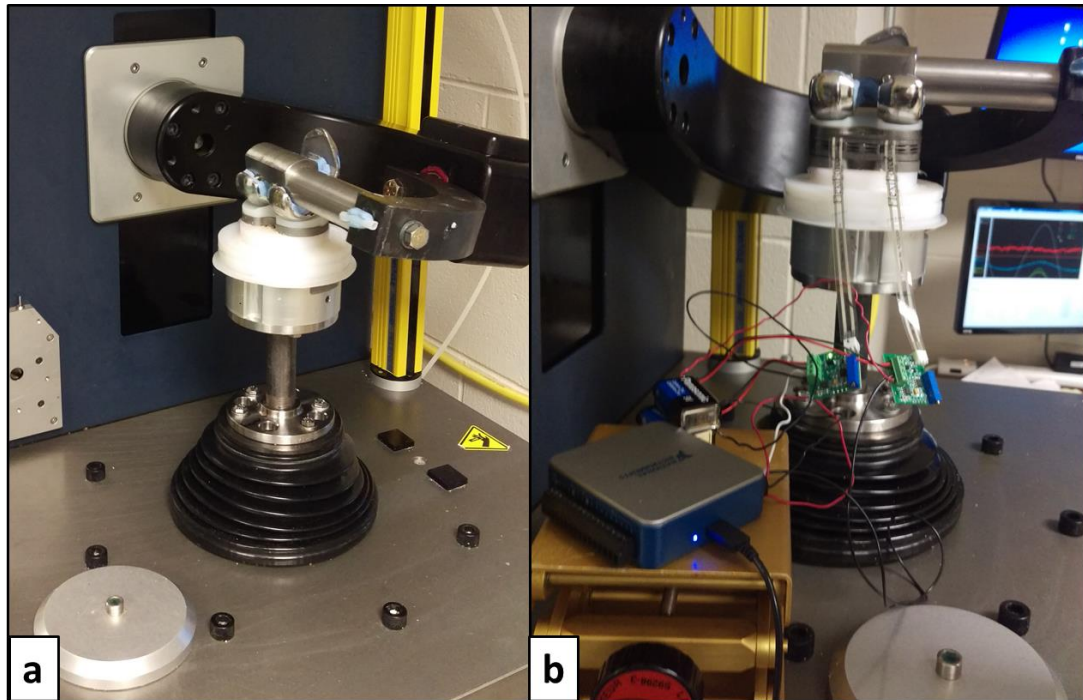


Figure 3-5- Experimental set-up configurations: a) TKR mounted on VIVO joint simulator and b) TKR mounted on VIVO joint simulator with package prototype embedded with Flexiforce sensors.

In both testing configurations, the initial pose of the experimental set-up was determined by reducing the joint with a 50 N compressive load, while maintaining 0 N of force (or 0 Nm of torque) for all other remaining DOFs other than flexion. Flexion was set to 0° , or full extension. Once the initial position of the joint was defined, a sinusoidal compressive load ranging from 50 N to 2600 N was applied at 0.5 Hz. The stiffness of the experimental set-ups with and without the package prototype were calculated using the vertical displacement acquired from the VIVO and the applied force. The stiffness of the package was then calculated by subtracting the stiffness of the experimental set-up without the package from the stiffness of the TKR with the package. In addition to the prototype's deflection measured by the VIVO, the Flexiforce sensors measured the compartmental loads.

A static compressive load of 2600 N was applied to the Flexiforce embedded prototype. Loading perturbations were superimposed atop the 2600 N compressive load. To simulate a load imbalance along the coronal plane, a sinusoidal abduction-adduction (AA) load of ± 20 Nm was applied. Using the medial force ratio distribution reported by Halder et al and Kutzner et al (Halder et al., 2014; Kutzner et al., 2013), 20 Nm of tibial adduction and an axial load of 2600 N, 65% of the total axial load would be transmitted through the medial compartment. An abduction moment of 20 Nm would shift the majority of the axial load laterally in which the medial compartment carries 35% of the mediolateral force distribution. All remaining DOF in each loading scenario maintained 0 N of force, or 0 Nm of torque. The cyclic loads were applied at a frequency of 0.5 Hz. Loads measured by the Flexiforce sensors and the VIVO joint simulator were recorded during loading.

3.3 Results

3.3.1 Axial Loading of Package Prototype

During the cyclic compression testing, using the VIVO, the package had a stiffness of 4555 N/mm. With the Instron, the stiffness of the test fixture was 8712 N/mm. The fixture with the prototype mounted had a stiffness of 2615 N/mm (Figure 3-6). In order to nullify the stiffness of the test fixture, it was assumed the test fixture and the prototype were compressed in series. The prototype's stiffness was calculated to be 3190 N/mm. This is 8628 N/mm, or 73%, less than what was predicted by the computational model in Chapter 2.

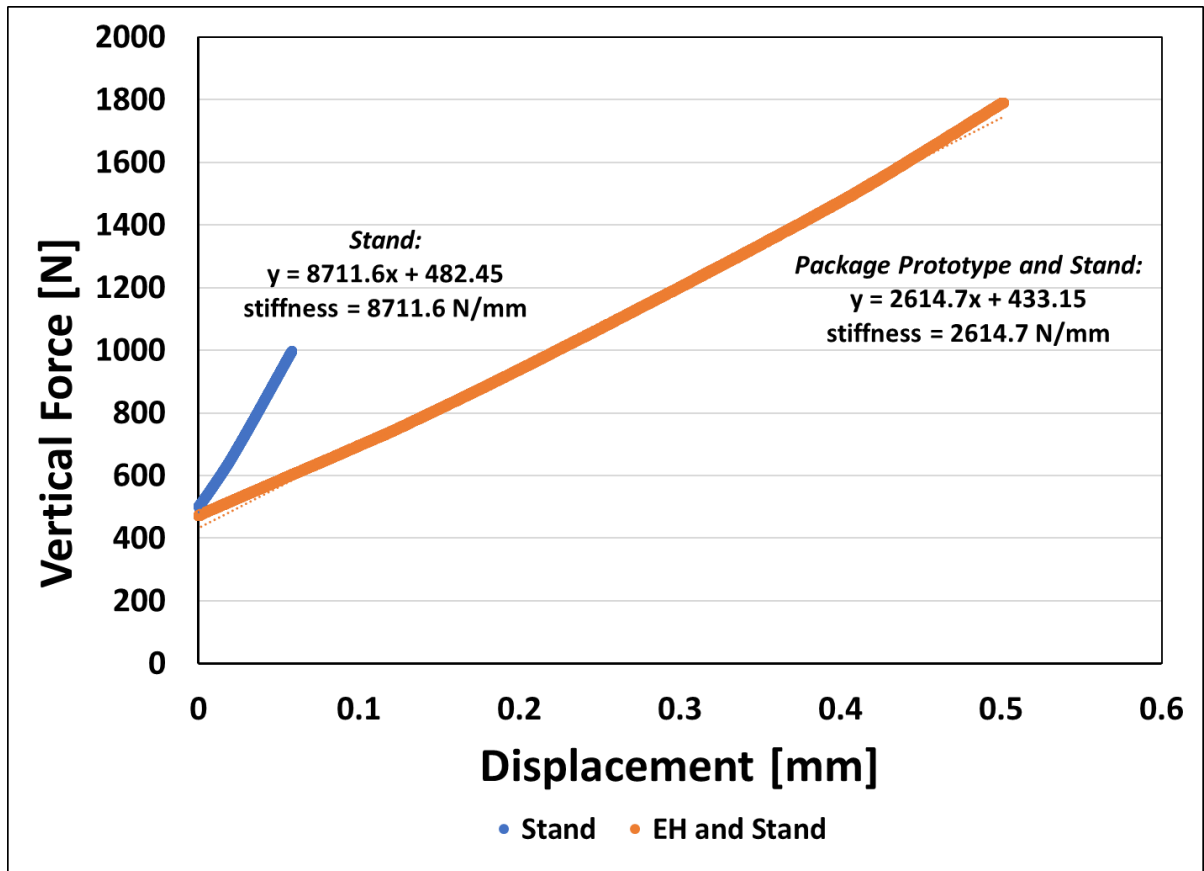


Figure 3-6- Force vs. displacement plot of package prototype subjected to uniaxial vertical loading.

3.3.2 Imbalance Testing

During simulated coronal imbalance testing, as expected, the Flexiforce sensors showed opposite responses to the AA moment, however the magnitudes were not identical. This was probably due to the geometric and positional variance of the silicone spacers beneath the Flexiforce sensors. When a 20 Nm adduction moment was applied, the medial compartment force sensor experienced a 23% load increase versus a 33% decrease at the lateral compartment force sensor with respect to the static 2600 N compression. When a 20 Nm abduction moment was applied, the medial compartment load decreased by 8%, while the lateral compartment load increased by 8%.

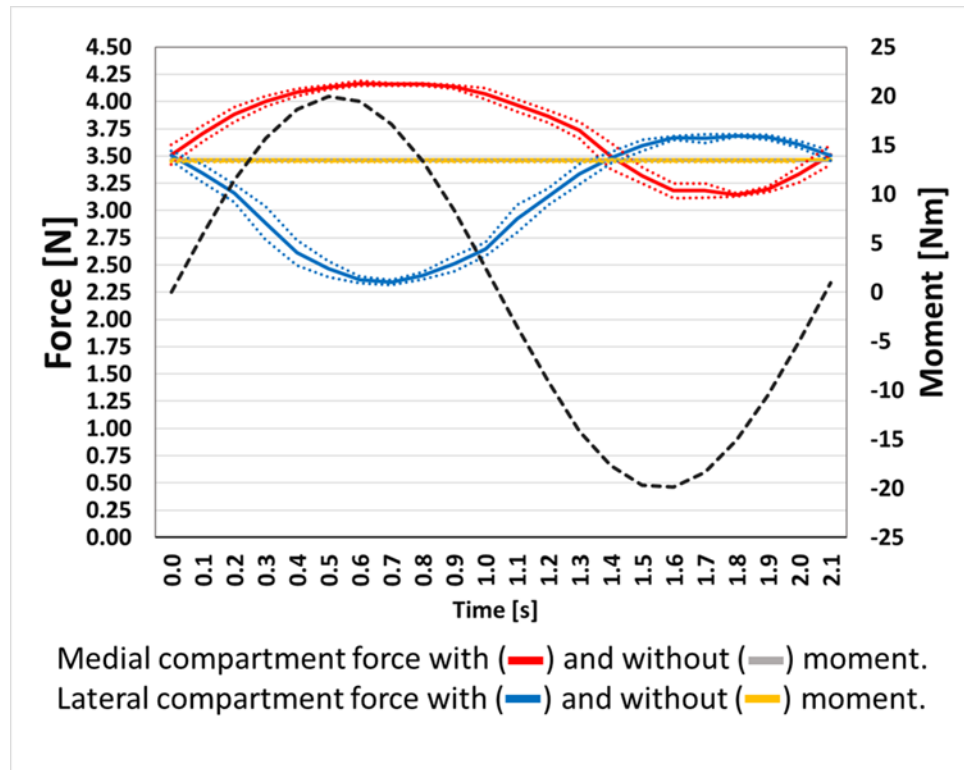


Figure 3-7- Flexiforce measurements during cyclic abduction/adduction.

3.4 Discussion

3.4.1 Stiffness of Additively Manufactured Parts

In this study, the stiffness of an additively manufactured prototype was experimentally determined for the purpose of measuring the difference with respect to the stiffness calculated in the computational model presented in the previous chapter. The prototype's stiffness, under axial loading, was 73% less than what was predicted in the computational model.

Additively manufactured structures have been shown to have stiffness that vary greatly from the stiffness determined from computational models which may be due to geometric discrepancies. The internal porosity, unfused material, and surface roughness can reduce the effective cross-sectional area of the 3D printed prototypes. As a result, additively manufactured parts may not possess the stiffness suggested by their respective

computational models. In some cases, computational models can have stiffness values that are greater than additively manufactured structures by a factor of 4 (Harrysson et al., 2008). Additional manufactured simplified designs with a similar elastic body structure underwent uniaxial vertical loading. Discrepancies between the computational and experimental models were observed with these simplified designs. These results are outlined in Appendix C. Despite the difference between the computational and experimental models, it can be valuable to understand the implications of considering SLM Ti6Al4V as a manufacturing method.

3.4.2 Intercompartmental Load Measurements

The prototype was also subjected to cyclic AA loading to quantify differences in the package's deflection as the tibiofemoral load distribution changes. During AA testing, compartmental loads from the Flexiforce sensors did indicate a shift in the load along the mediolateral axis. However, the measured loads at peak abduction and adduction did not show a symmetric response. The medial compartment measured 64% and 46% of the total load in full adduction and abduction, respectively. The measured compartmental loads did not display a symmetrical force response at the maximum and minimum loads, or displacements, of the perturbed loading scenarios. This may be attributed to the load sensor calibration, inconsistent silicone fill levels, and the placement of the load sensors within the package.

The ability to measure the tibiofemoral forces about the anteroposterior axis can help detect signs of future implant complications such as malalignment. Large abduction or adduction angles, greater than 3° , has been shown to increase the intercompartmental load difference (Bäthis et al., 2004; Halder et al., 2014). Higher AA moments may entail increased stresses in the surrounding implant components and underlying bones, PE bearing wear (Collier et al., 2007; Srivastava et al., 2012) and aseptic loosening (Gromov et al., 2014; Ritter et al., 2011). Kutzner et al. have demonstrated a correlation between tibiofemoral alignment and mediolateral force distribution where varus alignment leads to increased medial compartment loads. Medial force ratios of 70% to 80% can be expected

with a knee that is 3° varus (Kutzner et al., 2017). The prototype with embedded Flexiforce sensors has demonstrated the ability to measure the compartmental loads during the application of a cyclic AA moment. The package was compliant enough in the medial and lateral compartments to measure loads as the AA angle oscillated between $\pm 2^\circ$ during AA loading. The package most likely will be able to detect the increased coronal planeload imbalances associated with AA angles greater than 3° which can be beneficial in restoring a more even mediolateral load distribution through interventions such as soft tissue balancing.

A limitation to this study is that the performance of the TEGs, with this current package design, was not quantified. In spite of this, thin Flexiforce sensors were used in lieu of the TEGs due to their unavailability at the time of testing. Silicone spacers were placed underneath the sensors. Silicone was selected because of its low stiffness relative to the stiffness of the package. The low stiffness silicone reduced the interference the spacers had on the force transmitted through the package. However, silicone may not have been an ideal choice. Visual signs of plastic deformation, or indentations of the Flexiforce sensors, were seen on the silicone spacers after testing. This means that the measured loads acquired by the Flexiforce sensors may be inaccurate since a portion of the load was transmitted to the silicone that was not covered by the sensing element of the Flexiforce sensors.

Future testing can be performed to quantify the measured compartmental loads and power generated by the TEGs embedded in the package. Further tuning of the package may need to be done to maximize the electricity generated.

3.5 Conclusion

From uniaxial compression testing of the prototype, the AM Ti6Al4V components were more compliant as determined from their corresponding computational models. Despite this stiffness discrepancy between the experimental and computational models, the prototype deflected proportionally to shifts in the mediolateral load distribution. The

compartmental loads measured with this package design in conjunction with embedded sensors can be a means of better understanding the effects of surgical technique and implant design on stability after implantation.

3.6 References

- Bäthis, H., Perlick, L., Tingart, M., Lüring, C., Zurakowski, D., Grifka, J., 2004. Alignment in total knee arthroplasty. A comparison of computer-assisted surgery with the conventional technique. *J. Bone Jt. Surg. - Ser. B* 86, 682–687. <https://doi.org/10.1302/0301-620X.86B5.14927>
- Cho, K.-J., Seon, J.-K., Jang, W.-Y., Park, C.-G., Song, E.-K., 2018. Objective quantification of ligament balancing using VERASENSE in measured resection and modified gap balance total knee arthroplasty. *BMC Musculoskelet. Disord.* 19, 266. <https://doi.org/10.1186/S12891-018-2190-8>
- Collier, M.B., Engh, C.A., McAuley, J.P., Engh, G.A., 2007. Factors Associated with the Loss of Thickness of Polyethylene Tibial Bearings After Knee Arthroplasty. *J. Bone Jt. Surg.* 89, 1306–1314. <https://doi.org/10.2106/JBJS.F.00667>
- Elmallah, R.K., Mistry, J.B., Cherian, J.J., Chughtai, M., Bhave, A., Roche, M.W., Mont, M.A., 2016. Can We Really “Feel” a Balanced Total Knee Arthroplasty? *J. Arthroplasty* 31, 102–105. <https://doi.org/10.1016/J.ARTH.2016.03.054>
- Gromov, K., Korchi, M., Thomsen, M.G., Husted, H., Troelsen, A., 2014. What is the optimal alignment of the tibial and femoral components in knee arthroplasty? An overview of the literature. *Acta Orthop.* 85, 480–487. <https://doi.org/10.3109/17453674.2014.940573>
- Gustke, Kenneth A., Golladay, G.J., Roche, M.W., Elson, L.C., Anderson, C.R., 2014. A new method for defining balance: Promising Short-Term Clinical Outcomes of Sensor-Guided TKA. *J. Arthroplasty* 29, 955–960. <https://doi.org/10.1016/j.arth.2013.10.020>
- Gustke, Kenneth A, Golladay, G.J., Roche, M.W., Elson, L.C., Anderson, C.R., 2014. Primary TKA patients with quantifiably balanced soft-tissue achieve significant clinical gains sooner than unbalanced patients. *Adv. Orthop.* 2014, 628695.

<https://doi.org/10.1155/2014/628695>

Halder, A., Kutzner, I., Graichen, F., Heinlein, B., 2014. Influence of Limb Alignment on Mediolateral. *J. Bone Jt. Surg.* 94, 1023–1029.

Harrysson, O.L.A., Cansizoglu, O., Marcellin-Little, D.J., Cormier, D.R., West, H.A., 2008. Direct metal fabrication of titanium implants with tailored materials and mechanical properties using electron beam melting technology. *Mater. Sci. Eng. C* 28, 366–373. <https://doi.org/10.1016/j.msec.2007.04.022>

Kutzner, I., Bender, A., Dymke, J., Duda, G., Von Roth, P., Bergmann, G., 2017. Mediolateral force distribution at the knee joint shifts across activities and is driven by tibiofemoral alignment. *Bone Jt. J.* 99B, 779–787. <https://doi.org/10.1302/0301-620X.99B6.BJJ-2016-0713.R1>

Kutzner, I., Trepczynski, A., Heller, M.O., Bergmann, G., 2013. Knee adduction moment and medial contact force-facts about their correlation during gait. *PLoS One* 8, 8–15. <https://doi.org/10.1371/journal.pone.0081036>

Ritter, M.A., Davis, K.E., Meding, J.B., Pierson, J.L., Berend, M.E., Malinzak, R.A., 2011. The Effect of Alignment and BMI on Failure of Total Knee Replacement. *J. Bone Jt. Surgery-American* Vol. 93, 1588–1596. <https://doi.org/10.2106/JBJS.J.00772>

Srivastava, A., Lee, G.Y., Steklov, N., Colwell, C.W., Ezzet, K.A., D’Lima, D.D., 2012. Effect of tibial component varus on wear in total knee arthroplasty. *Knee* 19, 560–563. <https://doi.org/10.1016/j.knee.2011.11.003>

Chapter 4

4 Durability Testing of Energy Harvester Package

Overview: *The fatigue strength is an important mechanical property to consider in implant design. Ideally, TKRs should withstand repetitive physiological loading for up to several decades of use. In this chapter, the fatigue life of the package prototype was quantified when subjected to a sinusoidal vertical load with maximum and minimum loads that correspond with ISO 14243.*

4.1 Introduction

Ti6Al4V is a common material used for orthopaedic applications because of its high yield strength, low stiffness relative to other metal alloys, biocompatibility, and high fatigue strength. One of the main requirements the compliant package must satisfy is that it must be durable enough to withstand the repetitive loading of activities of daily living. The failure of the package will not only render the energy harvester damaged and unusable, but this can also lead to an introduction of foreign wear particles, and affect the stresses transmitted to the surrounding implant components that may elicit a biological response.

Complex geometries can be manufactured through additive manufacturing (AM) methods such as selective laser melting (SLM). The mechanical properties of AM Ti6Al4V are comparable to its wrought form (Baufeld et al., 2011; Brandl et al., 2010; Chan et al., 2013; Facchini et al., 2010; Koike et al., 2011; Leuders et al., 2013; Murr et al., 2009; Qiu et al., 2013), but AM Ti6Al4V may possess anisotropic microstructure and properties due to the directional nature of AM (Baufeld et al., 2011; Harrysson et al., 2008).

However, the fatigue performance of AM Ti6Al4V is adversely affected by its inherent internal porosity, residual stress, build orientation and surface condition (Baufeld et al., 2011; Brandl et al., 2010; Chan et al., 2013; Edwards and Ramulu, 2014; Ghose et al., 2018; Leuders et al., 2013; Shiomi et al., 2004; Sterling et al., 2015). The poor notch sensitivity of Ti6Al4V makes AM parts susceptible to defects and stress concentrations

(Ahmadi et al., 2018; Hrabe et al., 2011). Internal pores and surface defects can become potential sites for crack initiation and propagation (Ghouse et al., 2018; Yadollahi and Shamsaei, 2017).

Despite the poor fatigue performance of AM Ti6Al4V compared to its wrought form, the post processing performed can improve the fatigue strength by relieving residual stress, improving the microstructure and surface finish (Edwards and Ramulu, 2014; Ghouse et al., 2018; Yadollahi and Shamsaei, 2017). Heat treatment and hot isostatic pressing (HIP) have been shown to homogenize the microstructure through recrystallizing the material, relieving residual stress and fusing un-melted particles (Edwards and Ramulu, 2014; Wycisk et al., 2015; Yadollahi and Shamsaei, 2017). Machined or polished surfaces of specimens that have underwent heat treatment or HIP have increased the fatigue performance by mitigating crack initiation due to surface defects (Edwards and Ramulu, 2014; Wycisk et al., 2015).

As an initial attempt at quantifying the fatigue performance of the compliant package design, two prototypes underwent cyclic axial loading at the maximum vertical load as per ISO 14243 and a reduced vertical load determined from the computational model. Visual indications of fatigue failure were compared to high stress locations in the computational model presented in Chapter 2. AM Ti6Al4V has been observed to have a brittle failure mode as a porous material because of its poor notch sensitivity (Ahmadi et al., 2018; Ghouse et al., 2018; Hrabe et al., 2011). Therefore, cracks may initiate and propagate in the high stress areas indicated in the computational model.

4.2 Materials and Methods

4.2.1 Experimental Set-Up

The same prototype that was used in Chapter 3 underwent fatigue testing (Figure 3-1). A similar experimental set-up as in Chapter 3 was used, however a different joint simulator was utilized for fatigue testing. The Boston joint simulator (AMTI, Watertown, MA) was used to apply a sinusoidal, vertical load to the package prototype. The AMTI Boston

operates in 4 DOF. The vertical actuator of the AMTI Boston operates only in force control. The AP, IE and flexion DOFs operate in displacement control. The remaining DOF, AA and ML, are left unconstrained or constrained. The femoral component was cemented, using PMMA, on a femoral component holder designed to interface with the AMTI Boston. Dentstone cemented the tibial tray on a custom fixture positioned on the lower actuator of the test station. Flexion, AP, and IE DOF were set to zero displacement. The ML DOF was left to translate freely along its axis. The flexion angle was set to 0° (Figure 4-1).

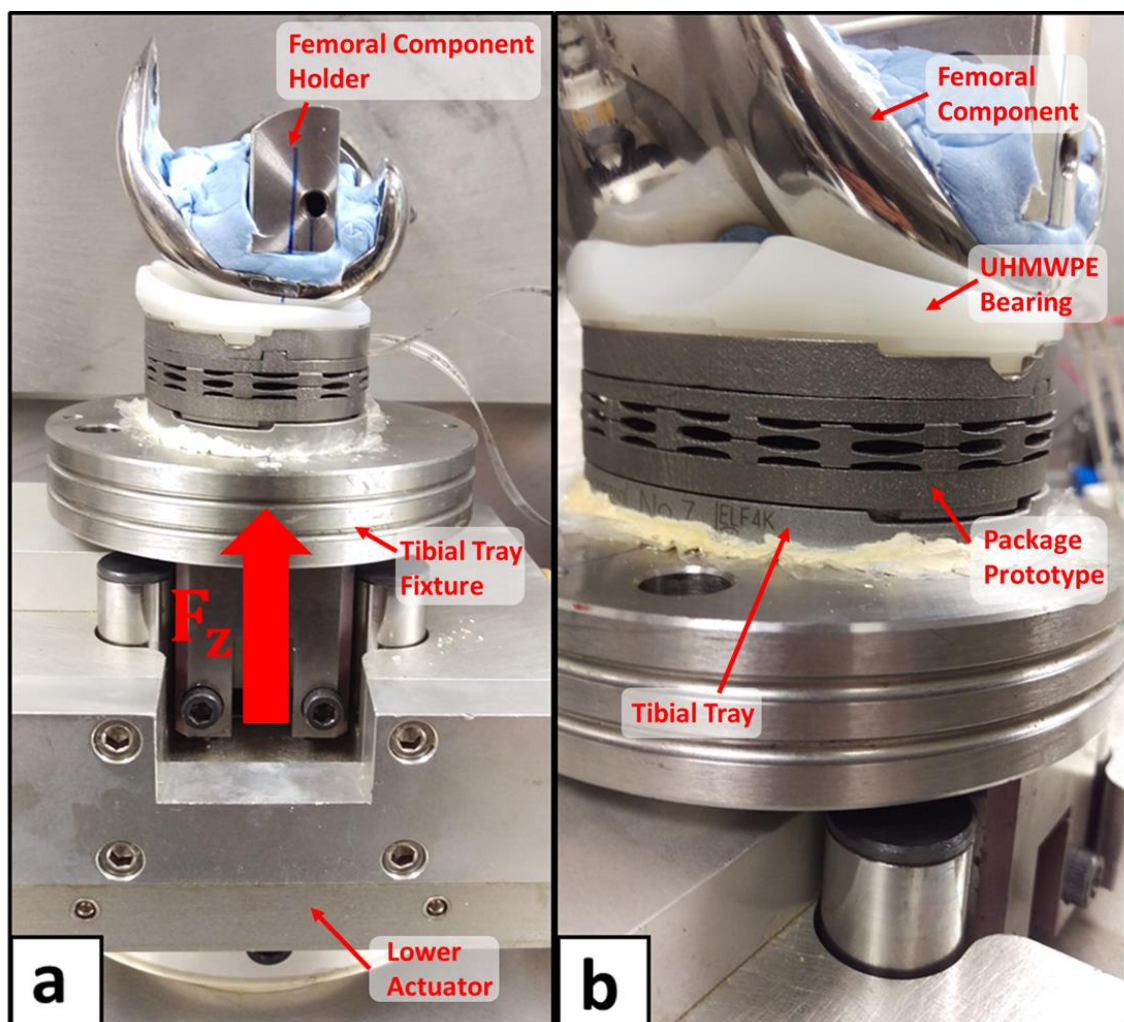


Figure 4-1-Experimental Set-up for Fatigue Testing on AMTI Boston: (a) Medial View, (b) Anteromedial View

4.2.2 Loading Scenario at Maximum Vertical Load

The amplitude of the load waveform was based on the maximum and minimum vertical forces in ISO 14243. The minimum compressive load was 265 N, and the maximum compressive load was 2600 N (ISO, 2009). The sinusoidal load was applied at a rate of 2 Hz. Load and displacement data, from the AMTI Boston, were acquired every 10 000 cycles for 2.5 s at a sampling rate of 200 samples/second. The Boston joint simulator was set to perform a total of 5M cycles in 500k cycle intervals. Because of the brittle fatigue failure of AM Ti6Al4V (Ahmadi et al., 2018; Ghouse et al., 2018; Hrabe et al., 2011), the beams on the prototype were assessed for cracks after removal every 500k cycles. However, the prototype was periodically monitored for cracks during testing. Further fatigue testing was terminated if cracks were detected. The loading scenario used is assumed to be an approximation of the “double-humped”, gait waveform in ISO 14243 at 1 Hz. Because the vertical force in gait has the largest component, and the energy harvester’s electrification mechanism is dependent on the vertical displacement of the package, the shear forces in ISO 14243 were neglected. Furthermore, when the shear forces were considered along with the maximum vertical load in the gait cycle, the shear forces had little effect on the calculated stresses (Figure 4-2). The vertical position of the lower actuator, at the maximum load, was analyzed for changes in the displacement of the package, or for the permanent collapse of the package. The vertical actuator of the AMTI Boston has a resolution of 0.025 mm.

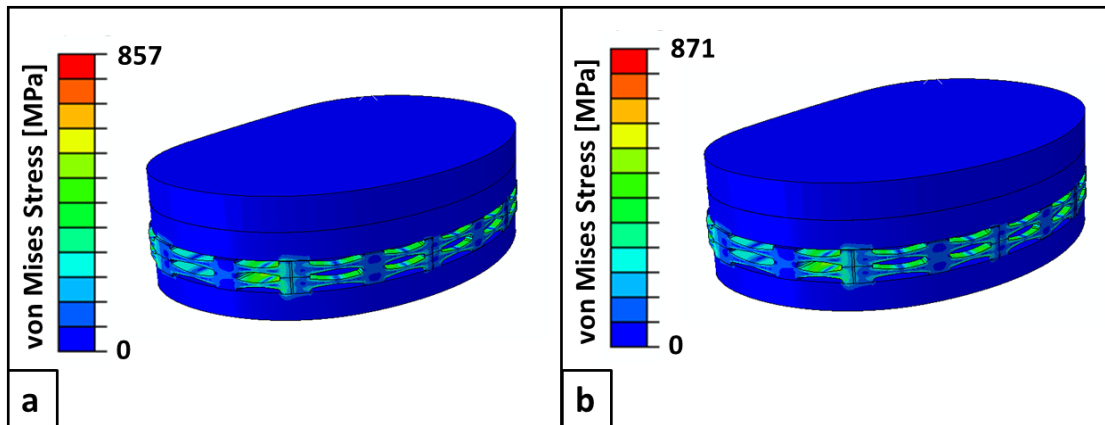


Figure 4-2- von Mises Stress Plots of Maximum Load in Gait Cycle: a) Vertical Load of 2600 N, and b) Vertical Load of 2600 N Superimposed with Corresponding Shear Forces in Percent Gait Cycle (Anteriorly Directed Load of 109 N and Internal Torque of 0.9 Nm).

4.2.3 Reduced Vertical Load

In the computational model of the prototype presented in Chapter 2, the peak stresses were about 800 MPa at the maximum vertical load of 2600 N. Considering that this stress exceeded the fatigue threshold of 550 MPa, an additional prototype was subjected to the same cyclical experiment as the previous prototype but at a reduced load. Additionally, load and displacement data were acquired every 2k cycles. The maximum load was reduced to 1400 N where the peak von Mises stresses did not exceed 500 MPa based on the computational model (Figure 4-3).

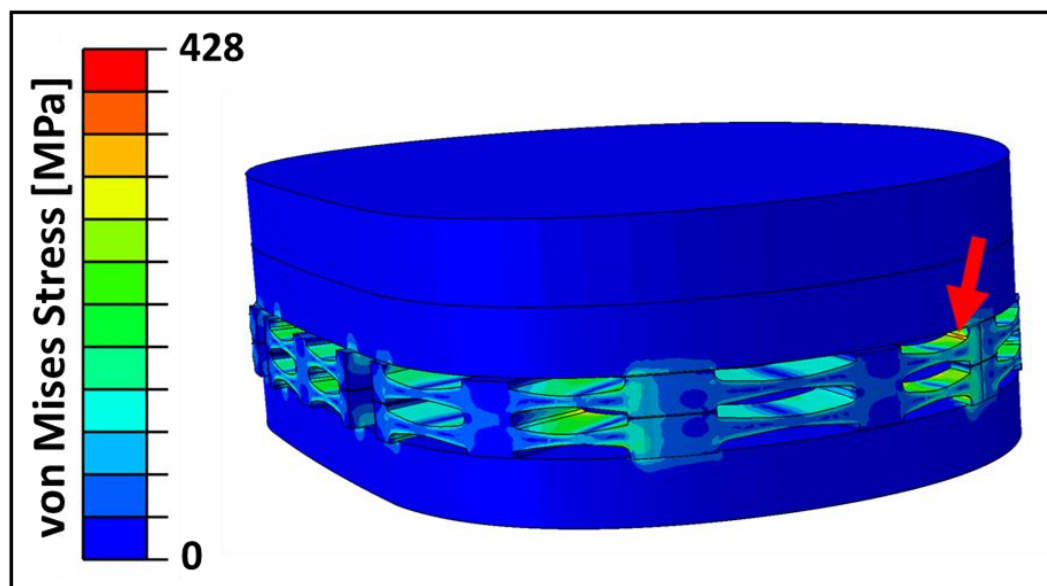


Figure 4-3- Stress plot of the package at a reduced compressive load of 1400 N. The peak stress was below 550 MPa. The red arrow denotes the location of the peak stress.

4.3 Results

4.3.1 Maximum Vertical Load

Fatigue testing was terminated after 140 000 cycles. Cracks were visible at the medial and lateral locations of the package (Figure 4-4). The vertical position of the lower actuator is relative to the flexion axis of the AMTI Boston's upper actuator. Therefore, a decrease in the vertical position at the maximum load indicates the lower actuator translated to a more proximal position relative to the upper actuator. The vertical position, at the maximum applied load, of the lower actuator, decreased by 0.1 mm at 30k cycles. This is assumed to be when the cracks developed (Figure 4-5). The gradual decrease prior to 30k cycles may be due to creep deformation of the PE bearing and plastic deformation of the prototype.

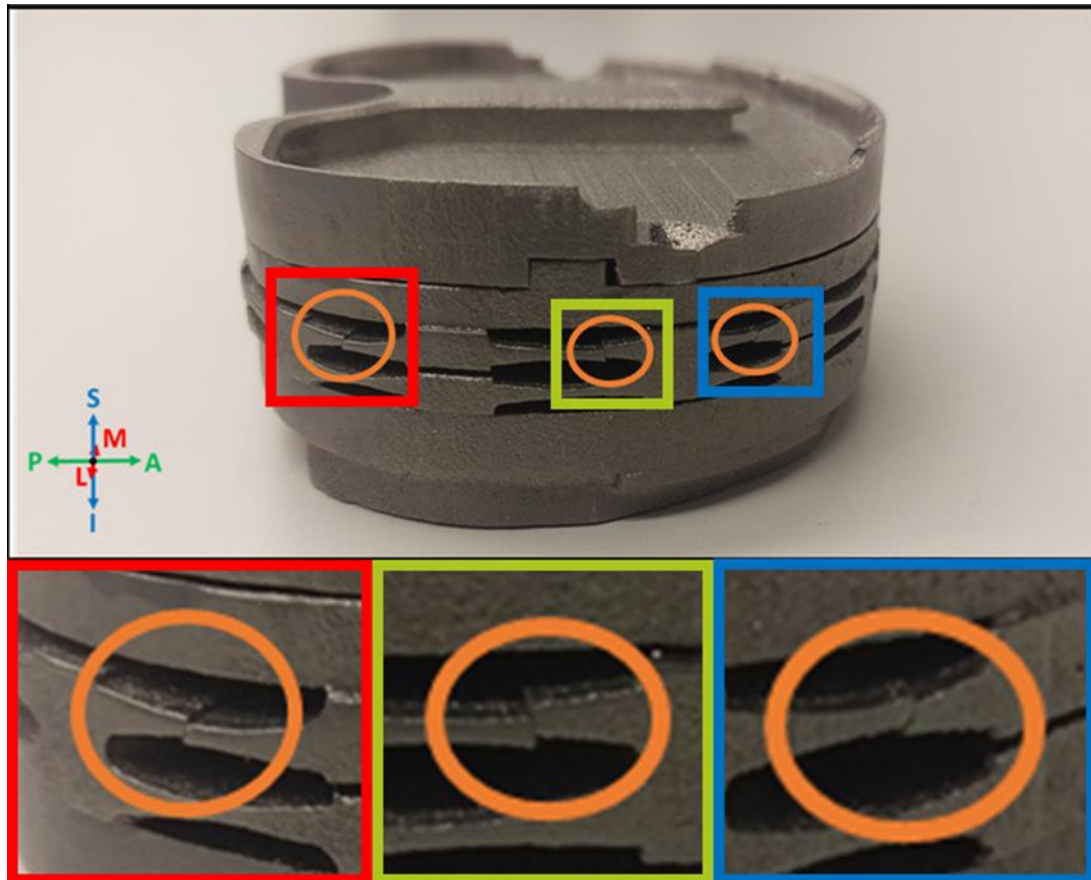


Figure 4-4- Locations of cracks on the lateral side of the prototype after fatigue testing was terminated. Cracks were located in the same locations on the medial side.

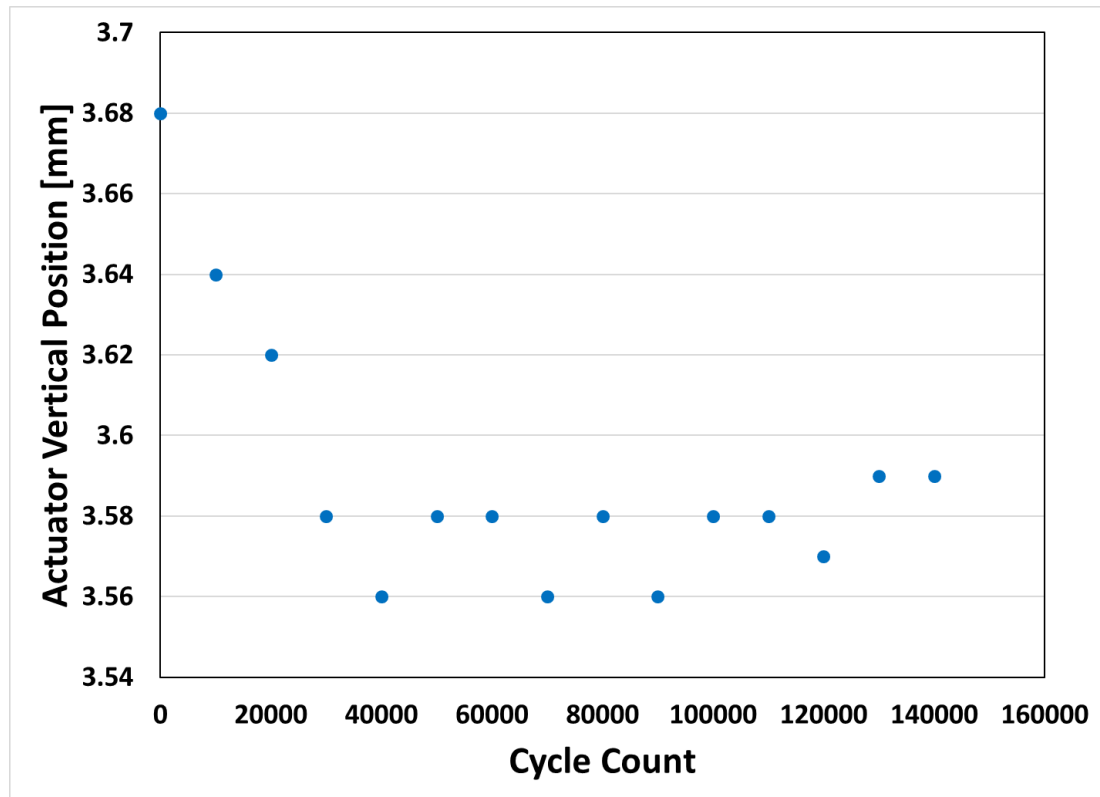


Figure 4-5- Vertical position of lower actuator at the maximum applied load of 2600 N in 10 000 cycle intervals.

4.3.2 Reduced Vertical Load

Despite the reduction in the vertical load, failure occurred around 70k cycles based on the decrease in the vertical position of the actuator's position (Figure 4-6). Cracks were located at the anteromedial and anterolateral regions where the peak stresses were calculated in the computational model (Figure 4-3).

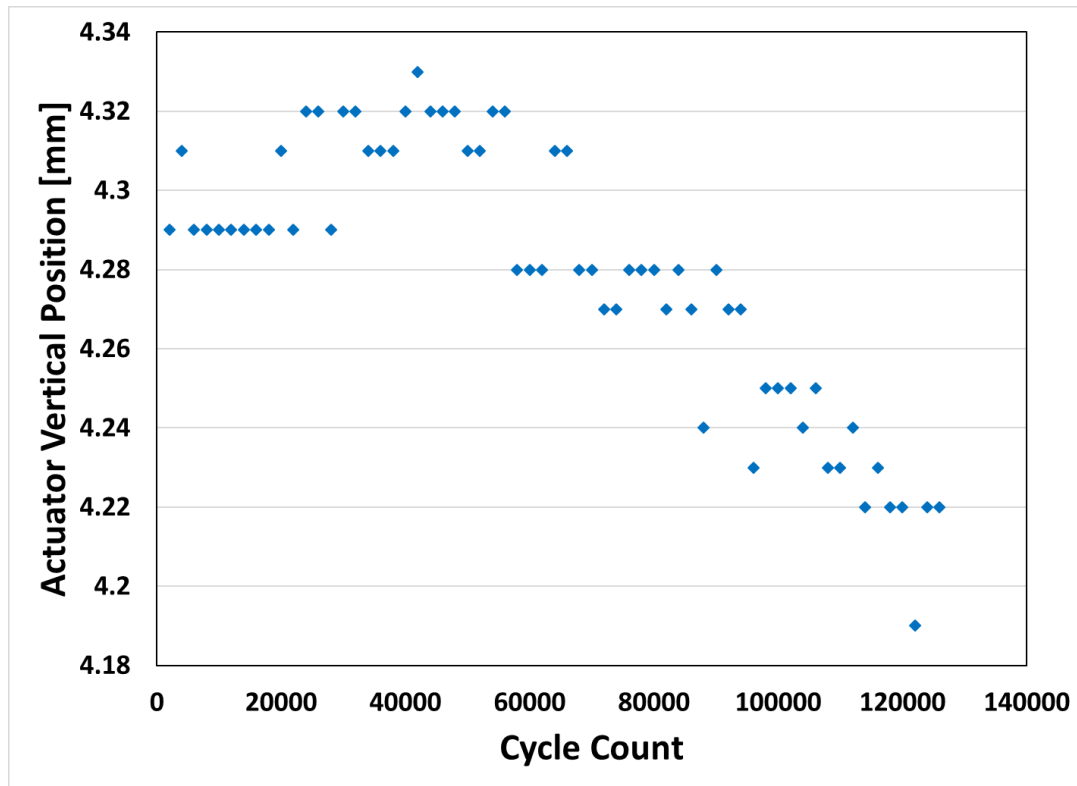


Figure 4-6- Vertical position of lower actuator at the maximum applied load of 1400 N in 2000 cycle intervals. A decrease in the actuator position becomes consistent after 70 000 cycles.

4.4 Discussion

In this study, the fatigue performance of the prototype was quantified at the maximum vertical load of the gait cycle and at a load below the fatigue threshold of 550 MPa. When the prototype was subjected to the maximum axial load of 2600 N, cracks propagated in the high stress areas of the computational model in Chapter 2 at 30k cycles (Figure 4-7). At the decreased compressive load of 1400 N, a consistent decrease in the actuator position occurred at 70k cycles. Although the fatigue life was extended by decreasing the applied force, the fatigue strength of the prototype appears to be less than 550 MPa. However, there is a lack of knowledge of the fatigue performance of small beam structures similar to what was employed in this package design. The fatigue strength of a

material is determined experimentally and dependent on the parameters related to the applied load. For instance, a beam undergoing reversed bending will have a different fatigue strength as when the same part is subjected to unidirectional bending. The previously assumed fatigue strength of 550 MPa may not be applicable. Although the computational and experimental models lack absolute agreement, the patterns and crack locations are useful to know.

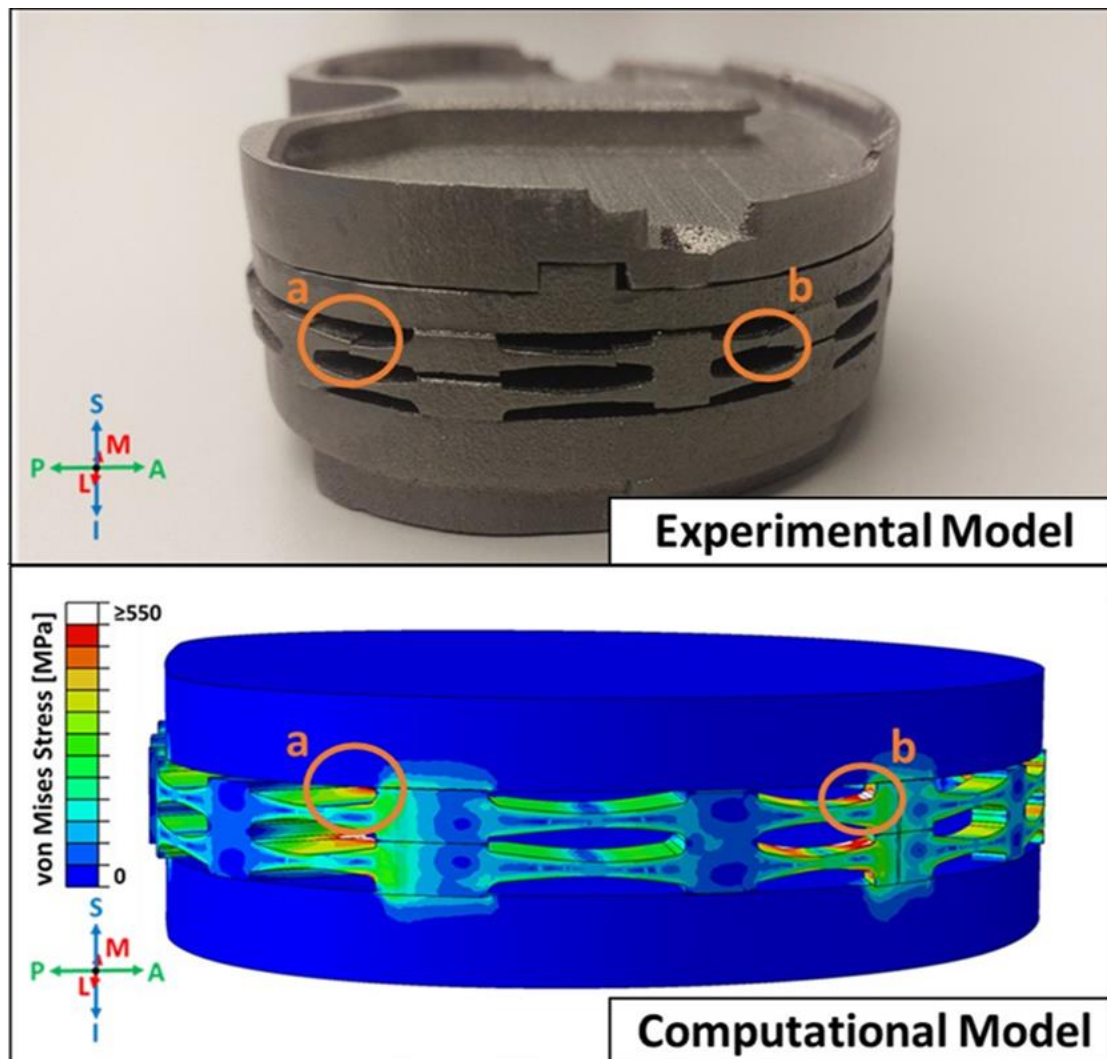


Figure 4-7- Comparison between the Results from Fatigue Testing and the FE Model

In its solid form, Ti6Al4V has a high fatigue strength thereby making it a popular material for implants. However, there can be a decrease in fatigue strength of Ti6Al4V when additively manufactured. The premature failure of the prototype may be attributed to factors inherent to AM Ti6Al4V. The internal porosity, the presence of unfused material, residual stresses, sensitivity to defects and the microstructure can impact the fatigue performance of AM Ti6Al4V (Ghouse et al., 2018; Sterling et al., 2015; Wycisk et al., 2015; Yadollahi and Shamsaei, 2017).

Parameters in the AM process, such as alloy used and scanning parameters, can be optimized to improve the fatigue performance of the prototype. Ghouse et al. compared the fatigue strength differences between commercially-pure titanium (CP-Ti), Ti6Al4V, tantalum (Ta), and TiTa. Ti6Al4V had the lowest fatigue strength: modulus ratio when compared to the other aforementioned alloys. Ta and TiTa had fatigue strength: modulus ratios 8% greater than CP-Ti, and 19% greater than Ti6Al4V (Ghouse et al., 2018). The laser parameters and scanning strategies can be considered for the fatigue strength optimization of Ti6Al4V. Ghouse et al. observed that a low laser power of 50 W increased the fatigue strength of Ti6Al4V by 7% when compared to samples manufactured using a high laser power of 200 W. A contour scan strategy improved the fatigue strength of Ti6Al4V samples by 8% compared to samples manufactured using points or pulsed scanning strategies (Ghouse et al., 2018).

Post processing of the AM Ti6Al4V can increase the fatigue strength. Post-process heat treatment has proven to increase the fatigue strength of Ti6Al4V by eliminating or minimizing the residual stresses and porosity (Edwards and Ramulu, 2014; Nicoletto et al., 2017; Wycisk et al., 2015). However, the temperature, time, and pressure for both annealing and cooling can greatly affect the fatigue strength of the sample. HIP has also shown to eliminate internal voids, homogenize the microstructure and relieving residual stresses thus improving the fatigue strength of AM Ti6Al4V (Kasperovich and Hausmann, 2015; Leuders et al., 2015). In addition to heat treatment, a smooth surface finish, achieved by machining or polishing, can mitigate the detrimental effects of surface

defects that can be sites for stress concentrations, and crack development (Sterling et al., 2015; Yadollahi and Shamsaei, 2017). By considering the alloy used, laser parameters, scanning strategies, surface finish, and heat treatment, the adverse effects of the inherent anisotropic mechanical properties of as-built SLM Ti6Al4V can be mitigated.

Nicoletto et al. were able to achieve fatigue strengths of AM Ti6Al4V that were comparable to its wrought form. By heat treating the specimen at a temperature of 740°C for more than an hour, followed by a period of vacuum cooling at 530°C for an additional hour and cooling to room temperature in argon, and subsequent surface machining had a fatigue strength of 500 MPa at 10^7 cycles (Nicoletto et al., 2017). The heat treatment used by Nicoletto et al. vary from what was used in the fabrication of the current prototype. HIP or a heat treatment procedure employed by Nicoletto et al. can improve the fatigue strength of future package designs. However, depending on the complexity of the geometry being additively manufactured, surface machining may not be feasible thus rendering the structure susceptible to crack initiation from surface defects. Surface machining of the current package design may not be feasible with the thin gaps between the beams.

There are discrepancies between the computational and the experimental model, mainly in the geometry. There were defects in the beams that were not present in the computational model. For instance, some of the beams were distorted from the manufacturing process (Figure 4-8e) and layers may have shifted during printing (Figure 4-9). The defects can introduce stress concentrations and alter the load transmission through the elastic bodies. These differences can introduce stresses in the experimental model that may not be accounted for in the computational model.

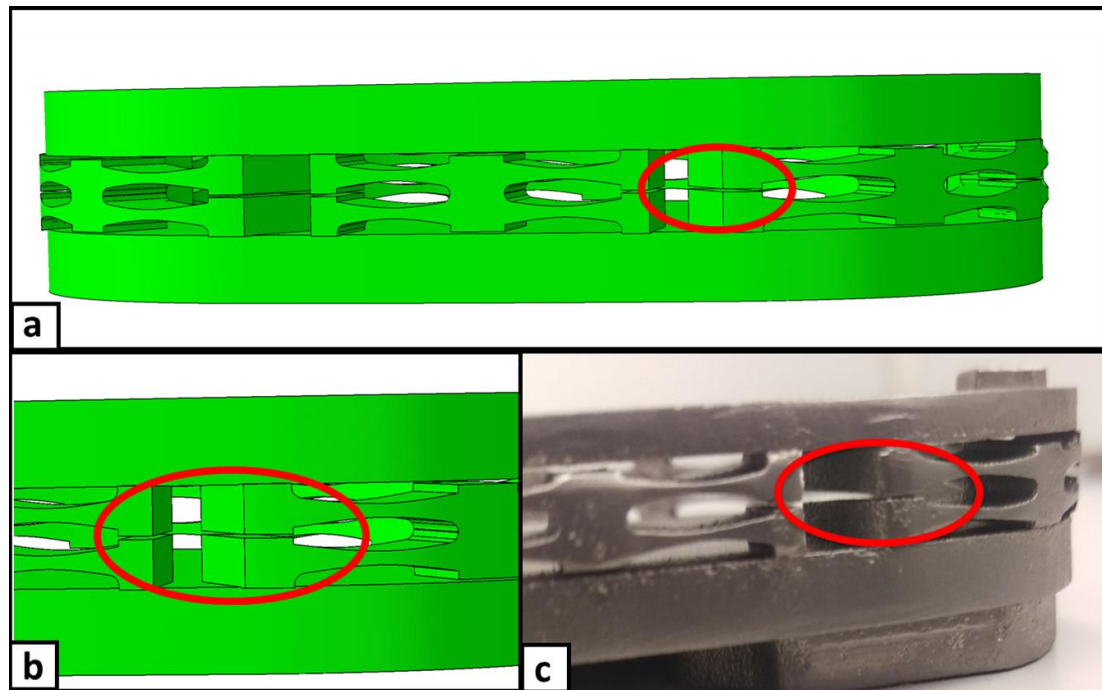


Figure 4-8- Posterior view of the computational model and a prototype that illustrate the distortion that was present in some of the elastic bodies: a) the area of interest is highlighted in the red circle, b) magnified view of computational model, and c) magnified view of prototype.

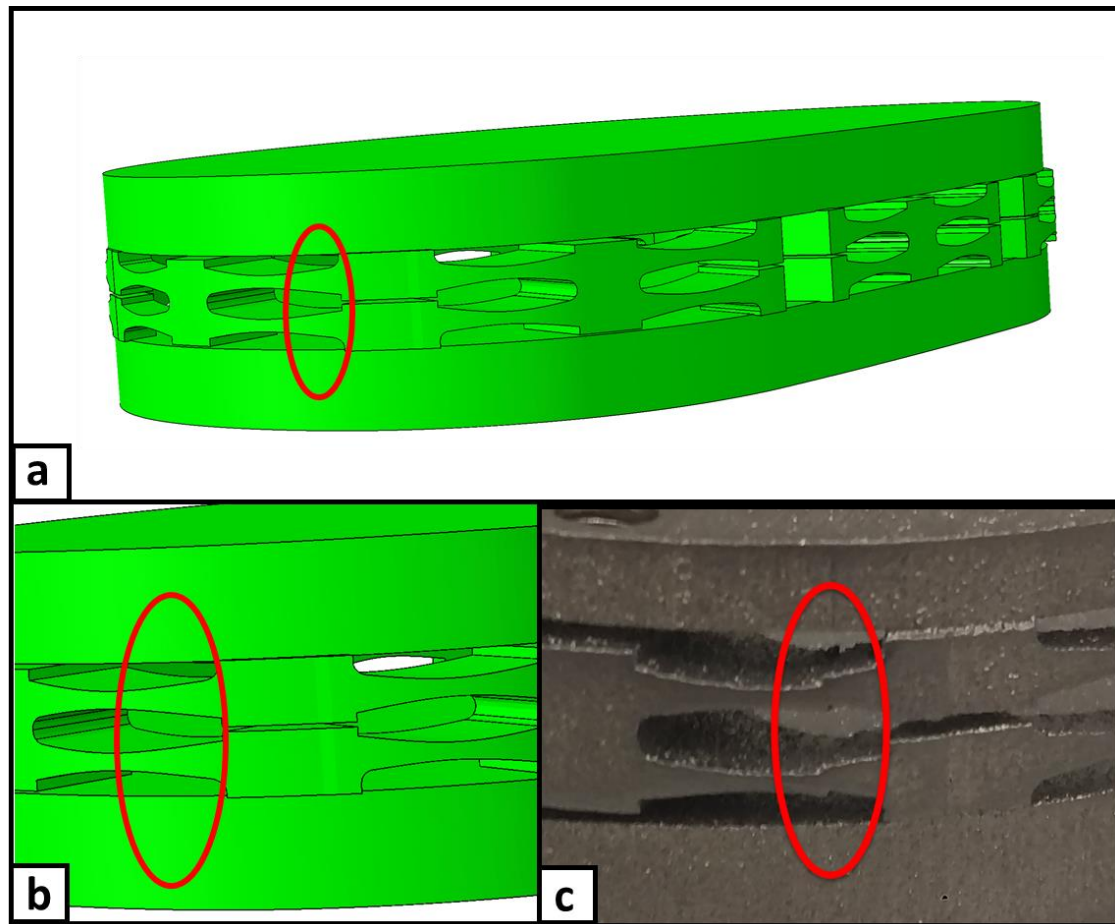


Figure 4-9- Example of a shift in the printing layers: a) posteromedial view of computational model, b) magnified view of computational model, and c) magnified view of prototype.

4.5 Conclusion

The current prototype may not have the fatigue strength to withstand high cycle fatigue ($>10^6$ cycles). However, this can be attributed to the inherent porosity, surface defects, and unfused material in AM Ti6Al4V. There are several factors that can address the microstructure of the material and AM Ti6Al4V's poor notch sensitivity. The choice of alloy, heat treatment, laser parameters, scanning strategies, and surface finish are variables that can be optimized to improve fatigue strength immensely. In this study, the

high stress areas in the computational models corresponded with where cracks were initiated.

4.6 References

- Ahmadi, S.M., Hedayati, R., Li, Y., Lietaert, K., Tümer, N., Fatemi, A., Rans, C.D., Pouran, B., Weinans, H., Zadpoor, A.A., 2018. Fatigue performance of additively manufactured meta-biomaterials: The effects of topology and material type. *Acta Biomater.* 65, 292–304. <https://doi.org/10.1016/j.actbio.2017.11.014>
- Baufeld, B., Brandl, E., Van Der Biest, O., 2011. Wire based additive layer manufacturing: Comparison of microstructure and mechanical properties of Ti-6Al-4V components fabricated by laser-beam deposition and shaped metal deposition. *J. Mater. Process. Technol.* 211, 1146–1158. <https://doi.org/10.1016/j.jmatprotec.2011.01.018>
- Brandl, E., Baufeld, B., Leyens, C., Gault, R., 2010. Additive manufactured Ti-6Al-4V using welding wire: Comparison of laser and arc beam deposition and evaluation with respect to aerospace material specifications, in: *Physics Procedia*. Elsevier B.V., pp. 595–606. <https://doi.org/10.1016/j.phpro.2010.08.087>
- Chan, K.S., Koike, M., Mason, R.L., Okabe, T., 2013. Fatigue life of titanium alloys fabricated by additive layer manufacturing techniques for dental implants. *Metall. Mater. Trans. A Phys. Metall. Mater. Sci.* 44, 1010–1022. <https://doi.org/10.1007/s11661-012-1470-4>
- Edwards, P., Ramulu, M., 2014. Fatigue performance evaluation of selective laser melted Ti-6Al-4V. *Mater. Sci. Eng. A* 598, 327–337. <https://doi.org/10.1016/j.msea.2014.01.041>
- Facchini, L., Magalini, E., Robotti, P., Molinari, A., Höges, S., Wissenbach, K., 2010. Ductility of a Ti-6Al-4V alloy produced by selective laser melting of prealloyed powders. *Rapid Prototyp. J.* 16, 450–459. <https://doi.org/10.1108/13552541011083371>
- Ghose, S., Babu, S., Nai, K., Hooper, P.A., Jeffers, J.R.T., 2018. The influence of laser parameters, scanning strategies and material on the fatigue strength of a stochastic porous structure. *Addit. Manuf.* 22, 290–301.

<https://doi.org/10.1016/J.ADDMA.2018.05.024>

- Harrysson, O.L.A., Cansizoglu, O., Marcellin-Little, D.J., Cormier, D.R., West, H.A., 2008. Direct metal fabrication of titanium implants with tailored materials and mechanical properties using electron beam melting technology. *Mater. Sci. Eng. C* 28, 366–373. <https://doi.org/10.1016/j.msec.2007.04.022>
- Hrabe, N.W., Heintl, P., Flinn, B., Körner, C., Bordia, R.K., 2011. Compression-compression fatigue of selective electron beam melted cellular titanium (Ti-6Al-4V). *J. Biomed. Mater. Res. Part B Appl. Biomater.* 99B, 313–320. <https://doi.org/10.1002/jbm.b.31901>
- ISO, 2009. ISO 14243-1, Implants for surgery - Wear of total knee-joint prostheses.
- Kasperovich, G., Hausmann, J., 2015. Improvement of fatigue resistance and ductility of TiAl6V4 processed by selective laser melting. *J. Mater. Process. Technol.* 220, 202–214. <https://doi.org/10.1016/j.jmatprotec.2015.01.025>
- Koike, M., Greer, P., Owen, K., Lilly, G., Murr, L.E., Gaytan, S.M., Martinez, E., Okabe, T., 2011. Evaluation of Titanium Alloys Fabricated Using Rapid Prototyping Technologies—Electron Beam Melting and Laser Beam Melting. *Materials (Basel)*. 4, 1776–1792. <https://doi.org/10.3390/ma4101776>
- Leuders, S., Thöne, M., Riemer, A., Niendorf, T., Tröster, T., Richard, H.A., Maier, H.J., 2013. On the mechanical behaviour of titanium alloy TiAl6V4 manufactured by selective laser melting: Fatigue resistance and crack growth performance. *Int. J. Fatigue* 48, 300–307. <https://doi.org/10.1016/j.ijfatigue.2012.11.011>
- Leuders, S., Vollmer, M., Brenne, F., Tröster, T., Niendorf, T., 2015. Fatigue Strength Prediction for Titanium Alloy TiAl6V4 Manufactured by Selective Laser Melting. *Metall. Mater. Trans. A Phys. Metall. Mater. Sci.* 46, 3816–3823. <https://doi.org/10.1007/s11661-015-2864-x>
- Murr, L.E., Esquivel, E. V., Quinones, S.A., Gaytan, S.M., Lopez, M.I., Martinez, E.Y., Medina, F., Hernandez, D.H., Martinez, E., Martinez, J.L., Stafford, S.W., Brown,

- D.K., Hoppe, T., Meyers, W., Lindhe, U., Wicker, R.B., 2009. Microstructures and mechanical properties of electron beam-rapid manufactured Ti-6Al-4V biomedical prototypes compared to wrought Ti-6Al-4V. *Mater. Charact.* 60, 96–105.
<https://doi.org/10.1016/j.matchar.2008.07.006>
- Nicoletto, G., Maisano, S., Antolotti, M., Dall’aglio, F., 2017. Influence of post fabrication heat treatments on the fatigue behavior of Ti-6Al-4V produced by selective laser melting, in: *Procedia Structural Integrity*. Elsevier B.V., pp. 133–140.
<https://doi.org/10.1016/j.prostr.2017.11.070>
- Qiu, C., Adkins, N.J.E., Attallah, M.M., 2013. Microstructure and tensile properties of selectively laser-melted and of HIPed laser-melted Ti-6Al-4V. *Mater. Sci. Eng. A* 578, 230–239. <https://doi.org/10.1016/j.msea.2013.04.099>
- Shiomi, M., Osakada, K., Nakamura, K., Yamashita, T., Abe, F., 2004. Residual stress within metallic model made by selective laser melting process. *CIRP Ann. - Manuf. Technol.* 53, 195–198. [https://doi.org/10.1016/S0007-8506\(07\)60677-5](https://doi.org/10.1016/S0007-8506(07)60677-5)
- Sterling, A., Shamsaei, N., Torries, B., Thompson, S.M., 2015. Fatigue Behaviour of Additively Manufactured Ti-6Al-4 v. *Procedia Eng.* 133, 576–589.
<https://doi.org/10.1016/j.proeng.2015.12.632>
- Wycisk, E., Siddique, S., Herzog, D., Walther, F., Emmelmann, C., 2015. Fatigue performance of laser additive manufactured Ti-6Al-4V in very high cycle fatigue regime up to 10^9 cycles. *Front. Mater.* 2. <https://doi.org/10.3389/fmats.2015.00072>
- Yadollahi, A., Shamsaei, N., 2017. Additive manufacturing of fatigue resistant materials: Challenges and opportunities. *Int. J. Fatigue* 98, 14–31.
<https://doi.org/10.1016/j.ijfatigue.2017.01.001>

Chapter 5

5 Sensitivity Analysis of Polyethylene Thickness and the Effect of Physiological Loading Assumptions

Overview: *In the operating room, the TKR components used are modular in design to ensure correct sizing, and joint stability. With this in mind, the influence of different implant sizes on the mechanical behaviour of the package should be considered. This chapter quantifies the package's sensitivity to PE insert thickness. In addition to considerations behind PE insert thickness, the assumption that the tibiofemoral forces in the gait cycle can be accurately approximated with a vertical compression loading scenario will be examined.*

5.1 Introduction

Implant sizing is an important factor that is considered to ensure stability of a TKR procedure. Different PE bearing thicknesses need to be considered to restore the joint line and equalizing the extension and flexion gaps. If the proximal tibia was excessively resected during the TKR procedure, which affects the flexion and extension gaps, a thicker PE bearing can restore the joint line (Abdel and Haas, 2014). Therefore, the package's mechanical behaviour and stress from physiological loading should not be adversely affected by the PE bearing thickness deemed suitable by the surgeon.

In the previous studies in this thesis, it was assumed that the consideration of the vertical load of the gait cycle would be sufficient for analyzing the stresses and mechanical behaviour of the package design. This was assumed because the vertical component contributes the largest proportion of force relative to the other components in the gait cycle. This assumption overlooks the significance of the other components of loading thus overlooking how they affect the stresses in the package. Simulations or experiments that only consider vertical loading may underestimate the stresses an instrumented implant would actually be subjected to under physiological loading.

In this chapter, computational modeling was performed to elucidate the effects PE bearing thickness and multiaxial loading have on the current package design. The effect of the PE bearing thickness on the mechanical behaviour in the package were quantified. In other words, the changes in the stresses and displacements in the package were calculated when the PE bearing thickness was altered during loading. Furthermore, considering that the vertical component is the largest contributor to the resultant force in gait, the viability of assuming a vertical compression loading scenario is representative of a loading scenario that considers all load components was examined.

5.2 Materials and Methods

Finite element analysis was conducted using Abaqus. A defeatured version of the prototype was used for analysis. Simulations with loads based on Orthoload were applied to the model (Bergmann et al., 2014). A rigidly connected reference point was defined inferiorly to the bottom surface of the package. An Encastre boundary condition fully restrained this reference point. The thickness of the lowest points of a 9 mm and 11 mm size 7 Stryker Triathlon Cruciate Retaining (CR) UHMWPE bearing were measured for the purpose of determining the position of the reference point where loads were resolved in the computational model to replicate the coordinate system used in (Kutzner et al., 2010). The Ti6Al4V package had the following material properties $E = 130\,000$ MPa (Renishaw plc, 2017) and $\nu = 0.31$ (AZoMaterials, n.d.). The package was meshed with a global mesh size of 1 mm. Tetrahedral elements were used to mesh the part. For all simulations, a self-contact interaction, nonlinear effects of large deformations and displacements were defined.

The Orthoload dataset for AVER75 in the gait cycle was used in the analyses (Bergmann et al., 2014). All six components of force were applied to models simulating a 9 mm and 11 mm thick PE bearing in 1% gait cycle intervals. In two separate models that replicate a 9 mm and 11 mm PE bearing, the maximum vertical load in AVER75 of 1960 N was applied in 0.01 step increments. Stresses and displacements were analyzed to quantify the differences when the shear forces, moments, and the PE insert thickness are considered.

5.3 Results

5.3.1 Axial Force Only versus Six Component Loading

The deflection and stress were different between the two loading scenarios. The six component loading scenario had a larger peak stress than the uniaxial compressive scenario (851 MPa and 733 MPa, respectively). Although, the peak stresses occurred at 48% in the gait cycle, or at the time maximum loads were applied to the package.

Throughout the stance phase, the stress was greater in the six component loading than the vertical loading scenario (Figure 5-1).

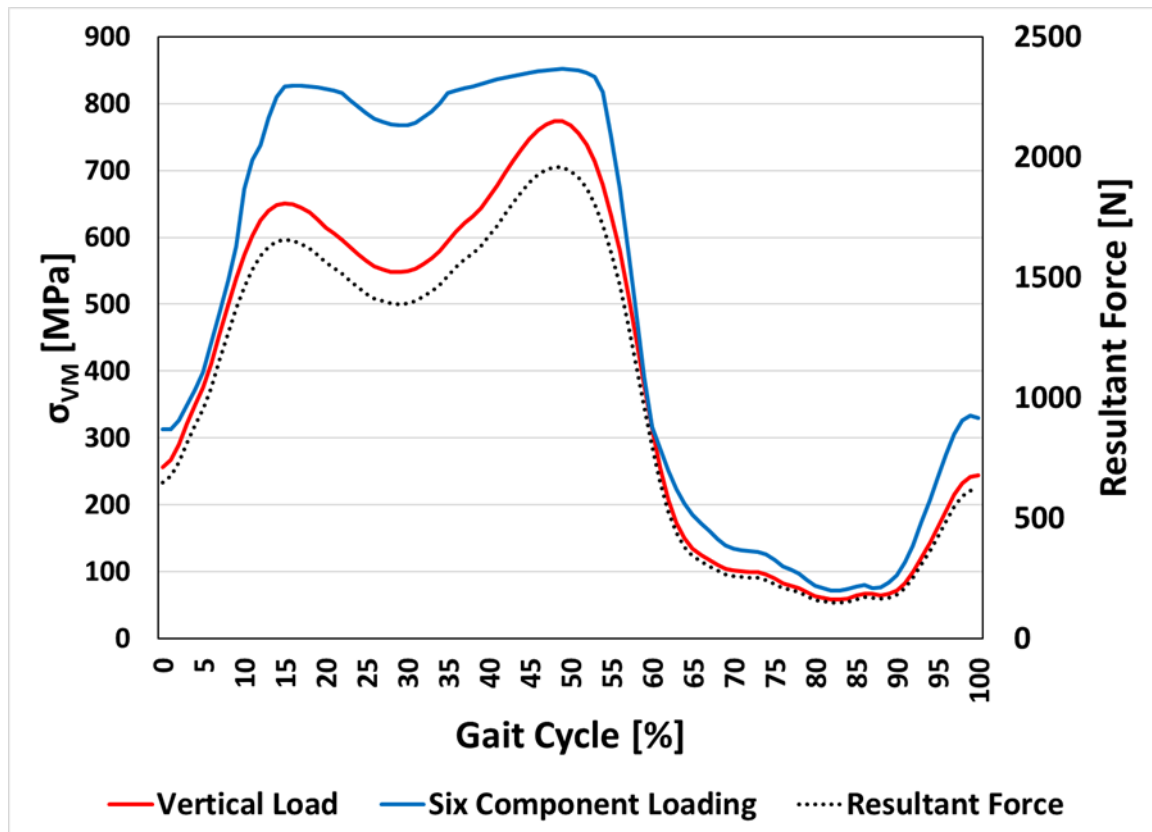


Figure 5-1- Comparison between uniaxial compressive loading and six component loading. Peak stresses occurred at 48% gait cycle for both loading scenarios. There was a 15% difference between load scenarios where the six component loading scenario was greatest.

When all six components were simulated, the superimposed shear forces created an asymmetrical stress and deflection response. The greatest stress and maximum deflection were located at the anterolateral portion of the package (Figure 5-2). The maximum deflection, under simulated gait, was 0.22 mm (Figure 5-3).

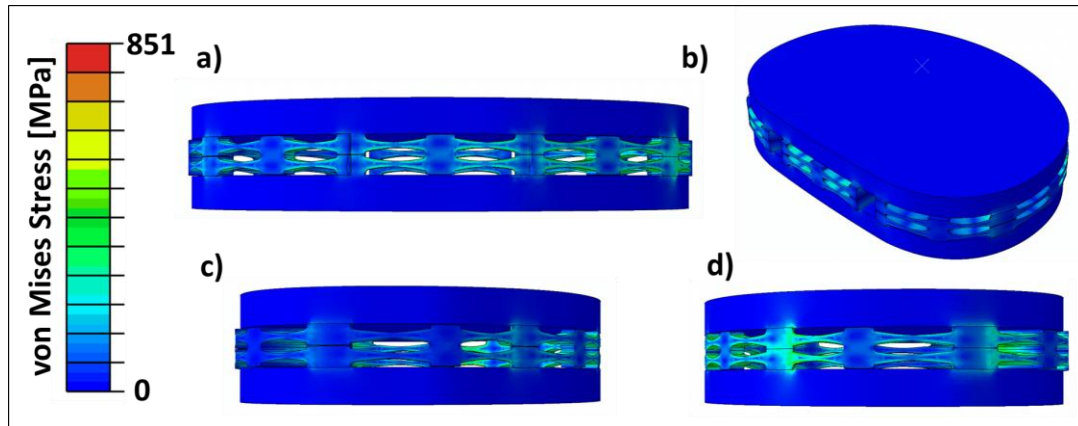


Figure 5-2-Stress Plot of Maximum Six Component Loading: a) anterior, b) isometric, c) medial, d) lateral

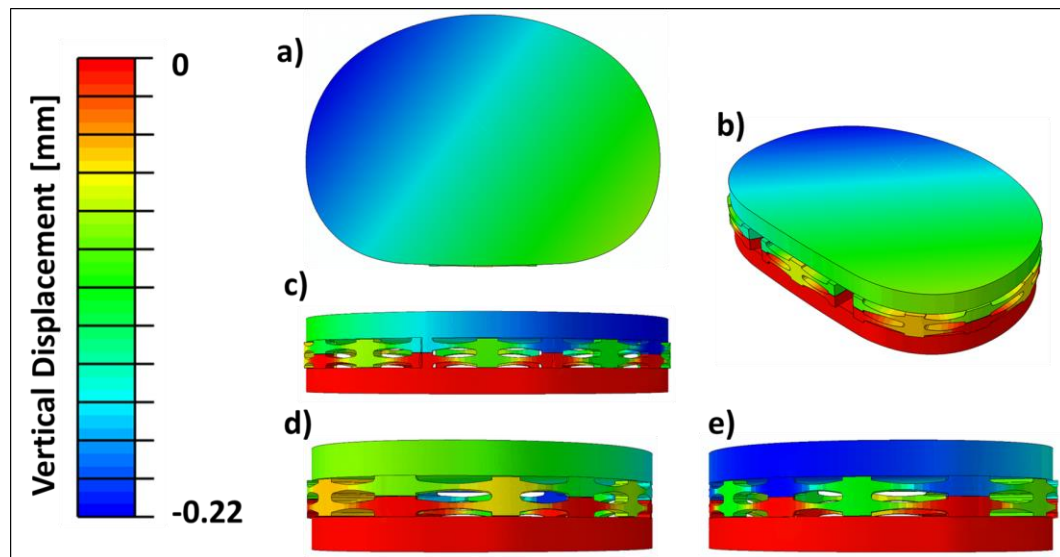


Figure 5-3- Vertical Displacement Plot of Maximum Six Component Loading: a) superior, b) isometric, c) anterior, d) medial, e) lateral

Under the loading scenario where only the vertical force was considered, the maximum deflection was 0.23 mm in the anterior aspect of the package (Figure 5-4 and Figure 5-5). Due to the symmetry of the package and the location of where the load was applied, the peak stresses were located in the anteromedial and anterolateral regions of the package.

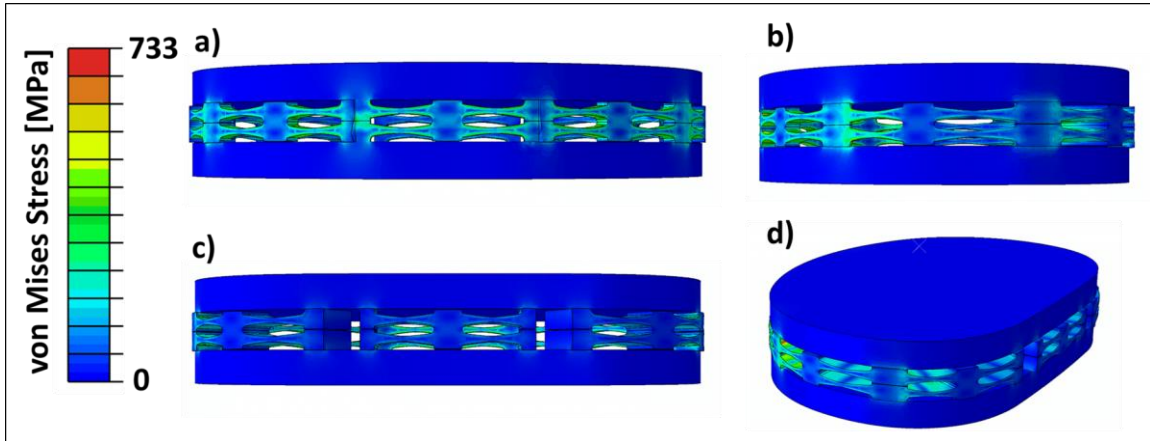


Figure 5-4- Stress Plot of Maximum Vertical Load: a) anterior, b) lateral, c) posterior, d) isometric

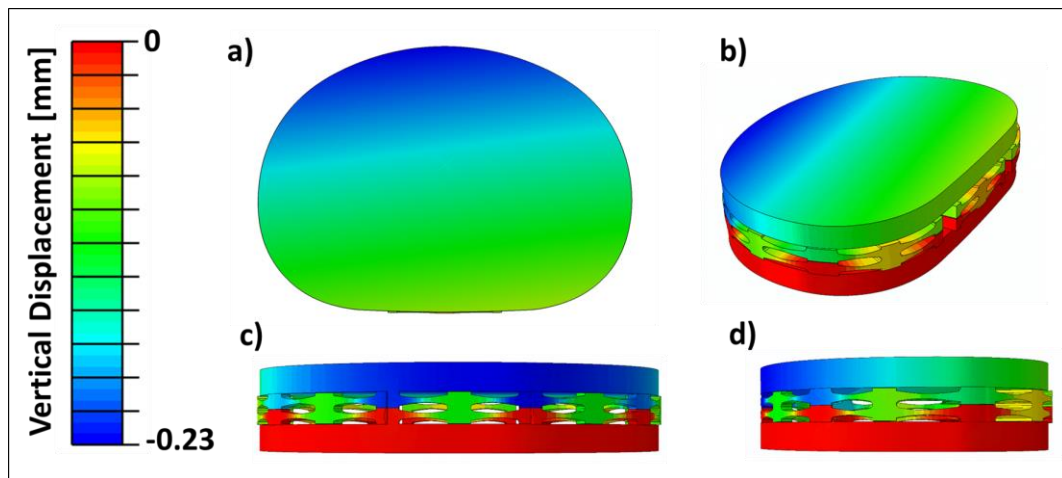


Figure 5-5- Vertical Displacement Plot of Maximum Vertical Fz: a) superior, b) isometric, c) anterior, d) lateral

5.3.2 Effect of Polyethylene Insert Thickness

There was little difference in the stresses and displacements between the models with 9 mm and 11 mm PE thicknesses. In the simulations with only a vertical load applied, the maximum stress was 733 MPa, and the shear displacements of the top plate's bottom surface did not exceed 10 μm . The largest magnitudes in displacements and stresses were located in the anterior portion of the package.

The mechanical behaviour in the gait cycle simulations were very similar (Figure 5-6). The largest stress and displacements were located in the anterolateral region of the package. The peak stress was 851 MPa. The percent difference between the peak stress in the 9 mm and 11 mm bearing simulations was 0.02%. The shear displacement, along the mediolateral axis, ranged from 3 to 5 μm directed in the lateral direction where the largest displacement was in the posterior section of the top plate. Along the anteroposterior axis, the shear displacements were greatest in the lateral part of the top plate (about 6 μm) and decreased towards the medial direction to a minimum of about 2 μm .

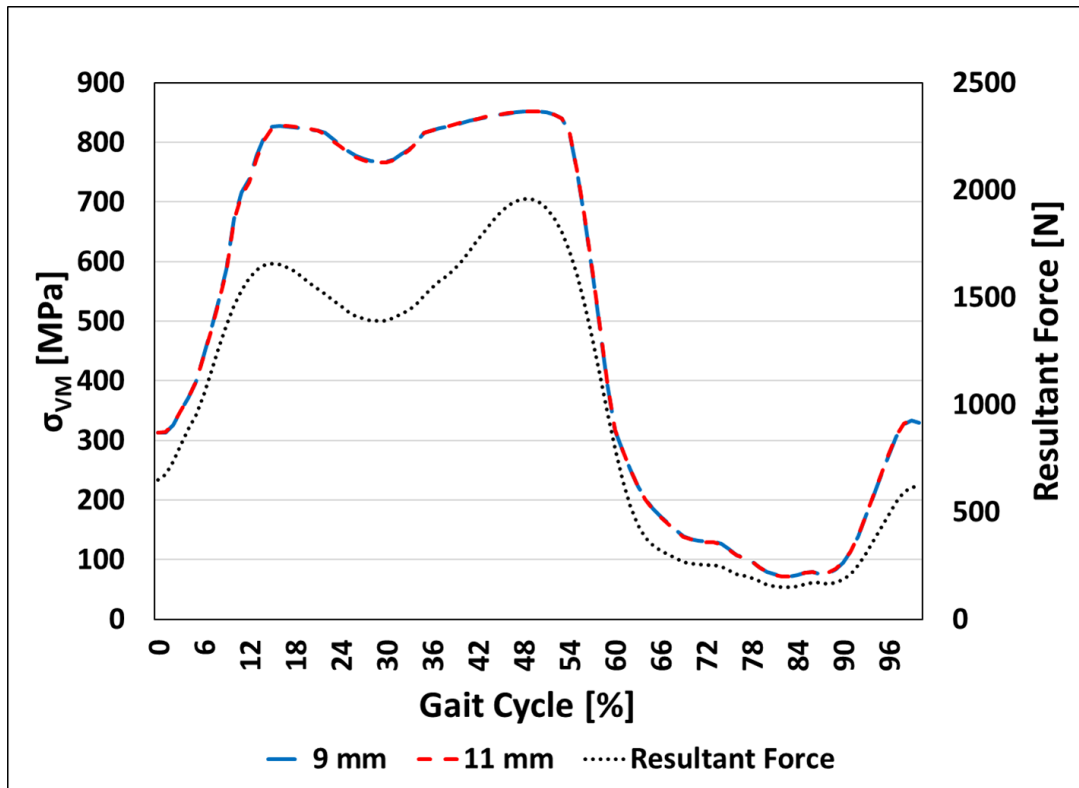


Figure 5-6- Comparison of the maximum von Mises stresses calculated in six component loading between a 9 mm and 11 mm PE bearing.

5.4 Discussion

In this chapter, the package design was not sensitive to the effects of changing the PE bearing thickness— there was little difference in the stress and deflection response between the 9 mm and 11 mm thick PE bearings. When considering all force and moment components in gait, the calculated stresses were greater throughout the stance phase compared to when the vertical component was considered. The effects of the shear forces and moments appear to have a significant effect on the stresses in the package design.

The stress distribution and displacements in this chapter are different in the computational model presented in Chapter 2. In Chapter 2, the load was applied to a reference point offset from the sagittal plane to achieve a medial bias and positioned more posteriorly than the one used in this chapter. Additionally, the forces were derived

from the tibial forces presented by Bergmann et al (Bergmann et al., 2014). The computational models simulate the loading scenario used by Bergmann et al. since the design of this package would require the use of a PS or CS TKR system, and the *in vivo* measurements gathered by Bergmann et al. serves as a more accurate representation of the forces transmitted in the knee.

The TKR components were excluded from the simulations in order to simplify the analyses. The main objective of this study was to quantify the mechanical behaviour of the package design under physiological loading. Therefore, the consideration of the contact mechanics of the articulating surfaces, and stresses in the interlocking mechanism were omitted due to the increased complexity these factors would introduce. Future work can investigate how the presence of the package may affect the interfacing TKR components.

When comparing the effect of PE insert thickness on the mechanical behaviour of the package, there was no difference observed. The stresses and displacements of the computational model are not sensitive to a 2 mm difference in thickness. The use of a thicker PE insert, thicker than the ones used in these analyses, may not reproduce the same trend. It can be hypothesized that a thicker PE insert will magnify the effects of the shear forces due to the increased moment arm. However, because the computational model simulates a linear-elastic model, peak stresses in thicker PE bearings are proportional to the change in the PE bearing thickness. Considering the thickness of the current package design, the use of a PE insert thicker than 11 mm is highly unlikely because of the amount of the proximal tibia required to be resected.

Although the vertical component in gait has the largest contribution to the resultant force, the exclusion of the shear forces and moments may not be advisable. The asymmetrical load distribution, due to the shear forces and moments associated with gait, resulted in localized increases in stress and displacements. Dismissing all the load components, aside from the vertical component, can produce results that may not be representative of what would occur in reality.

Future iterations should increase the stiffness of the anterior region of the package. Based on the location of the coordinate system used in (Bergmann et al., 2014), the magnitude of the load transmitted through the anterior region of the package was greater than expected in the design process using the loads from ISO 14243. The increased load thereby increases the stresses and the likelihood of premature failure.

5.5 Conclusion

In this chapter, the sensitivity of the mechanical response of the package was determined between computational models that compared the effect of different PE insert thicknesses and quantified the differences in the stresses and displacements between a simplified simulation where only the vertical component of gait was considered versus a simulation with all six load components in gait were considered. The increase in PE insert thickness did not change the mechanical behaviour of the package. However, this cannot be said when comparing the two loading scenarios. Applying only the vertical force to the package did not result in an accurate approximation of the physiological loading in gait despite the vertical component having the largest magnitude relative to the other components.

5.6 References

Abdel, M.P., Haas, S.B., 2014. The unstable knee: Wobble and Buckle. *Bone Jt. J.* 96B, 112–114. <https://doi.org/10.1302/0301-620X.96B11.34325>

AZoMaterials, n.d. Properties: Titanium Alloys - Ti6Al4V Grade 5 [WWW Document]. URL <https://www.azom.com/properties.aspx?ArticleID=1547> (accessed 11.4.19).

Bergmann, G., Bender, A., Graichen, F., Dymke, J., Rohlmann, A., Trepczynski, A., Heller, M.O., Kutzner, I., 2014. Standardized Loads Acting in Knee Implants. *PLoS One* 9, 86035. <https://doi.org/10.1371/journal.pone.0086035>

Kutzner, I., Heinlein, B., Graichen, F., Bender, A., Rohlmann, A., Halder, A., Beier, A., Bergmann, G., 2010. Loading of the knee joint during activities of daily living measured in vivo in five subjects. <https://doi.org/10.1016/j.jbiomech.2010.03.046>

Renishaw plc, 2017. Ti6Al4V ELI-0406 powder for additive manufacturing [WWW Document]. URL <https://resources.renishaw.com/en/details/data-sheet-ti6al4v-eli-0406-powder-for-additive-manufacturing--94700>

Chapter 6

6 General Discussion and Conclusion

Overview: *This chapter summarizes the conclusions made to address the research objectives presented in Chapter 1. The strengths and limitations of the current thesis work are discussed. Future directions in the improvement and development of an energy harvesting load sensor for the use of measuring tibiofemoral forces are outlined. Lastly, the significance of the current work is highlighted.*

6.1 Summary

This present work presents a novel method in measuring *in vivo* tibial forces by using a 3D printed package designed to house load sensing and energy harvesting elements in between the PE insert and tibial tray. This eliminates the need to alter existing TKR components. Instead, the package can be designed to be compatible with commercially available TKR components. The stacked beam structure of the elastic bodies placed along the periphery of the package has shown to provide the deflection response required for the TEGs to operate from gait loading.

In Chapter 2, the iterative design process of a package was outlined. The parameters of the stacked beam structures were tuned to provide the desired force-displacement relationship when subjected to loads associated with the gait cycle. The design of the package was also designed to resist shear forces that could damage the embedded TEGs. The package design was also tuned to minimize the stresses when the maximum vertical load in gait was applied.

In Chapter 3, it was noted that the package prototype was more compliant than what was expected based on computational models. However, experiments demonstrated that the package prototype was capable of deflecting accordingly to the cyclic abduction/adduction applied to the package. In other words, the package, in conjunction with embedded load sensors, is capable of measuring coronal imbalances. Interpositional

load sensing devices, such as this package design, can measure the compartmental loads transmitted through a TKR.

Chapter 4 outlines the fatigue performance of the current prototype. Unfortunately, despite the capabilities of manufacturing complex geometries from SLM, the package prototype did not have the durability to prove that it can withstand years of use. The internal porosity and the defect sensitivity of SLM Ti6Al4V are notable reasons for the prototype's poor fatigue strength. However, the fatigue strength of SLM Ti6Al4V can be improved to address the inherent obstacles with SLM Ti6Al4V. HIP has been shown to improve the microstructure and density and machining the surfaces of parts can eliminate surface defects.

In Chapter 5, from the computational models, the package is not sensitive to the PE insert thickness. So, this package design can most likely be used with varying PE insert thicknesses to ensure joint line restoration and equalized extension and flexion gaps. It was also deduced that applying a cyclic sinusoidal vertical load is not an accurate representation of a loading scenario where all six load components are considered. The package sustained higher stresses when all components of loading were considered in the analyses.

6.2 Strengths and Limitations

Additive manufacturing was used to create a prototype with a complex geometry. Despite the ability to manufacture parts that are not feasible with subtractive manufacturing techniques, there were some limitations associated with AM Ti6Al4V. Manufacturing errors were present in the prototypes such as distorted beams and shifts in print layers. AM Ti6Al4V is also notorious for its internal porosity, unfused material, and poor defect sensitivity. This may explain the large stiffness discrepancy between the computational and experimental models and low fatigue life.

The prototypes were subjected to vertical loading. It is expected that the other forces and moments in gait will have an effect on the mechanical behaviour and stress of the

prototype. To address this shortcoming, computational models were developed to determine how a six-component loading differs from a loading scenario where only the vertical force was considered. Also, the vertical load is the largest force component in gait. With this in mind, the TEGs were designed to operate primarily from the vertical deflection resulting from vertical loading.

Gait was the only ADL that was considered in the initial package design. Although other ADL considered, the loads applied to the package correspond to ISO 14243. ISO 14243 is an established standard that is used for the durability testing of knee prostheses.

The triboelectric effect is an energy harvesting mechanism that has not been harnessed for measuring the tibiofemoral forces in knee implants. The TEGs can be used to generate usable electricity and measuring forces. However, there are limitations to this concept. The durability of the TEGs still needs to be investigated. The use of TEGs requires motion to operate optimally, but TKR designs have been developed to eliminate motion. Motion between components and within components can accelerate wear and lead to implant failure. TEGs may have a nonlinear relationship between the applied force and the measured voltage. The TEG's reliance on the frequency of the contact and separation can mean the TEGs are not usable for measuring static loads. Despite the drawbacks of using TEGs in knee implants, there are some aspects that are beneficial. The use of TEGs can be a solution for powering other load sensors which has been the main obstacle behind the development of instrumented implants. If a self-contained, self-powering load sensing device can be successfully developed, the measurement of tibiofemoral loads will no longer be limited to a laboratory setting.

6.3 Future Directions

The package was designed to be integrated with the TEGs. With the complete triboelectric energy harvester assembly, the energy harvester's ability to generate usable electricity, accurately measure loads, and transmit load data wirelessly still needs to be investigated.

The package can undergo further iterations. The overall thickness of the package can be reduced so that more bone can be preserved in TKR. Other elastic body geometries may yield the desired design responses while decreasing the thickness of the package. Despite the elastic body geometry used, the package requires sealing with perhaps a hyperelastic biocompatible material to isolate the TEGs and the electronics from foreign biological substances.

The fatigue performance of the package was identified to be problematic. Parameters, related to AM Ti6Al4V, such as laser power, scanning strategy, alloy, heat treatment, and surface finish can be optimized to maximize the fatigue strength of the package.

6.4 Significance

This current thesis work presents a novel concept of leveraging the triboelectric effect for measuring tibiofemoral forces. The design process of creating an interpositional, compliant component can be translated to other energy harvesting components and TKR systems. Through experimental testing, the mechanical behaviour and fatigue life of AM Ti6Al4V are better understood in applications that require large deflections. The use of energy harvesting devices may serve as another approach in better understanding *in vivo* knee mechanics. Such devices can be beneficial in monitoring patient activities postoperatively, the refinement of surgical procedures and the improvement of current implant designs.

Appendices

Appendix A- Analytical Model Calculations

E=	130,000 MPa
F-tot=	2600 N
delta=	0.1 mm
Perimeter	235 mm

s=	0 mm
w=	2 mm

L	I (based on V equation)	F/beam	F_total (8 beam config)	b=											
				1	2	3	4	5	6	7	8	9	10	11	12
1	7.0922E-05	55.31915	442.55	0.094766	0.075216	0.065707	0.059699	0.05542	0.052152	0.04954	0.047383	0.045559	0.043987	0.042611	0.041393
2	0.001134752	66.38298	531.06	0.238796	0.189533	0.165572	0.150432	0.139649	0.131415	0.124833	0.119398	0.114801	0.110839	0.107373	0.104304
3	0.005744681	77.44681	619.57	0.41003	0.325441	0.284299	0.258303	0.239787	0.225648	0.214346	0.205015	0.197122	0.190319	0.184368	0.179097
4	0.018156028	88.51064	708.09	0.601729	0.477592	0.417215	0.379065	0.351893	0.331144	0.314558	0.300864	0.289281	0.279298	0.270564	0.262829
5	0.044326241	99.57447	796.60	0.810241	0.643088	0.56179	0.51042	0.473832	0.445893	0.42356	0.40512	0.389523	0.37608	0.36432	0.353905
6	0.091914894	110.6383	885.11	1.033211	0.82006	0.716389	0.650882	0.604225	0.568598	0.540119	0.516606	0.496716	0.479574	0.464577	0.451296
7	0.170283688	121.7021	973.62	1.26897	1.007182	0.879855	0.799401	0.742098	0.698341	0.663364	0.634485	0.610057	0.589004	0.570585	0.554274
8	0.290496454	132.766	1062.13	1.516261	1.203457	1.051317	0.955185	0.886715	0.834431	0.792638	0.758131	0.728942	0.703786	0.681778	0.662288
9	0.465319149	143.8298	1150.64	1.774097	1.408102	1.23009	1.117611	1.037498	0.976323	0.927423	0.887049	0.852897	0.823463	0.797713	0.774908
10	0.709219858	154.8936	1239.15	2.041679	1.620481	1.415621	1.286177	1.193981	1.123579	1.067304	1.020839	0.981537	0.947663	0.918029	0.891785
11	1.038368794	165.9574	1327.66	2.318343	1.84007	1.607449	1.460464	1.355775	1.275833	1.211932	1.159171	1.114543	1.076079	1.04243	1.012629
12	1.470638298	177.0213	1416.17	2.603529	2.066422	1.805186	1.64012	1.522553	1.432777	1.361015	1.301764	1.251646	1.208451	1.170662	1.137196
13	2.025602837	188.0851	1504.68	2.896756	2.299156	2.008498	1.824842	1.694033	1.594146	1.514302	1.448378	1.392615	1.344555	1.30251	1.265275
14	2.724539007	199.1489	1593.19	3.197605	2.53794	2.217095	2.014365	1.869971	1.75971	1.671573	1.598802	1.537248	1.484197	1.437785	1.396682
15	3.590425532	210.2128	1681.70	3.505708	2.782482	2.430722	2.208458	2.05015	1.929265	1.832637	1.752854	1.685369	1.627205	1.576322	1.531259
16	4.647943262	221.2766	1770.21	3.820739	3.032522	2.649152	2.406915	2.234382	2.102634	1.997322	1.910369	1.83682	1.77343	1.717973	1.668861
17	5.923475177	232.3404	1858.72	4.142405	3.287829	2.872184	2.609552	2.422493	2.279654	2.165475	2.071203	1.991461	1.922734	1.862609	1.809362
18	7.445106383	243.4043	1947.23	4.470445	3.548194	3.099633	2.816204	2.614332	2.46018	2.33696	2.235222	2.149166	2.074997	2.01011	1.952647
19	9.242624113	254.4681	2035.74	4.804618	3.813428	3.331336	3.02672	2.809758	2.644083	2.511652	2.402309	2.309819	2.230106	2.160369	2.09861
20	11.34751773	265.5319	2124.26	5.144708	4.083357	3.567141	3.240963	3.008643	2.831242	2.689437	2.572354	2.473317	2.387962	2.313289	2.247158
21	13.79297872	276.5957	2212.77	5.490515	4.357825	3.806911	3.458808	3.210873	3.021547	2.870211	2.745258	2.639564	2.548471	2.468779	2.398203
22	16.61390071	287.6596	2301.28	5.841857	4.636685	4.050518	3.68014	3.416339	3.214898	3.053877	2.920929	2.808472	2.71155	2.626758	2.551666
23	19.84687943	298.7234	2389.79	6.198565	4.919804	4.297845	3.904851	3.624943	3.411202	3.240349	3.099282	2.979959	2.877119	2.787149	2.707473
24	23.53021277	309.7872	2478.30	6.560481	5.207057	4.548784	4.132844	3.836593	3.610372	3.429544	3.280241	3.15395	3.045106	2.949883	2.865554
25	27.70390071	320.8511	2566.81	6.92746	5.498329	4.803233	4.364027	4.051203	3.812328	3.621385	3.46373	3.330376	3.215442	3.114893	3.025847
26	32.40964539	331.9149	2655.32	7.299367	5.793511	5.061098	4.598313	4.268695	4.016996	3.815802	3.649683	3.509169	3.388066	3.282119	3.188292
27	37.69085106	342.9787	2743.83	7.676072	6.092503	5.322291	4.835623	4.488994	4.224305	4.012728	3.838036	3.690271	3.562917	3.451502	3.352833
28	43.59262411	354.0426	2832.34	8.057459	6.395209	5.58673	5.075881	4.71203	4.43419	4.212101	4.028729	3.873622	3.739941	3.62299	3.519419
29	50.16177305	365.1064	2920.85	8.443413	6.701541	5.854336	5.319017	4.937738	4.646589	4.413861	4.221707	4.05917	3.919085	3.796533	3.688
30	57.44680851	376.1702	3009.36	8.83383	7.011416	6.125036	5.564964	5.166055	4.861444	4.617955	4.416915	4.246863	4.100301	3.972082	3.858531

M	SigmaB	b=											
		1	2	3	4	5	6	7	8	9	10	11	12
5.531915		3695.887	2933.427	2562.585	2328.263	2161.368	2033.925	1932.054	1847.943	1776.797	1715.479	1661.834	1614.327
22.12766		2328.263	1847.943	1614.327	1466.714	1361.576	1281.292	1217.118	1164.131	1119.312	1080.684	1046.89	1016.962
49.78723		1776.797	1410.245	1231.962	1119.312	1039.077	977.8091	928.8348	888.3985	854.1949	824.7161	798.9267	776.0876
88.51064		1466.714	1164.131	1016.962	923.9717	857.7393	807.1636	766.7362	733.3568	705.1224	680.7882	659.4994	640.6462
138.2979		1263.975	1003.218	876.3916	796.2547	739.1773	695.5925	660.7532	631.9877	607.656	586.6854	568.3394	552.0921
199.1489		1119.312	888.3985	776.0876	705.1224	654.5776	615.9811	585.1292	559.656	538.1091	519.5386	503.2923	488.9045
271.0638		1009.997	801.6349	700.2926	636.2581	590.6497	555.8226	527.9838	504.9984	485.5558	468.7989	454.1393	441.1567
354.0426		923.9717	733.3568	640.6462	582.0657	540.3419	508.4812	483.0135	461.9858	444.1993	428.8697	415.4586	403.5818
448.0851		854.1949	677.9749	592.2657	538.1091	499.5362	470.0816	446.5372	427.0975	410.6541	396.4822	384.0839	373.104
553.1915		796.2547	631.9877	552.0921	501.609	465.6525	438.1958	416.2485	398.1273	382.7993	369.5887	358.0314	347.7963
669.3617		747.2344	593.0803	518.1034	470.7282	436.9853	411.2189	390.6227	373.6172	359.2328	346.8355	335.9897	326.3847
796.5957		705.1224	559.656	488.9045	444.1993	412.3581	388.0438	368.6083	352.5612	338.9875	327.2888	317.0543	307.9906
934.8936		668.482	530.5746	463.4996	421.1173	390.9307	367.8798	349.4543	334.241	321.3726	310.2819	300.5792	291.9864
1084.255		636.2581	504.9984	441.1567	400.8175	372.086	350.1463	332.609	318.129	305.881	295.3248	286.0898	277.9113
1244.681		607.656	482.2969	421.3252	382.7993	355.3594	334.406	317.657	303.828	292.1305	282.0489	273.2291	265.4182
1416.17		582.0657	461.9858	403.5818	366.6784	340.3941	320.3231	304.2795	291.0328	279.828	270.171	261.7225	254.2406
1598.723		559.0097	443.6863	387.5957	352.1541	326.9109	307.6349	292.2268	279.5049	268.7438	259.4693	251.3555	244.17
1792.34		538.1091	427.0975	373.104	338.9875	314.6881	296.1328	281.3008	269.0545	258.6959	249.7681	241.9577	235.0408
1997.021		519.0584	411.977	359.895	326.9863	303.5472	285.6489	271.3419	259.5292	249.5373	240.9256	233.3917	226.7197
2212.766		501.609	398.1273	347.7963	315.9939	293.3427	276.0461	262.2201	250.8045	241.1485	232.8263	225.5456	219.0979
2439.574		485.5558	385.3859	336.6656	305.881	283.9547	267.2116	253.8281	242.7779	233.4309	225.375	218.3274	212.086
2677.447		470.7282	373.6172	326.3847	296.5402	275.2835	259.0517	246.0769	235.3641	226.3025	218.4927	211.6602	205.6095
2926.383		456.9831	362.7077	316.8544	287.8813	267.2453	251.4875	238.8915	228.4915	219.6945	212.1127	205.4798	199.6057
3186.383		444.1993	352.5612	307.9906	279.828	259.7693	244.4523	232.2087	222.0996	213.5487	206.179	199.7317	194.0219
3457.447		432.2735	343.0957	299.7217	272.3153	252.7951	237.8893	225.9744	216.1368	207.8154	200.6436	194.3693	188.8129
3739.574		421.1173	334.241	291.9864	265.2873	246.2709	231.7498	220.1424	210.5587	202.4521	195.4653	189.353	183.9399
4032.766		410.6541	325.9364	284.7316	258.6959	240.152	225.9916	214.6727	205.327	197.4219	190.6087	184.6483	179.3697
4337.021		400.8175	318.129	277.9113	252.4992	234.3995	220.5783	209.5305	200.4087	192.6929	186.043	180.2253	175.0732
4652.34		391.5495	310.773	271.4852	246.6607	228.9795	215.478	204.6856	195.7747	188.2374	181.7412	176.058	171.025
4978.723		382.7993	303.828	265.4182	241.1485	223.8624	210.6626	200.1114	191.3997	184.0307	177.6797	172.1235	167.203

Sigma_shear											
1	2	3	4	5	6	7	8	9	10	11	12
116.7485	73.54697	56.12684	46.33169	39.92744	35.35769	31.90456	29.18713	26.98297	25.15271	23.60422	22.27395
92.66337	58.37427	44.5479	36.77348	31.69043	28.06342	25.32267	23.16584	21.4164	19.96372	18.73468	17.67885
80.94891	50.99462	38.91618	32.1246	27.68414	24.51566	22.12139	20.23723	18.70895	17.43991	16.36625	15.4439
73.54697	46.33169	35.35769	29.18713	25.15271	22.27395	20.09861	18.38674	16.99821	15.84521	14.86973	14.03171
68.27496	43.01053	32.82318	27.09493	23.34971	20.67731	18.6579	17.06874	15.77974	14.70939	13.80383	13.02589
64.2492	40.47446	30.88779	25.49731	21.97292	19.45809	17.55776	16.0623	14.8493	13.84207	12.9899	12.25783
61.03123	38.44726	29.34075	24.22026	20.87239	18.48352	16.67836	15.25781	14.10556	13.14878	12.33929	11.64389
58.37427	36.77348	28.06342	23.16584	19.96372	17.67885	15.95228	14.59357	13.49149	12.57635	11.80211	11.13698
56.12684	35.35769	26.98297	22.27395	19.19511	16.99821	15.33811	14.03171	12.97206	12.09216	11.34773	10.7082
54.18987	34.13748	26.05177	21.50526	18.53267	16.41159	14.80878	13.54747	12.52429	11.67485	10.95611	10.33865
52.49532	33.06998	25.23712	20.83278	17.95315	15.89839	14.3457	13.12383	12.13274	11.30977	10.6135	10.01536
50.99462	32.1246	24.51566	20.23723	17.43991	15.4439	13.9356	12.74865	11.7859	10.98646	10.31009	9.729045
49.65203	31.27882	23.87021	19.70442	16.98075	15.03729	13.5687	12.41301	11.4756	10.69721	10.03865	9.472897
48.44052	30.51561	23.28777	19.22363	16.56642	14.67038	13.23762	12.11013	11.19559	10.43619	9.793704	9.241758
47.33921	29.82183	22.75832	18.78658	16.18978	14.33684	12.93666	11.8348	10.94106	10.19892	9.571042	9.031645
46.33169	29.18713	22.27395	18.38674	15.84521	14.03171	12.66133	11.58292	10.7082	9.981859	9.367341	8.839424
45.4048	28.60323	21.82835	18.01891	15.52822	13.751	12.40804	11.3512	10.49398	9.782168	9.179944	8.662588
44.5479	28.06342	21.4164	17.67885	15.23517	13.49149	12.17387	11.13698	10.29593	9.597555	9.006696	8.499103
43.75223	27.56218	21.03388	17.36309	14.96305	13.25051	11.95643	10.93806	10.11204	9.426133	8.845827	8.347301
43.01053	27.09493	20.67731	17.06874	14.70939	13.02589	11.75374	10.75263	9.940612	9.266337	8.695869	8.205794
42.31669	26.65784	20.34374	16.79339	14.4721	12.81575	11.56413	10.57917	9.780251	9.116854	8.555588	8.073419
41.66556	26.24766	20.03071	16.53499	14.24942	12.61856	11.38619	10.41639	9.629762	8.976573	8.423943	7.949193
41.05274	25.86161	19.7361	16.29179	14.03984	12.43296	11.21872	10.26319	9.488127	8.844545	8.300044	7.832276
40.47446	25.49731	19.45809	16.0623	13.84207	12.25783	11.06069	10.11861	9.354474	8.719957	8.183126	7.721948
39.92744	25.15271	19.19511	15.84521	13.65499	12.09216	10.91121	9.981859	9.228046	8.602106	8.07253	7.617584
39.40884	24.82601	18.94579	15.63941	13.47763	11.9351	10.76949	9.85221	9.108188	8.490377	7.96768	7.518644
38.91618	24.51566	18.70895	15.4439	13.30915	11.7859	10.63485	9.729045	8.994324	8.384236	7.868073	7.424651
38.44726	24.22026	18.48352	15.25781	13.14878	11.64389	10.50671	9.611816	8.885948	8.283212	7.773268	7.335188
38.00016	23.9386	18.26857	15.08037	12.99587	11.50848	10.38453	9.50004	8.782613	8.186887	7.682873	7.249888
37.57316	23.66961	18.06329	14.91092	12.84984	11.37916	10.26784	9.393289	8.683924	8.094891	7.596541	7.168421

Bending and Shear Stresses											
1	2	3	4	5	6	7	8	9	10	11	12
3812.635	3006.974	2618.712	2374.594	2201.295	2069.283	1963.959	1877.13	1803.78	1740.631	1685.439	1636.601
2420.926	1906.318	1658.875	1503.487	1393.267	1309.356	1242.441	1187.297	1140.728	1100.648	1065.625	1034.641
1857.746	1461.239	1270.878	1151.437	1066.761	1002.325	950.9562	908.6357	872.9039	842.156	815.2929	791.5315
1540.261	1210.463	1052.32	953.1588	882.892	829.4376	786.8348	751.7436	722.1206	696.6334	674.3692	654.6779
1332.25	1046.229	909.2148	823.3496	762.5271	716.2698	679.4111	649.0565	623.4358	601.3948	582.1432	565.118
1183.561	928.873	806.9754	730.6197	676.5505	635.4392	602.687	575.7183	552.9584	533.3807	516.2822	501.1624
1071.028	840.0822	729.6334	660.4783	611.522	574.3061	544.6622	520.2562	499.6613	481.9477	466.4786	452.8006
982.3459	770.1303	668.7096	605.2315	560.3056	526.1601	498.9658	476.5794	457.6907	441.446	427.2607	414.7188
910.3218	713.3326	619.2486	560.383	518.7313	487.0798	461.8753	441.1292	423.6261	408.5743	395.4316	383.8122
850.4445	666.1252	578.1439	523.1143	484.1852	454.6074	431.0572	411.6748	395.3237	381.2635	368.9875	358.1349
799.7297	626.1503	543.3405	491.561	454.9385	427.1173	404.9684	386.741	371.3656	358.1453	346.6032	336.4
756.117	591.7806	513.4202	464.4365	429.798	403.4877	382.5439	365.3098	350.7734	338.2753	327.3644	317.7196
718.1341	561.8534	487.3698	440.8217	407.9114	382.9171	363.023	346.654	332.8482	320.9791	310.6178	301.4593
684.6986	535.514	464.4445	420.0411	388.6524	364.8167	345.8466	330.2392	317.0766	305.761	295.8835	287.1531
654.9952	512.1187	444.0835	401.5859	371.5492	348.7428	330.5937	315.6628	303.0716	292.2479	282.8001	274.4499
628.3974	491.173	425.8558	385.0651	356.2393	334.3548	316.9408	302.6158	290.5362	280.1528	271.0899	263.08
604.4145	472.2896	409.4241	370.173	342.4391	321.3859	304.6348	290.8561	279.2378	269.2515	260.5355	252.8326
582.657	455.1609	394.5204	356.6663	329.9233	309.6243	293.4747	280.1915	268.9918	259.3657	250.9644	243.5399
562.8107	439.5391	380.9289	344.3494	318.5103	298.8994	283.2984	270.4673	259.6493	250.3517	242.2375	235.067
544.6195	425.2223	368.4736	333.0626	308.0521	289.072	273.9738	261.5571	251.0891	242.0926	234.2415	227.3037
527.8725	412.0437	357.0093	322.6744	298.4268	280.0274	265.3923	253.3571	243.2111	234.4919	226.883	220.1594
512.3937	399.8649	346.4154	313.0752	289.5329	271.6703	257.4631	245.7805	235.9323	227.4692	220.0842	213.5587
498.0358	388.5693	336.5905	304.1731	281.2852	263.9204	250.1103	238.7547	229.1827	220.9573	213.7799	207.438
484.6737	378.0585	327.4486	295.8903	273.6114	256.7101	243.2694	232.2182	222.9032	214.899	207.9148	201.7438
472.201	368.2484	318.9168	288.1605	266.4501	249.9815	236.8856	226.1186	217.0435	209.2457	202.4419	196.4304
460.5261	359.067	310.9322	280.9267	259.7485	243.6849	230.9119	220.4109	211.5603	203.9557	197.3207	191.4586
449.5703	350.452	303.4406	274.1398	253.4611	237.7775	225.3075	215.0561	206.4162	198.993	192.5163	186.7943
439.2647	342.3493	296.3948	267.757	247.5483	232.2222	220.0372	210.0205	201.5789	194.3262	187.9986	182.4083
429.5496	334.7116	289.7538	261.7411	241.9754	226.9865	215.0701	205.2748	197.02	189.9281	183.7409	178.2749
420.3725	327.4976	283.4815	256.0594	236.7122	222.0417	210.3792	200.7929	192.7146	185.7746	179.7201	174.3714

Appendix B- Simplified Design Iterations using OFAT

Factors	min	inc	max
h	0.5	0.5	2
L	10	2	26
r	0.25	0.25	0.5

Responses	Target Value
sigma_vm [Mpa]	550
d [mm]	0.2

Test Run	Factors			Repsonses		Notes
	h	L	r	sigma_vm	d	
1	1	6	0.25	1113	0.1948	
2	1	8	0.25	1774	0.4918	
3	1	10	0.25	2200	1.001	beams come into contact;
4	1	12	0.25			
5	1	14	0.25			
6	1	16	0.25			
7	1	18	0.25			
8	1	20	0.25			
9	1	22	0.25			
10	1	24	0.25			
11	1	26	0.25			
12	1.5	6	0.25	632.4	0.079	
13	1.5	8	0.25	984.4	0.1867	
14	1.5	10	0.25	1414	0.38	
15	1.5	12	0.25	1896	0.6879	
16	1.5	14	0.25			
17	1.5	16	0.25			
18	1.5	18	0.25			
19	1.5	20	0.25			
20	1.5	22	0.25			
21	1.5	24	0.25	1.02E+06	60.25	beams come into contact; nonlinear problem
22	1.5	26	0.25	7.72E+05	283	beams come into contact; nonlinear problem
23	2	6	0.25	4.00E+02	0.04426	probed stresses at bends because of stress singularity
24	2	8	0.25	6.08E+02	0.09934	probed stresses at bends because of stress singularity
25	2	10	0.25	815	0.196	
26	2	12	0.25	594	0.165	
27	2	14	0.25	27060	0.3095	beams come into contact; nonlinear problem
28	2	16	0.25	347200	0.3115	beams come into contact; nonlinear problem
29	2	18	0.25			
30	2	20	0.25			

31	2	22	0.25			
32	2	24	0.25			
33	2	26	0.25			
34	1	6	0.5	839.2	0.1744	
35	1	8	0.5	1358	0.4497	
36	1	10	0.5	1999	0.97	
37	1	12	0.5	1591	1.004	contact; mesh adaptation failed at 2nd iteration
38	1	14	0.5	3.13E+06	41.69	beams come into contact; nonlinear problem
39	1	16	0.5			
40	1	18	0.5			
41	1	20	0.5			
42	1	22	0.5			
43	1	24	0.5			
44	1	26	0.5			
45	1.5	6	0.5	388.9	0.07167	Stress singularity at fillet locations; probed stresses
46	1.5	8	0.5	631.9	0.1722	Stress singularity at fillet locations; probed stresses
47	1.5	10	0.5	1919	0.3547	stress singularity at fillet locations
48	1.5	12	0.5	1300	0.6478	stress singularity at fillet locations; probed stress result
49	1.5	14	0.5			
50	1.5	16	0.5			
51	1.5	18	0.5			
52	1.5	20	0.5			
53	1.5	22	0.5			
54	1.5	24	0.5			
55	1.5	26	0.5			
56	2	6	0.5			not possible with this h and H value
57	2	8	0.5			
58	2	10	0.5			
59	2	12	0.5			
60	2	14	0.5			
61	2	16	0.5			
62	2	18	0.5			
63	2	20	0.5			
64	2	22	0.5			
65	2	24	0.5			
66	2	26	0.5			

Whittled Results							
Test Run	Factors				Repsones		Notes
	h	L	r	sigma_vm	d		
1	1	6	0.25	1113	0.1948		
2	1	8	0.25	1774	0.4918		
3	1	10	0.25	2200	1.001	beams come into contact; nonlinear problem; probed stresses at bends because of stress singularity	
4	1.5	6	0.25	632.4	0.079		
5	1.5	8	0.25	984.4	0.1867		
6	1.5	10	0.25	1414	0.38		
7	1.5	12	0.25	1896	0.6879		
8	2	6	0.25	400	0.04426	probed stresses at bends because of stress singularity	
9	2	8	0.25	608.1	0.09934	probed stresses at bends because of stress singularity	
10	2	10	0.25	815	0.196		
11	2	12	0.25	594	0.165		
12	1	6	0.5	839.2	0.1744		
13	1	8	0.5	1358	0.4497		
14	1	10	0.5	1999	0.97		
15	1.5	6	0.5	388.9	0.07167		
16	1.5	8	0.5	631.9	0.1722		
17	1.5	10	0.5	1919	0.3547		
18	1.5	12	0.5	1300	0.6478		

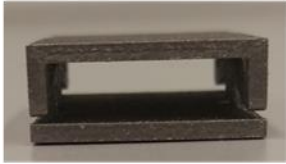
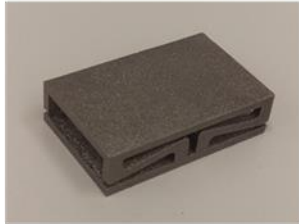
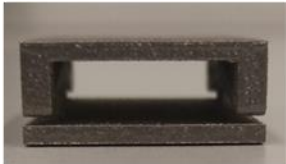
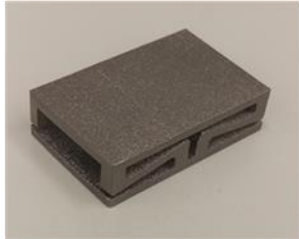


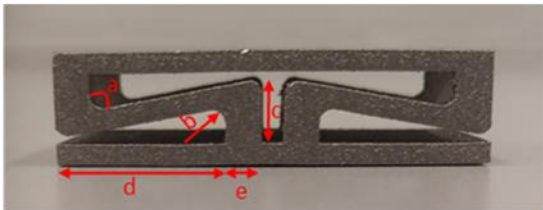
Adjusting L (H=6mm)								
Test Run	Factors					Repsones		
	h_s	h_l	L	r_s	r_l	sigma_vm	F_R	
1	0.5	4	8	0.25	0.75	1128	1200	
2	0.75	3.5	8	0.5	0.75	956.2	1293	
3	0.75	3.5	8.25	0.5	0.75	741	1205	
3	0.75	3.5	8.5	0.5	0.75	733.7	1116	
4	0.75	3.5	8.75	0.5	0.75	695.7	1035	

Appendix C: Axial Loading of Rectangular Models

Methods

Computational Model

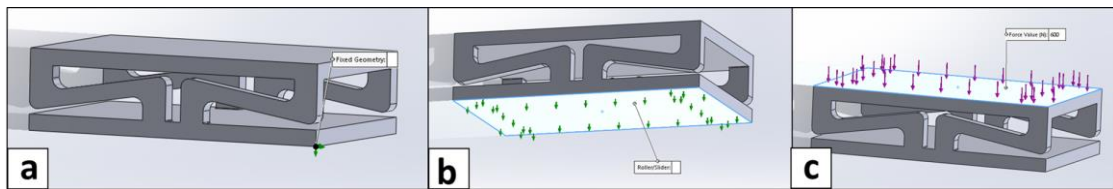
Rectangular models with S-shaped beams were created using CAD software (Solidworks). S-shaped beams, positioned along the edges of the model, provide deflection in the entire model through bending. Three configurations with identical beam geometries were tested. However, the three models differ in thickness and in the number of beams along the periphery. Two of the configurations consist of having the S-beams located along two opposing sides, but the thickness of the beams vary where one configuration had a beam thickness of 2 mm and the other configuration had a beam thickness of 3mm. These parts will be referred to as D2 and D3, respectively. The third configuration has the same beam geometry as D3, but the beams are located on all four sides of the part. This configuration will be referred to as Q3 hereinafter. The three rectangular models are presented in the table below.

	<i>Side View</i>	<i>Isometric View</i>
2 mm Thick Beams Along Two Opposing Sides (D2)		
3 mm Thick Beams Along Two Opposing Sides (D3)		
3 mm Thick Beams Along All Four Sides (Q3)		
Beam Dimensions [mm]	 <p>$a = 80.62^\circ$, $b = 1.25$, $c = 2.55$, $d = 15$, $e = 3$</p>	

Rectangular models with S-beam design.

These models were used to develop computational models that calculated the stiffness of the parts during axial compression. Solidworks Simulation was used to perform static analyses on the parts. A fixed restraint was applied to one of the corners on the bottom

surface of the part and a roller/slider was applied to the bottom surface. A normal force applied to the top surface of the part. The default tetrahedral element mesh with a size of 1.6 mm was used. Local mesh refinement was achieved by using the h-adaptive mesh refinement where target accuracy was set to 99% and was set to run five iterations. The models accounted for large displacements so that changes in the stiffness would be updated as the model deformed during the analyses. Because the stiffness varies between the different configurations, the maximum applied loads were 600 N, 1200 N and 2400 N for the thin beam, thick beam and eight beam configurations, respectively. These loads correspond to the load that resulted in von Mises stresses equal to the yield strength of Ti6Al4V.



Locations of boundary conditions and load application: (a) a fixed restraint was defined to a corner on the bottom surface of the part, (b) a roller/slider was defined to the bottom surface and (c) the compressive load was applied to the top surface of the rectangular models.

Experimental Model

Experimental testing was performed on 3D printed versions of the CAD generated parts. The 3D printing parameters were identical to what was used on the package prototype (Table 3 1). These 3D printed parts were compressed using a TTD Series mechanical testing machine (Adelaide Testing Machine (ATM), Inc., Toronto, ON). Compression plates were secured to the machine's fixture adapters. The part being tested was placed in the centre of the bottom compression plate. Once in position, by manually controlling the position of the crosshead using the dial responsible for actuation, the crosshead was lowered at a loading rate of 6 mm/min until contact was achieved. The initial force and crosshead position were recorded. Again, by manually controlling the crosshead position,

the force and position were recorded in approximately 100 N increments. As in the computational models, the maximum applied loads were 600 N, 1200 N and 2400 N for the thin beam, thick beam and eight beam configurations, respectively. The experimental stiffness of the three configurations, calculated from the measured loads and crosshead displacements, were compared to the computational models' stiffness.

Results

Axial Loading of Rectangular Models

The stiffness in the 3D printed rectangular models and their respective computational models had a similar trend as what was observed with the prototype. The results are summarized in the table below. D2, D3 and Q3 had stiffness values 61%, 59% and 67% less than what was calculated in the computational models, respectively.

	k [N/mm]		
	D2	D3	Q3
SW Simulation	2222	3243	6154
ATM	863	1328	2027
Percent Error	61	59	67

Tabulated stiffness from computational and experimental models. The manufactured parts have shown to be more compliant than what was determined in the computational models.

Discussion

In addition, 3D printed rectangular models were subjected to axial loading. The axial compression testing of additional rectangular models yielded similar results as the prototype—the stiffness of the as-built rectangular parts were about 60% less than the computational model's stiffness. Overall, from the axial testing performed on these 3D

printed specimens, the compliance of as-built 3D printed parts were consistently lower than what was expected based on the computational models.

Appendix D: Stiffness Calculation of Single Silicone Spacer

$$w = 15 \text{ mm}, L = 6 \text{ mm}, h = 18 \text{ mm}$$

$$A = 15 \times 18 = 270 \text{ mm}^2$$

$$\text{Shore A Hardness} = 25$$

$$E = 0.949 \text{ N/mm}^2$$

$$k_{\text{silicone}} = EA/L = (0.949)(270)/6 = \mathbf{42.7 \text{ N/mm}}$$

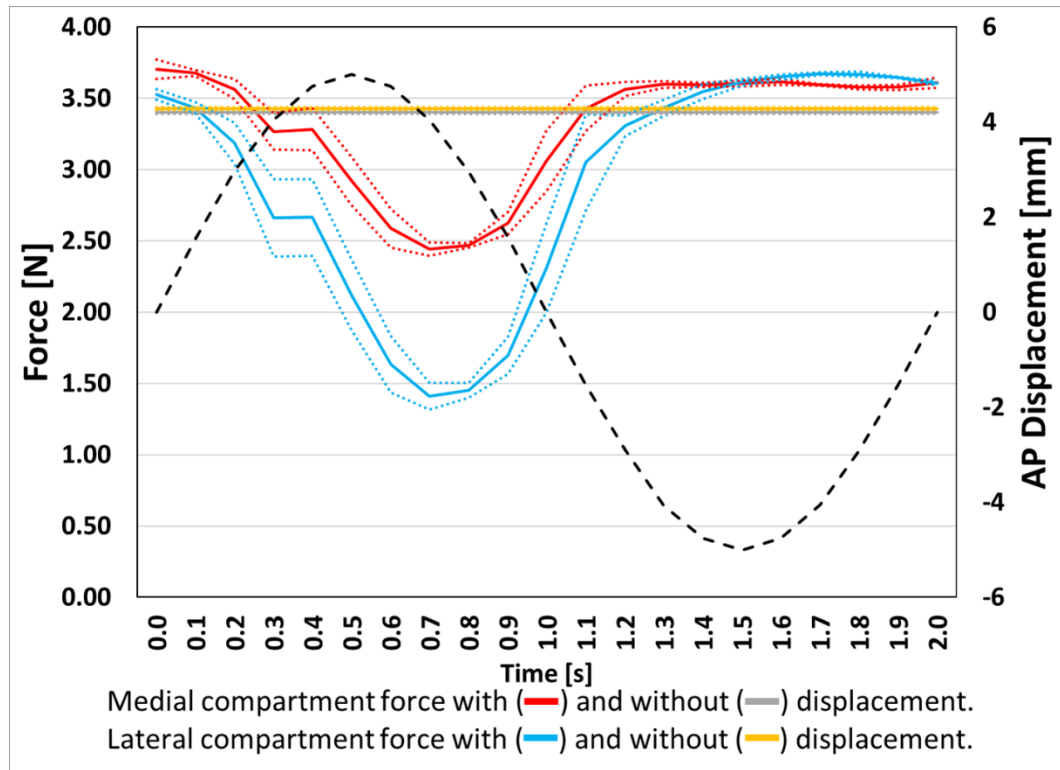
Appendix E: AP Translation and IE Rotation Testing

Methods

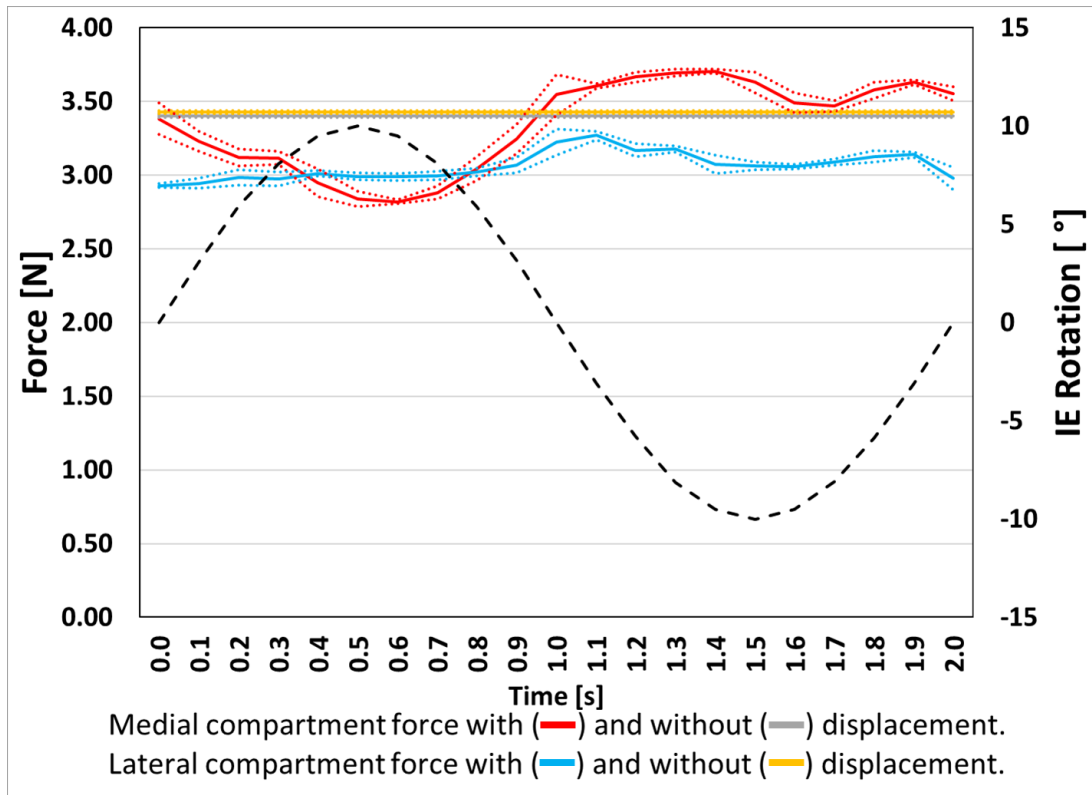
The addition of an internal-external (IE) rotation of $\pm 10^\circ$, and an anteroposterior (AP) translation of ± 5 mm were tested in separate subsequent loading scenarios.

Results

The Flexiforce sensors measured changes in the load distribution when a cyclic AP translation was applied. Loads reached their highest magnitude as the tibia translated anteriorly with respect to the femur. As the tibia translated posteriorly, the measured compartment loads decreased. During IE rotation testing, the measured medial compartmental load had a larger range than the lateral compartment. The medial condyle was more mobile along the AP axis; the joint seemed to exhibit a lateral pivot.



Flexiforce measurements during anteroposterior translation.



Flexiforce measurements during cyclic internal/external rotation.

Appendix F: Copyright Approval

ELSEVIER LICENSE TERMS AND CONDITIONS

Nov 21, 2019

This Agreement between The University of Western Ontario -- Geoffrey Yamomo ("You") and Elsevier ("Elsevier") consists of your license details and the terms and conditions provided by Elsevier and Copyright Clearance Center.

License Number	4683870212283
License date	Oct 07, 2019
Licensed Content Publisher	Elsevier
Licensed Content Publication	Bone
Licensed Content Title	Diagnosis of osteoarthritis: Imaging
Licensed Content Author	Hillary J. Braun, Garry E. Gold
Licensed Content Date	Aug 1, 2012
Licensed Content Volume	51
Licensed Content Issue	2
Licensed Content Pages	11
Start Page	278
End Page	288
Type of Use	reuse in a thesis/dissertation
Portion	figures/tables/illustrations
Number of figures/tables/illustrations	1
Format	both print and electronic
Are you the author of this Elsevier article?	No
Will you be translating?	No
Original figure numbers	Figure 1
Requestor Location	Geoffrey Yamomo 1151 Richmond St London, ON N6A 3K7 Canada Attn: The University of Western Ontario
Publisher Tax ID	GB 494 6272 12

Articles

Early aseptic loosening of a mobile-bearing total knee replacement

A case-control study with retrieval analyses

Ines Kutzner, Geir Hallan, Paul Johan Høl, Ove Furnes, Øystein Gøthesen, Wender Figved & ...[show all](#)
 Pages 77-83 | Received 28 Feb 2017, Accepted 29 Sep 2017, Published online: 06 Nov 2017

Download citation <https://doi.org/10.1080/17453674.2017.1398012> [Check for updates](#)

[Full Article](#) [Figures & data](#) [References](#) [Supplemental](#) [Citations](#) [Metrics](#) [Licensing](#) [PDF](#)

© 2017 The Author(s). Published by Taylor & Francis on behalf of the Nordic Orthopedic Federation.

This is an Open Access article distributed under the terms of the Creative Commons Attribution-Non-Commercial License (<https://creativecommons.org/licenses/by-nc/3.0>)



Attribution-NonCommercial 3.0 Unported (CC BY-NC 3.0)

This is a human-readable summary of (and not a substitute for) the [license](#). [Disclaimer](#).

You are free to:

Share — copy and redistribute the material in any medium or format

Adapt — remix, transform, and build upon the material

The licensor cannot revoke these freedoms as long as you follow the license terms.

Under the following terms:



Attribution — You must give [appropriate credit](#), provide a link to the license, and [indicate if changes were made](#). You may do so in any reasonable manner, but not in any way that suggests the licensor endorses you or your use.



NonCommercial — You may not use the material for [commercial purposes](#).

No additional restrictions — You may not apply legal terms or [technological measures](#) that legally restrict others from doing anything the license permits.

Notices:

You do not have to comply with the license for elements of the material in the public domain or where your use is permitted by an applicable [exception or limitation](#).

No warranties are given. The license may not give you all of the permissions necessary for your intended use. For

Springer Science and Bus Media B V LICENSE
TERMS AND CONDITIONS

Nov 21, 2019

This is a License Agreement between The University of Western Ontario -- Geoffrey Yamomo ("You") and Springer Science and Bus Media B V ("Springer Science and Bus Media B V") provided by Copyright Clearance Center ("CCC"). The license consists of your order details, the terms and conditions provided by Springer Science and Bus Media B V, and the payment terms and conditions.

All payments must be made in full to CCC. For payment instructions, please see information listed at the bottom of this form.

License Number	4683980860348
License date	Oct 07, 2019
Licensed content publisher	Springer Science and Bus Media B V
Licensed content title	Knee surgery, sports traumatology, arthroscopy : official journal of the ESSKA
Licensed content date	Jan 1, 1993
Type of Use	Thesis/Dissertation
Requestor type	Academic institution
Format	Print, Electronic
Portion	image/photo
Number of images/photos requested	1
The requesting person/organization is:	Geoffrey Yamomo
Title or numeric reference of the portion(s)	Fig. 2
Title of the article or chapter the portion is from	Internal femoral component rotation adversely influences load transfer in total knee arthroplasty: a cadaveric navigated study using the Verasense device
Editor of portion(s)	N/A
Author of portion(s)	Manning, William A Ghosh, Kanishka M Blain, Alasdair Longstaff, Lee Rushton, Steven P Deehan, David J
Volume of serial or monograph.	26
Issue, if republishing an article from a serial	5
Page range of the portion	1577-1585
Publication date of portion	15 July 2017
Rights for	Main product
Duration of use	Life of current edition
Creation of copies for the disabled	no

ELSEVIER LICENSE
TERMS AND CONDITIONS

Nov 21, 2019

This Agreement between The University of Western Ontario -- Geoffrey Yamomo ("You") and Elsevier ("Elsevier") consists of your license details and the terms and conditions provided by Elsevier and Copyright Clearance Center.

License Number	4701440013394
License date	Nov 03, 2019
Licensed Content Publisher	Elsevier
Licensed Content Publication	The Journal of Arthroplasty
Licensed Content Title	Tibial Forces Measured In Vivo After Total Knee Arthroplasty
Licensed Content Author	Darryl D. D'Lima,Shantann Patil,Nikolai Steklov,John E. Slamin,Clifford W. Colwell
Licensed Content Date	Feb 1, 2006
Licensed Content Volume	21
Licensed Content Issue	2
Licensed Content Pages	8
Start Page	255
End Page	262
Type of Use	reuse in a thesis/dissertation
Portion	figures/tables/illustrations
Number of figures/tables/illustrations	1
Format	both print and electronic
Are you the author of this Elsevier article?	No
Will you be translating?	No
Title	Design and Analysis of a 3D Printed Compliant Energy Harvester Package for Knee Implants
Institution name	n/a
Expected presentation date	Dec 2019
Portions	Fig. 1
Requestor Location	The University of Western Ontario 1151 Richmond St London, ON N6A 3K7 Canada Attn: The University of Western Ontario
Publisher Tax ID	GB 494 6272 12
Total	0.00 CAD

ELSEVIER LICENSE
TERMS AND CONDITIONS

Nov 21, 2019

This Agreement between The University of Western Ontario -- Geoffrey Yamomo ("You") and Elsevier ("Elsevier") consists of your license details and the terms and conditions provided by Elsevier and Copyright Clearance Center.

License Number	4701440681522
License date	Nov 03, 2019
Licensed Content Publisher	Elsevier
Licensed Content Publication	Journal of Biomechanics
Licensed Content Title	A multiaxial force-sensing implantable tibial prosthesis
Licensed Content Author	Bryan Kirking, Janet Krevolin, Christopher Townsend, Clifford W. Colwell, Darryl D. D'Lima
Licensed Content Date	Jan 1, 2006
Licensed Content Volume	39
Licensed Content Issue	9
Licensed Content Pages	8
Start Page	1744
End Page	1751
Type of Use	reuse in a thesis/dissertation
Portion	figures/tables/illustrations
Number of figures/tables/illustrations	1
Format	both print and electronic
Are you the author of this Elsevier article?	No
Will you be translating?	No
Title	Design and Analysis of a 3D Printed Compliant Energy Harvester Package for Knee Implants
Institution name	n/a
Expected presentation date	Dec 2019
Portions	Figure 3
Requestor Location	The University of Western Ontario 1151 Richmond St London, ON N6A 3K7 Canada Attn: The University of Western Ontario
Publisher Tax ID	GB 494 6272 12
Total	0.00 CAD
Terms and Conditions	

IOP Publishing LICENSE
TERMS AND CONDITIONS

Nov 21, 2019

This is a License Agreement between The University of Western Ontario -- Geoffrey Yamomo ("You") and IOP Publishing ("IOP Publishing") provided by Copyright Clearance Center ("CCC"). The license consists of your order details, the terms and conditions provided by IOP Publishing, and the payment terms and conditions.

All payments must be made in full to CCC. For payment instructions, please see information listed at the bottom of this form.

License Number	4674851289408
License date	Sep 23, 2019
Licensed content publisher	IOP Publishing
Licensed content title	Smart Materials and Structures
Licensed content date	Jan 1, 1992
Type of Use	Educational/Instructional Program
Requestor type	Author of requested content
Format	Electronic
Portion	chart/graph/table/figure
Number of charts/graphs/tables/figures	6
The requesting person/organization is:	Geoffrey Yamomo
Title or numeric reference of the portion(s)	Figure 2. Upper and lower layers of ... SEM image for PDMS layer, Figure 3. Operating mechanism for the triboelectric energy harvester, Figure 6. The variation of the short-circuit ... loads at 1 Hz frequency, Figure 9. The variation of the voltage...generated by increasing the frequency., Figure 11. The time domain output voltage... MΩ and 1 Hz frequency, Figure 13. The average generated power for... MΩ and 1 Hz frequency.
Title of the article or chapter the portion is from	A smart knee implant using triboelectric energy harvesters
Editor of portion(s)	N/A
Author of portion(s)	Abwathiqbellah Ibrahim
Volume of serial or monograph.	28
Page range of the portion	1-11
Publication date of portion	25 January 2019
Rights for	Main product
Duration of use	Current edition and up to 5 years
Creation of copies for the disabled	no
With minor editing privileges	no
For distribution to	Canada
In the following language(s)	Original language of publication

Appendix G- Mechanical Testing Machine Technical Data Sheets

Instron 8874 Mechanical Testing Machine



The difference is measurable

8874 BIAxIAL SERVOHYDRAULIC FATIGUE TESTING SYSTEM

25 kN/100 Nm

The Instron® 8874 is a compact tabletop biaxial servohydraulic testing system that meets the challenging demands of various static and dynamic tests. The system carries out axial, torsion, or combined axial-torsion tests. With the actuator in the upper crosshead and a lower t-slot table, the 8874 makes an ideal platform for testing a variety of medical devices, biomaterials, advanced materials, and other components testing.

FEATURES

- Double-acting servohydraulic actuator with force capacity up to ± 25 kN (± 5620 lbf) and torque capacity of ± 100 Nm (880 in-lb)
- High-stiffness, precision-aligned load frame with twin columns and actuator in upper crosshead
- 100 mm (4 in) of useable axial stroke and $\pm 130^\circ$ of rotation
- Designed for both dynamic and static testing on a variety of materials and components
- Choice of hydraulic configuration and dynamic performance to suit application
- Adjustable upper crosshead with hydraulic lifts and manual locks fitted as standard for easy adjustment of daylight
- Patented, Dynacell™ load cell technology for faster testing and reduction of inertial errors
- Compact tabletop servohydraulic fatigue testing system – frame requires less than 0.4 m² (4.3 ft²) of space
- Designed to be used with the 3520 Series of Hydraulic Power Units
- Compatible with a large range of grips, fixtures, chambers, video extensometers, protective shields, and other accessories
- Patented stiffness based tuning algorithm that enables users to tune a variety of specimens in seconds

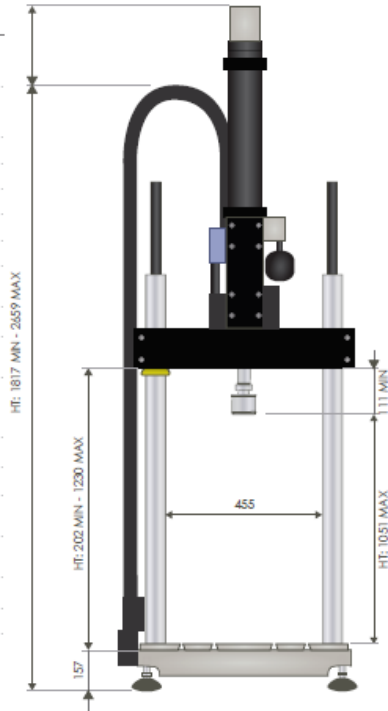
CONTROLLER AND SOFTWARE

The 8874 is supplied with a two-axis digital 8800MT controller that provides full system control, including features such as stiffness based tuning, amplitude control specimen protect, 19-bit resolution across the full range of transducers, and adaptive control technology. It also allows access to WaveMatrix 2 Dynamic Testing Software, Bluehill® Software for axial static tests, and other application specific software, such as the Fracture Mechanics suite.



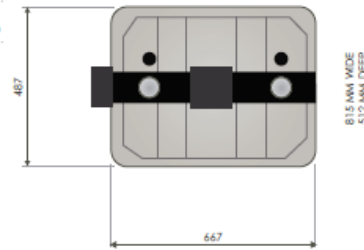
FRAME SPECIFICATIONS

Daylight Opening (Maximum Between Load Cell and Actuator at Mid-stroke, with Largest Capacity Actuator)	mm	1001
	in	39.41
Dynamic Load Capacity	kN	±25
	lbf	±5620
Torque Load Capacity	Nm	100
	inlb	880
Actuator Stroke (Total)	mm	100
	in	4
Actuator Rotation	kN	±130°
Configuration	Twin-Column High-Stiffness Load Frame with Actuator in Upper Crosshead and T-Slot Base	
Lift and Locks	Hydraulically-Powered Lifts and Manual Locks	
Load Cell	Patented, Dynacell™ Fatigue-Rated Load Cell with Capacity to Suit Actuator	
Load Weighing Accuracy	±0.002% of Load Cell Capacity or 0.5% of Indicated Load, Whichever is Greater - Down to 1/250th of Full Scale	
Hydraulic Pressure Supply (Required)	bar	207
	psi	3000
Electrical Supply	Single-Phase Mains 90-132 or 180-284 V 45/65 Hz with Power Consumption 800 VA Max	
Operating Environment	+10 to +38°C (+50 to +100°F) with 10 to 90% Humidity Non-Condensing	
Frame Stiffness	kN/mm	280
Frame Weight	kg	287
	lb	634



MECHANICAL ACCESSORIES

Load Cell	8 × M8 on 75 PCD
Actuator	8 × M8 on 75 mm PCD 8 × 9 mm Diameter Through Holes on 75 mm PCD
Table and Crosshead	4 × M10 Holes on a 280 mm × 90 mm for Accessory Mounting 8 × M10 × 20 Deep on 100 mm PCD (Table) with 40 mm Location Diameter 4 × M10 T-Slots Running Front to Back, Spaced 80 and 100 mm from Centerline
Table and Crosshead	4 × M10 Holes on a 280 mm × 90 mm for Accessory Mounting 8 × M10 × 20 deep on 100 mm PCD (Table) with 40 mm Location Diameter



Instron® 8874 Dimensions (All Dimensions in mm)

ACCESSORIES

8260C	±25 kN / ±100 Nm Fatigue Rated Hydraulic Wedge Grips
-------	--

1) US Patent Number 6508132

www.instron.com



Worldwide Headquarters
825 University Ave, Norwood, MA 02062-2643, USA
Tel: +1 800 584 8378 or +1 781 575 5000

European Headquarters
Coronation Road, High Wycombe, Bucks HP12 3BY, UK
Tel: +44 1494 484848

Instron is a registered trademark of Illinois Tool Works Inc. (ITW). Other names, logos, icons and marks identifying Instron products and services referenced herein are trademarks of ITW and may not be used without the prior written permission of ITW. Other product and company names listed are trademarks or trade names of their respective companies. Copyright © 2018 Illinois Tool Works Inc. All rights reserved. All of the specifications shown in this document are subject to change without notice.

8874_SHFatigueTestingSystems_V5

Adapted from: <https://www.instron.us/-/media/literature-library/products/2012/10/8874-servo-hydraulic-fatigue-testing-system.pdf?la=en>

Instron Load Cells



The difference is measurable®

LOAD CELLS FOR DYNAMIC SYSTEMS

250 N - 2500 kN



Instron® load cells are a key part of a materials testing system. Among our competitors, Instron is the only global materials testing supplier that designs and manufactures its own load cells. This ensures that Instron load cells meet the unique requirements of materials testing such as; high accuracy over a wide measurement range, high stiffness, resistance to offset loads, accurate alignment and excellent zero stability.

During tests carried out on dynamic machines, elements of the system are subject to acceleration. As a result, in addition to the force applied to the specimen, the load cell also reads forces resulting from its own movement and the mass of the grips and fixtures attached to it.

The accelerometer in a Dynacell is right at the heart of the load cell, directly on the load axis. This removes the risk of errors in the acceleration reading resulting from off center loading. This way, the accelerometer is on the load line eliminating both amplitude and phase errors and automatic set-up takes less than one minute.

The 2527 Series load cells are designed for use with Dynamic Testing Systems; offering exceptional performance with the ability to measure forces as low as 1/250th of the force capacity to an accuracy of 0.5% of reading. Automatic transducer recognition and electrical calibration, makes them easy to use. The load cells can withstand loads up to 150% of their force capacity without damage and 300% without mechanical failure. All Instron load cells are individually temperature-compensated and tested for accuracy and repeatability on calibration apparatus that is traceable to international standards, with a measurement uncertainty that does not exceed one-third of the permissible error of the load cell.

FEATURES AND BENEFITS

- Force capacities from ± 250 N to ± 2500 kN (56 - 562500 lbf)
- Torque capacities from ± 25 Nm to ± 2000 Nm (225 - 17702 in-lb)
- Suitable for a range of test types, including tension, compression, cyclic and reverse stress
- Automatic recognition with electronic serial number and electrical calibration allows for simple, error-free operation
- 300% of force capacity overload capability –reduces the possibility of damage
- Precision machining and construction along with high axial and lateral stiffness helps to maintain system alignment
- Low sensitivity to offset loads improves consistency of results
- Complies with all international force measurement standards, including BS1610 Part 1 1992 Grade 0.5, ASTM E4, ISO 7500-1 class 0.5, EN10002-2 class 0.5 and JIS B7721, B7733
- Fatigue life in excess of 10^9 full stress reversed cycles
- Highly accurate static load cell, with a measurement accuracy better than 0.25% of reading down to 1% of the load cell full scale. When used with 8800MT, an accuracy of 0.5% of reading down to 1/250th of the load cell full scale is easily achieved.

LOAD CELLS FOR DYNAMIC SYSTEMS 250 N - 2500 KN

SPECIFICATIONS

Catalog Number	Force Capacity		Torque Capacity		Mechanical Fitting (Frame)	Mechanical Fitting (Load String)	Effective Length		Diameter		Weight	
	kN	lbf	Nm	in-lb			mm	in	mm	in	kg	lb
2527-131	±0.25	56	-	-	3x M6 on 57 mm PCD	Central M6 x 1	42	1.65	75	2.95	1	2.2
2527-130	±1	225	-	-	3x M6 on 57 mm PCD	Central M6 x 1	42	1.65	75	2.95	1	2.2
2527-302	±1	225	±25	±225	3x M6 on 75 mm PCD	3x M6 on 75 mm PCD or 3x M6 on 57 mm PCD	68	2.68	94	3.7	1.3	2.87
2527-129	±2	450	-	-	3x M6 on 57 mm PCD	Central M6 x 1	42	1.65	75	2.95	1	2.2
2527-153	±5	1,125	-	-	3x M6 on 75 mm PCD	3x M6 on 75 mm PCD or 3x M6 on 57 mm PCD	68	2.68	94	3.7	2	4.4
2527-303	±5	1,125	±25	±225	3x M6 on 75 mm PCD	3x M6 on 75 mm PCD or 3x M6 on 57 mm PCD	68	2.68	94	3.7	2	4.4
2527-102	±10	2,250	-	-	6x M6 on 75 mm PCD	Central M20xL5	71	2.8	107	4.2	4	8.8
2527-202	±10	2,250	±100	±880	6x M8 on 75 mm PCD	6x M8 on 75 mm PCD	88	3.38	94	3.7	2.5	5.5
2527-101	±25	5,620	-	-	Central M20xL5 or 8 x M10 on 75 mm PCD	Central M20xL5	71	2.8	107	4.2	4	8.8
2527-201	±25	5,620	±100	±880	6x M8 on 75 mm PCD	6x M8 on 75 mm PCD	88	3.38	94	3.7	2.5	5.5
2527-100	±50	11,250	-	-	Central M30x2 or 6x M10 on 100 mm PCD	Central M30x2	99	3.9	154	6.06	10	22
2527-111	±100	22,500	-	-	Central M30x2 or 6x M10 on 100 mm PCD	Central M30x2	99	3.9	154	6.06	10	22
2527-115	±250	56,250	-	-	Central M48x2	Central M48x2	131	5.15	203	8	25.5	56.21
2527-125	±500	112,500	-	-	Central M72	Central M72x2 6x M20 on 150 mm PCD 6x M30 on 225 mm PCD	232	9.13	305	12	95	209.4
2527-120	±1000	225,000	-	-	Central M100	Central M100 6x M20 on 150 mm PCD 12x M30 on 225 mm PCD	360	12.17	305	12	140	308.8
2527-140	±2500	562,500	-	-	Central M150	Central M150	450	17.71	428	16.85	322	710

www.instron.com



Worldwide Headquarters
825 University Ave, Norwood, MA 02062-2643, USA
Tel: +1 950 564 9378 or +1 781 575 5000

European Headquarters
Comarion Road, High Wycombe, Bucks HP12 3BY, UK
Tel: +44 1494 464846

Instron is a registered trademark of Illinois Tool Works Inc. (ITW). Other names, logos, icons and marks identifying Instron products and services referenced herein are trademarks of ITW and may not be used without the prior written permission of ITW. Other product and company names listed are trademarks or trade names of their respective companies. Copyright © 2016 Illinois Tool Works Inc. All rights reserved. All of the specifications shown in this document are subject to change without notice.

DynamicSystemLoadCells_PodV1

(Adapted from: <https://www.instron.us/-/media/literature-library/products/2005/06/dynacell-fatigue-rated-load-cells.pdf?la=en-us&hash=35B791E3BD0C0B1AA5142F5E4408B4066304A5C6>)

8800 MiniTower Control Electronics



8800 MiniTower Control Electronics

The 8800 controller is a class-leading, fully digital dynamic controller that utilizes Instron® core technologies and is capable of running static and high-frequency dynamic tests. Found at the heart of Instron's servohydraulic testing systems, the 8800 controller provides full system control, machine safety, transducer conditioning, and data acquisition, as well as acts as the foundation for the user interface to the testing machine.

Features

- Dedicated materials testing hardware and firmware-based controller developed through decades of research, development, and continuous use
- Continuous synchronous data acquisition and loop closure rates of 5 kHz
- Up to 24-bit data resolution across the entire span of each transducer provides maximum data quality
- Automatic identification and calibration of all compatible transducers prevents configuration errors and simplifies setup
- Specimen Protect function helps to avoid damage of specimen and fixtures during test setup and end of test
- Continuous update of PID control terms with Adaptive Control - optimizes the control parameters throughout a test to suit the changing stiffness characteristics of the specimen
- Expandable architecture; extensive analog and digital channel capabilities



Handset and Frame Controls

The handset, frame controls, and emergency stop button make up the hardware interface that is rigidly mounted to the testing machine. Their functionality includes switching the machine into low power or high power mode; offering fast or fine positioning of the actuator; and where fitted, opening and closing of hydraulic grips. Uniquely, the 8800MT offers additional protection by locking out the actuator and grip controls when a waveform is running, or when in load/strain control.

Console Software

Console Software is the main user interface to the 8800 controller. Running on a PC, it allows all controller functions to be viewed and configured including control-loop optimization, setting of operational limits, and running of simple cyclic tests. Console provides the foundation for running more demanding tests in application software such as WaveMatrix®, Bluehill®, or specific software, such as the Low Cycle Fatigue or Fracture Mechanics suite.



Specifications

Configuration

Axes of control	-	1-2
Sensor conditioning channels	-	Up to 8
Channels as Standard	-	Position and Load
Spare Channel Slot for	-	Strain 1 and Strain 2 or any other compatible sensors
Control Loop Type	-	Type PID (Proportional, Integral, Derivative), Lag, Feed Forward (2 Term), Notch (4 Term) and External Compensation Input (e.g. Acceleration or Pressure Feedback)
Control Loop Update Rate	-	5 kHz
Auto Loop Shaping	-	Position, Load, and Strain
Adaptive Loop Shaping	-	Continually Updated PID Terms at 1 kHz
Low Power "Specimen Loading Mode" Feature	-	Maximum Actuator Velocity Limited by Control System

External Inputs and Outputs

Analog Input	-	1 off Per Axis, +/-10V Scalable
Analog Outputs	-	4 off Per Axis, +/-10V with 20% Over-Range, Zero Suppressed and Scalable. Selectable from Feedback Signals, Demand Error, etc.
Digital Inputs	-	4 off, Programmable, Low Level Opto Isolated Optional: 4 off 24V Inputs
Digital Outputs	-	4 off, Programmable, Low Level Opto Isolated for High-Speed Switching Optional: 4 off 24V, 1A Outputs for High Power Switching

Waveform Generation

Frequency Range	-	0.00001 to 1,000 Hz
Resolution	-	32-bit
Waveforms	-	Sine, Triangle, Square, Haversine, Havertriangle, Havesquare, Ramp, Dual Ramp, Trapezoidal, and Random

Signal Conditioning

Compatible Transducer Types	-	Resistive Bridges (e.g. Strain Gauged Load Cells and Extensometers), AC Devices (e.g. LVDT) and DC (e.g. Pre-Conditioned Devices)
Transducer Recognition / Calibration	-	Automatic with Instron Devices, Manual with Others
Data Acquisition Rate	-	5 kHz
Resolution	-	19-bit (1k Hz Bandwidth) 24-bit (1 Hz Bandwidth via a Digital Readout)

System Measurement Accuracies (with Instron Transducers)

Position	-	±0.2% of Transducer Full Travel Under Normal Operating Conditions
Load	-	±0.002% of Load Cell Capacity or 0.5% of Indicated Load, Whichever is Greater - Meets or Surpasses ISO7500-1 Class 0.5, ASTM E 4, EN10002-2 Class 0.5, JIS (B7721, B7733) Down to 1/250th of Full Scale.
Strain	-	±0.005% of Transducer Capacity or ±0.25% of Reading ±Transducer Accuracy, Whichever is Greater. Meets or Surpasses ISO9513 Class 0.5, 1, 2, ASTM E 83 Class B1, B2, C, D, EN 10002-4 Class 0.5, 1, 2 and JIS7741 Grade 0.5, 1, 2 Depending on the Extensometer Used.

General Specifications

Weight (Fully Populated)	kg	14
	lb	31
Height	mm	450
	in	17.7
Width	mm	198
	in	7.8
Depth	mm	475
	in	18.7
Electrical Supply	-	80-132 and 180-264V 45-65 Hz Single Phase (Auto Switching)
Power Consumption	-	800 VA Maximum
Environmental Conditions	°C	10 to 38, Humidity 10 to 80% Non-Condensing
	°F	50 to 100, Humidity 10 to 80% Non-Condensing



3D View (All Measurements in mm)

www.instron.com



Worldwide Headquarters
825 University Ave, Norwood, MA 02062-2643, USA
Tel: +1 800 564 8378 or +1 781 575 5000

European Headquarters
Coronation Road, High Wycombe, Bucks HP12 3BY, UK
Tel: +44 1494 464646

Instron Industrial Products
900 Liberty Street, Grove City, PA 16127, USA
Tel: +1 724 458 9610

Instron is a registered trademark of Illinois Tool Works Inc. (ITW). Other names, logos, icons and marks identifying Instron products and services referenced herein are trademarks of ITW and may not be used without the prior written permission of ITW. Other product and company names listed are trademarks or trade names of their respective companies. Copyright © 2012 Illinois Tool Works Inc. All rights reserved. All of the specifications shown in this document are subject to change without notice.

8800MiniTowerControlElectronics_V2

(Adapted from: <https://www.instron.us/-/media/literature-library/products/2012/10/8800-minitower-control-electronics.pdf?la=en-US>)

AMTI VIVO Joint Simulator



Technical Data

HARDWARE REQUIREMENTS & DIMENSIONS VIVO requires an external 5.5 MPA (800 psi) hydraulic power supply. Overall VIVO system dimensions shown below do not include the computer or hydraulic power unit.

VIVO OVERALL DIMENSIONS	PER TEST STATION
Height	1900 mm
Width	635 mm
Depth	965 mm
SPECIMEN WORKING AREA	WITH ABDUCTION / ADDUCTION GIMBAL
Vertical	
Below gimbal centerline	Adjustable, 130 mm - 310 mm
Above gimbal centerline	Unlimited
Width	
Right of gimbal centerline	120 mm
Left of gimbal centerline	Unlimited
Depth	240 mm

ISO & ASTM TESTING STANDARDS

VIVO performs a wide range of testing standards—capable of performing tests to ISO 14242-1, ISO 14243-1, ISO/CD 14243-3, ISO 14879-1, ISO 16402, ISO18192-1, ISO/TR 22676, ISO 7206-4, ASTM F1223-08, ASTM F2790-10, ASTM F2694-07, ASTM F2777-10, ASTM F2028-08, ASTM F1829-98

SPECIFICATIONS

TEST STATIONS	SPECIFICATION	
Modular, 1 to 3 test stations	All stations' motions are independent.	
DEGREE OF FREEDOM/AXIS	FORCE/TORQUE	DISPLACEMENT/ROTATION
Axial Load	±4500 N	±25 mm
Flexion	±80 N-m	±100°
IE Rotation	±40 N-m	±40°
Y-Axis (AP) Translation	±1000 N	±25 mm
X-Axis (ML) Translation	±1000 N	±25 mm
Abduction/Adduction or Valgus/Varus	±60 N-m	±30°

CONTROL AND DATA ACQUISITION ELECTRONICS

VIVO includes a complete data acquisition system, supervisory PC and internal real-time controller.

CONTINUED

SPECIFICATIONS CONTINUED

ACTUATOR TYPE	SPECIFICATION	
All Degrees of Freedom	Servo-hydraulic	
D.O.F. / AXIS	SENSORS	AVAILABLE CONTROL MODES
Vertical Actuator	Fz force & position	Force or displacement control
Flexion	Mx torque & position	Torque or displacement control
IE Rotation	Mz torque & position	Torque or displacement control
Y (AP) Translation	Fy force & position	Force or displacement control
X (ML) Translation	Fx force & position	Force or displacement control
Abduction/Varus	My torque & position	Torque or displacement control
LOAD CELLS	SPECIFICATION	MEASURED FORCES & MOMENTS
Six-Axis	Removable	Fx, Fy, Fz, Mx, My, Mz
PHYSICAL SPECIFICATIONS	SPECIFICATION	
Height	1900 mm	
Width	635 mm	
Depth	965 mm	
Weight	272 kg (800 lbs)	
HYDRAULIC SYSTEM [1]	SPECIFICATION	COMMENT
External hydraulic power supply		Required, quoted separately
Pressure	5.5 MPa (800 psi)	Required
Required Flow	30 LPM (8 GPM) Typical Gravity drain return	Required
Oil Temperature	38°C	Recommended at outlet
Water Cooling	3kW Typical 2 LPM @ 15°C	26°C Max cooling water temperature
POWER [2]	SPECIFICATION	COMMENT
Electric	115/230 VAC, 1500 watts	1 phase, 50/60 Hz
CE Compliant		

DYNAMIC PERFORMANCE

ITEM	MAXIMUM REPETITION RATE (REPETITIONS/SECOND)		
Controller	30 Hz		
D.O.F	TYPICAL REPETITION RATE (REPETITIONS/SECOND) [3]	MAXIMUM SPECTRAL CONTENT (HZ) [4]	RMS ERROR (% FS) [5]
Axial Load	2.0 Hz	10 Hz	< 1 %
Flexion Extension	2.0 Hz	10 Hz	< 1 %
IE Rotation	2.0 Hz	10 Hz	< 1 %
Y (AP) Translation	2.0 Hz	10 Hz	< 1 %
X (ML) Translation	2.0 Hz	10 Hz	< 1 %
Abduction/Varus	2.0 Hz	10 Hz	< 1 %



ENVIRONMENTAL CONDITIONING FOR SPECIMENS

SPECIMEN FLUID RECIRCULATION	SPECIFICATION	COMMENT
Pump	100 ml/min	60 RPM peristaltic with #25 silicone tubing
Reservoir	500 ml	Stainless steel tank
Fluid Level	High/Low	Magnetic sensor/float
SPECIMEN FLUID TEMPERATURE	SPECIFICATION	COMMENT
Temperature Controller	50 watts heating/cooling	Thermoelectric
SPECIMEN FLUID	SPECIFICATION	
Suitable fluids	Bovine serum, saline solution, water	

MEASUREMENT INSTRUMENTATION

DATA ACQUISITION	CHANNEL	RANGE	COMMENT
Data Rate	All channels	10-2000 samples/sec	User selectable
ADC Resolution	All channels	14 bit	
Digital Filters	All channels	10-500Hz	User selectable
Anti-Aliasing Filters	All channels	600 Hz	
MULTI-AXIS LOAD CELL	CHANNEL	RANGE	
Axial Load	Fz	±4500 N	
AP Force	Fy	±2200 N	
ML Force	Fx	±2200 N	
Flexion Moment	Mx	±200 N-m	
Valgus Moment	My	±200 N-m	
Axial Moment	Mz	±100 N-m	
ANGLE AND POSITION	RANGE	NOMINAL RESOLUTION	
Axial Position	±25 mm	0.1 mm	
Flexion	±100°	0.1°	
IE Rotation	±40°	0.1°	
Y (AP) Translation	±25 mm	0.1 mm	
X (ML) Translation	±25 mm	0.1 mm	
Abduction/Varus	±30°	0.1°	
OTHER SENSORS	COMMENT		
Serum Temperature	Dual sensors		
Oil Temperature	Table top temperature		
Serum Fluid Level	High/low safety shutoff		
Hydraulic Pressure	Dual gauges and supply sensor		

SPECIFICATIONS CONTINUED

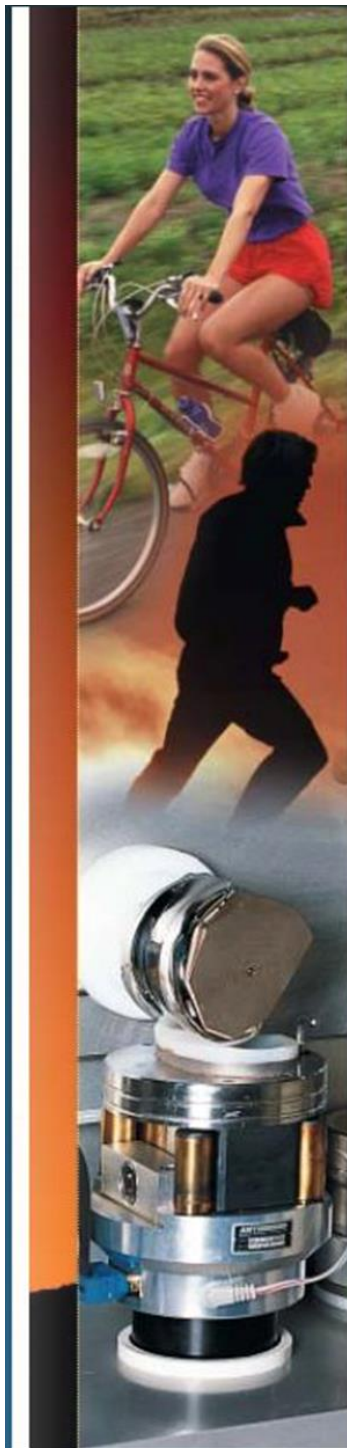
CONTROL SYSTEM

NETCONTROL INTERFACE	SPECIFICATION	COMMENTS	
Included Computer Hardware		Windows based PC and accessories	
Interface	Ethernet 1Gb		
REAL-TIME CONTROLLER	SPECIFICATIONS	COMMENTS	
Intel Core 2 Controller	2.8 GHz	Double precision floating point math	
Update Rate	2000 Hz		
CONTROL MODES	CHANNELS		
State Space Control	6		
Gain Scheduling	6		
Adaptive Control	6		
Virtual Soft Tissue	6		
WAVEFORM GENERATOR	CHANNELS	RANGE	COMMENTS
Reference Waveforms	6		
Repetition Rate	All channels	0.01 to 30 Hz	
Programmable		1024 points	Interpolated
EVENT MONITOR	CHANNELS	SPECIFICATION	COMMENTS
Threshold Trigger	5 per station		Rising or falling edge
Response Time	All channels	0.0005 seconds	
Programmable Response	All channels		Soft stop, hold, shut down
DATA ACQUISITION	CHANNELS		
Force/Torque	6		
Displacement/Rotation	6		
Temperature	4		
Reference Waveforms	6		
Servo Error	6		
Soft Tissue Constraint	6		
Sum Signals	6		
Oil Pressure	1		

[1] The external hydraulic system requires cooling water for operation, usually available from your laboratory's infrastructure. If not available, contact AMTI for information about chillers. [2] Contact AMTI for other power configurations. [3] The typical repetition rate corresponds to the maximum rate at which satisfactory performance will be achieved running the ISO standard gait cycle waveforms for knee testing. This is a somewhat subjective indication of dynamic performance. Overall tracking performance is reduced with higher frequency of operation. [4] The ISO waveforms contain spectral content in considerable excess of the fundamental driving frequency. Analysis of these waveforms indicates that tracking performance at a 1 Hz repetition rate is excellent up to the indicated frequency. [5] The RMS error provides a measure of the simulator's tracking performance (the extent that the machine's outputs differ from the target inputs). These values are typical for testing at a 1 Hz repetition rate while running the ISO waveforms and represent standard results while evaluating conventional prosthetics using AMTI's Adaptive Control Technology (iterative learning control algorithm). Different prosthetic devices or conditions may result in an increased or decreased tracking error.

(Adapted from: <https://www.amti.jp/AMTI-VIVO-Brochure-Rev2-HiRes.pdf>)

AMTI Boston



AMTI-Boston 6-Station Knee Simulator Model KS2-6-1000

The AMTI-Boston Knee Simulator, developed with the guidance of the medical profession and manufacturers of implants, simulates the loading and multi-axis motion of the knee in a physiologic environment. At each station the implant components are mounted in the proper fashion and the contact area is immersed in a sealed, temperature controlled fluid bath. The microprocessor controlled system allows programming of an endless combination of loads and motions in order to simulate walking, stair climbing etc. The simulator provides a system for evaluating materials, implant component designs and implant life testing.

The knee simulator has six stations arranged in two banks of three. Each bank may be operated at a different set of conditions. The system has four controlled degrees of freedom (load and three motions) on each bank. The femoral component rotates about the horizontal axis to a maximum of 134° in flexion ($\pm 67^\circ$ of flexion-extension); the femoral component translates (anterior/posterior translation) a maximum of ± 25 mm (± 1 in.) relative to the tibial tray. The tibial component has a maximum possible rotation about the vertical axis of $\pm 20^\circ$. Two other motions are allowed but not controlled; the tibial component is allowed to translate along the horizontal plane and rotate about the horizontal axis to provide "nesting" of the femoral and tibial components (a maximum of ± 10 mm (0.5 in.) of translation, and $\pm 3^\circ$ of rotation). A programmable axial load up to 4500 N (1000 lb) is applied at each station, where typical walking patterns may contain four load peaks during each step. Prior to the initiation of a test, adjustments may be made to provide for different condyle loading; for example, the distribution of the load applied may be set at 50% on each condyle, or up to 80% loading on either condyle.

Available as an option is medial/lateral force control on the tibial component. This feature results in a five degree-of-freedom simulator with ± 7.5 mm. of allowable translation and $\pm 5^\circ$ of tibial tray rotation.

The operating speed of the machine is variable up to speeds of 2 Hz - the speed is programmed through the computer. Each joint is immersed in its own bath of bovine serum, saline or water temperature-controlled fluid. Separate reservoirs (including level sensors) are provided for each station and each station includes its own pump to circulate the fluid to the test station. The knee components are enclosed in a flexible plastic bag (I.V. bag) to limit fluid evaporation and prevent foreign materials from influencing the test results.

At each station is a force/torque (Fx, Fy, Fz, Mx, My, Mz) load cell allowing any or all of the load components to be monitored continuously or at periodic intervals. In addition, motions and temperatures are available for monitoring at each station. These parameters are available for evaluation of the implant, wear, changing friction etc. as the testing proceeds. The simulator runs unattended 24 hours per day, allowing completion of 172,000 cycles per day when testing at 2 Hz. Each fluid reservoir contains level sensors, which shut off the machine if a leak in the system occurs or certain other malfunctions occur. Polycarbonate doors provide environmental and safety protection.





Specifications

6-Station Knee Simulator Model No. KS2-6-1000

- ◆ Six Station Knee Simulator arranged in 2 banks of 3.
- ◆ 4 Separate actuator axes for each bank; total of 8 servohydraulic control valves.
- ◆ Fz loads up to 4500 N (1000 lb) at each station; each bank of three under separate control.
- ◆ Mz loads up to 45 N·m (400 in-lb) at each station; each bank of three under separate control ($\pm 20^\circ$ rotation).
- ◆ Flexion of 134° total rotation with 56 N·m (500 in-lb) of torque per station; each bank of three under separate control.
- ◆ ± 25 mm of anterior/posterior motion at up to 1800 N (400 lb) per station; each bank of three under separate control.
- ◆ All motions servohydraulically generated with laminar seal actuators for long life ($> 10^6$ cycles).
- ◆ Separate six component load cells at each station (Fx, Fy, Fz, Mx, My, Mz).
- ◆ Separate peristaltic pump and reservoir unit with temperature and level sensors at each station. Automatic shut-down due to test fluid containment system leakage.
- ◆ Temperature control of test fluid at 37°C ($\pm 1\text{K}$) or other set point, provided by a closed loop recirculating heater/chiller unit.
- ◆ A total of 8 separate software programmable drive signals for the axes of motion.
- ◆ The four actuators on each bank can be "manually" controlled in addition to their full automatic operation.
- ◆ Separate cycle counter for each bank in addition to computer monitor of cycles for machine shut down.
- ◆ Up to 2 Hz speed - adjustable by computer.
- ◆ Separate unbreakable polycarbonate doors over each bank.
- ◆ Rated for continuous 24 hour operation.
- ◆ High pressure hydraulic filter: 6 micron ($6\ \mu\text{m}$) with indicator light.
- ◆ Separate hydraulic power supply required but not included - 5 MPa @ 1 L/s. (800 psi @ 15 gpm), gravity drain return line with no restrictions.
- ◆ Included is software (SIMMAC™) to operate the simulator, prepare "load" and "motion" templates for simulation of different conditions (walking, stair climbing etc.) and safety /low fluid shutdown of system. Also, included is a software program which is used in calibration of the simulator load cells.

Knee Simulator Options

Knee Simulator Vertical Position Sensor (model VPS-6)

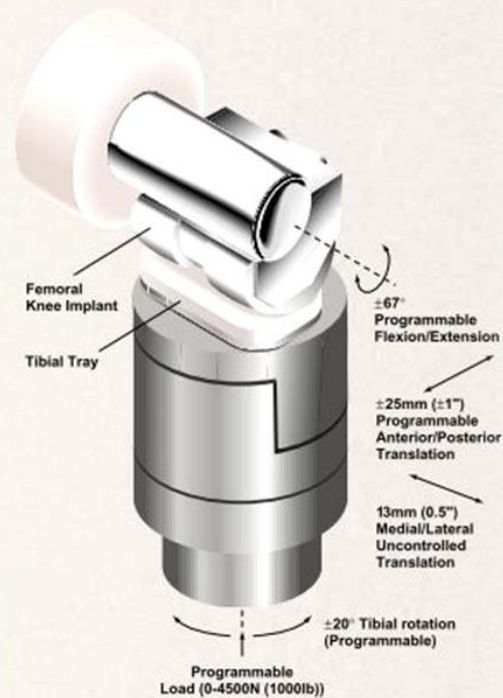
This option provides the six stations with a measurement of the vertical position of the tibial tray specimen holder. The sensors are of a non-contacting magnetic design and provide an output of 10 V/in. (0.4 V/mm). The measurement resolution is less than .001 inches (25 μm). All electrical outputs are wired in and sampled as part of the data acquisition routine for the stations.

Knee Simulator Tibial Torque Actuators (model KTTA)

This option provides an independent servo controlled medial/lateral force on each tibial component, with ± 7.5 mm of allowable medial/lateral translation and $\pm 5^\circ$ of allowable rocking about the A/P axis. Sensors are provided for the translation and rocking motions. The controlled output is ± 900 N (200 lb) for ± 10 V of command. There are individual pneumatic servo valves with a closed loop controller on the top of each load cell. All six actuators are controlled by a common command signal. With this option, the left and right banks of the machine are not provided with separate command signals. A continuous source of oilless air is required and recommendations for a suitable compressor will be provided.

Knee Machine Load Cell Calibration Fixtures (model KLCC)

Hardware and software to calibrate the six-component load cell is provided in this package. A single axis calibration cell is used to calibrate all channels at levels simulating operating loads.



(Adapted from: <https://www.yumpu.com/en/document/read/42207110/amti-boston>)

Curriculum Vitae

Name: Geoffrey Yamomo

Post-secondary Education and Degrees: The University of Western Ontario
London, Ontario, Canada
2012-2017 BESC

Related Work Experience

Teaching Assistant– FEM in Mechanical Engineering
The University of Western Ontario
Jan 2019-Apr 2019

Teaching Assistant– Advanced CAE: Reverse Engineering
The University of Western Ontario
Jan 2018-Apr 2018, Sept 2018-Dec 2018

Teaching Assistant– Advanced CAE: Simulation
The University of Western Ontario
Sept 2017-Dec 2017

Publications:

Willing R, Moslemian A, Yamomo G, Wood T, Howard J, Lanting B. Condylar-Stabilized TKR May Not Fully Compensate for PCL-Deficiency: An In Vitro Cadaver Study. *Journal of Orthopaedic Research*, 37:2172–2181, 2019.

Ibrahim A, Yamomo G, Willing R, Towfighian S. Analysis of a triboelectric energy harvester for total knee replacements under gait loading. *Proc. SPIE 10967, Active and Passive Smart Structures and Integrated Systems XIII*, 109671D (21 March 2019).

Conference Presentations and Posters:

Yamomo G, Ibrahim A, Towfighian S, Willing R. (2019) Tuning of 3D Printed Energy Harvester Package Design. *International Society for Technology in Arthroplasty 32nd Annual Congress, October 2-5, Toronto, Ontario*

Yamomo G, Moslemian A, Wood T, Lanting B, Willing R. (2019) Kinematic and Laxity Comparison between Cruciate Retaining and Cruciate Sacrificing Total Knee Replacements. *International Combined Orthopaedic Research Societies 2nd Annual Meeting, June 19-22, Montreal, Quebec*

Yamomo G, Moslemian A, Wood T, Lanting B, Willing R. (2019) Kinematic Comparison between Cruciate Retaining and Cruciate Sacrificing Total Knee

Replacements during Gait and Stair Ascent. *International Combined Orthopaedic Research Societies 2nd Annual Meeting, June 19-22, Montreal, Quebec*

Yamomo G, Moslemian A, Wood T, Lanting B, Willing R. (2019) Post-Operative Laxity Outcomes of Cruciate Retaining and Condylar Stabilizing Total Knee Replacements. *London Health Research Day, April 30, London, Ontario*

Yamomo G, Moslemian A, Wood T, Lanting B, Willing R. (2019) Post-Operative Laxity Differences Between Cruciate Retaining and Condylar Stabilizing Total Knee Replacements. Ontario Biomechanics Conference, March 8-10, Alliston, Ontario